



Faculteit Wetenschappen
Departement Fysica

Het Ontwikkelen van 3D Statistische Vormmodellen voor Diverse Applicaties

The Development of 3D Statistical Shape Models for Diverse Applications

Proefschrift voorgelegd tot het behalen van de graad van

Doctor in de Wetenschappen

aan de Universiteit Antwerpen, te verdedigen door

Femke DANCKAERS

Promotoren:

Prof. Dr. Jan Sibbers

Prof. Dr. Toon Huysmans

Antwerpen, 2018

Doctoral jury:

Prof. Dr. Jan Sijbers

Prof. Dr. Toon Huysmans

Prof. Dr. Joris Dirckx

Prof. Dr. Stefan Van Dongen

Prof. Dr. Ir. Richard Goossens?

Prof. Dr. Steven Truijen?

Prof. Dr. Matthew Reed?

Contact information:

✉ **Femke Danckaers**

imec - Vision Lab, Dept. of Physics

University of Antwerp (CDE)

Universiteitsplein 1, Building N1.18

B-2610 Wilrijk, Antwerpen, Belgium

☎ +32 3 265 24 77

✉ femke.danckaers@uantwerpen.be

🌐 <http://visielab.uantwerpen.be/people/femke-danckaers>

All rights reserved. No part of the material protected by this copyright notice may be reproduced or utilized in any form or by any means, electronic or mechanical, including photocopying, recording, broadcasting or by any other information storage and retrieval system without written permission from the copyright owner.

“We come in many different shapes and sizes,
and we need to support each other and our differences.
Our beauty is in our differences.”

CARRE OTIS



Contents

Summary

The human body appears in many shapes and sizes. For product developers, it is useful to have a virtual 3D mannequin available to generate and validate their designs. Such anthropometric tools are widely available, but often provide only a simplified representation of the body, based on 1D measurements. Modification of the shape is often done in an univariate way, so 3D shape variation is not incorporated in such models.

In this work, we concentrate on the 3D shape of objects. A 3D shape can be represented by a triangular mesh, which consists of vertices, connected by edges. Those edges form triangles. If a population of 3D shapes is present, a statistical shape model (SSM) can be built. This model consists of the average 3D shape of the object class and the main shape variations that occur inside the shape population. This thesis presents methods for an improved shape analysis of 3D body shapes. The methodology is not restricted to body shapes and is applicable to almost every object class that contains natural variance.

Chapter 1 is the introduction of this manuscript. First, digital human modeling and statistical shape modeling are shortly introduced, followed by possible applications of an SSM. Finally, an overview of the chapters is given.

For building an SSM, the shapes within a population need to be in correspondence with each other, so a point with a specific ID is on the same anatomical location for every shape. In Chapter 2, the method for elastic surface registration to obtain correspondence and building an SSM from corresponded surfaces is described. Additionally, this chapter describes how to use an SSM to register a new surface. Furthermore, registering a shape by an SSM is useful to reconstruct missing parts and to reduce artifacts due to the used scanning method.

Chapter 3 describes body shape modeling based on intuitive parameters, such as height, weight, gender, waist circumference,... This may be useful for product designers who want to quickly simulate a virtual mannequin of a costumer. Furthermore, in this chapter is examined which features are the most suitable to accurately predict a body shape.

In Chapter 4, a posture normalization technique is described. Shape variation captured by an SSM is often polluted by variations in posture, which may incorrectly correlate with features and negatively affects the compactness of those models. A framework that has low computational complexity to build a posture-invariant SSM, by capturing and correcting the posture of an instance, is shown. With the help of posture normalization, body shape can be analyzed in a more univariate way, as noise from posture variation is eliminated.

Statistical shape models are typically a static representation of a population. In Chapter ??, a movement acquired by a motion capturing system is integrated in the SSM. This is done by selecting landmarks on an SSM and predicting a body shape based on features. Then, a virtual skeleton is generated relative to those landmarks

and parented to the body shape, allowing to modify its pose in a realistic way and to add pre-recorded motion to different body shapes in a realistic way.

In Part III of the manuscript, some of many applications of SSMs are worked out in detail. In Chapter ??, an SSM of horticultural products is described. The method is applied to Jonagold apples, bell peppers and zucchini, reconstructed from X-ray CT scans. The algorithm is capable of generating a broad dataset of realistic instances for simulation purposes, such as stacking algorithms.

Chapter ?? gives more insight in the shape of the skull and the scalp. An SSM is a valuable tool when designing headgear, as it captures the variability of head geometry, enabling detailed analysis of the relation between the shape of the scalp and the skull. A combined SSM of the head may allow to work towards population based finite element models, e.g. for safety and comfort predictions when wearing headgear.

In Chapter ??, the human middle ear is looked into. The large morphological variations could affect our perception of hearing and explain large variations in experimentally obtained transfer functions. The statistical shape analysis is based on clinical cone beam CT scans of 100 patients. From the shape analysis could be deduced that the middle ear transfer function is not only influenced by anatomical features and inertia properties, but that the mechanical properties of the ligaments also have a major effect on this transfer function.

In Part IV, a conclusion of the manuscript is formed, followed by a bibliography. Then, there is a summary of software developed during the research presented in this thesis. Finally the curriculum vitae of the author is given, as well as a list of publications that preceded this manuscript.

Samenvatting

Het menselijk lichaam komt voor in verschillende vormen en maten. Voor productontwikkelaars is het belangrijk om een virtuele 3D paspop beschikbaar te hebben voor het ontwikkelen en valideren van hun ontwerpen. Zulke antropometrische hulpmiddelen zijn reeds beschikbaar, maar zijn veelal een vereenvoudigde voorstelling van het lichaam, gebaseerd op 1D metingen. Het aanpassen van de lichaamsvorm gebeurt vaak op een univariante manier, dus 3D vormvariatie is niet aanwezig in dit soort modellen.

In dit werk concentreren we ons op de 3D vorm van objecten. Een 3D vorm kan weergegeven worden met een driehoeksmaas, die bestaat uit hoekpunten die verbonden zijn met randen, om driehoeken te vormen. Wanneer een populatie 3D vormen beschikbaar is, kan een statistisch vormmodel (SSM) opgesteld worden. Dit model bevat de gemiddelde 3D vorm van de object klasse en de belangrijkste vormvarianties die voorkomen in de populatie. Deze thesis presenteert methodes voor een verbeterde vormanalyse van 3D lichaamsvormen. De methodologie is niet gelimiteerd tot lichaamsvormen en kan toegepast worden op bijna elke object klasse die natuurlijke variatie bevat.

Hoofdstuk 1 is de introductie van dit manuscript. Eerst worden het digitaal modelleren van de mens en statistische vormmodellering kort geïntroduceerd, gevolgd door mogelijke toepassingen van een SSM. Ten slotte is er een overzicht van de hoofdstukken.

Voor het opstellen van een SSM moeten de vormen die voorkomen in de populatie met elkaar in correspondentie zijn, zodat voor elke vorm een punt met een bepaald ID op dezelfde anatomische locatie ligt. In Hoofdstuk 2 wordt de methode voor elastische oppervlakregistratie om correspondenties te bekomen en het opstellen van een SSM uit deze gecorrespondeerde oppervlakken uitgelegd. Aanvullend beschrijft dit hoofdstuk hoe een SSM aan een nieuw oppervlak geregistreerd kan worden. Het registreren van een vorm met een SSM is nuttig voor het reconstrueren van ontbrekende delen en het verminderen van artefacten te wijten aan de gebruikte scanmethode.

Hoofdstuk 3 gaat over het modelleren van het lichaam op basis van intuïtieve parameters zoals lengte, gewicht, geslacht, taille omtrek,... Dit is bruikbaar voor productontwikkelaars die snel een virtuele paspop van een klant willen simuleren. Verder wordt in dit hoofdstuk onderzocht welke parameters het meest geschikt zijn voor het accuraat voorspellen van een lichaamsvorm.

In Hoofdstuk 4 wordt een methode om houding te normaliseren behandeld. Vormvarianties die beschreven worden door een SSM zijn vaak verstoord door variaties in houding, welke incorrect gecorreleerd kunnen worden met specifieke vormparameters en een negatief effect hebben op de compactheid van deze modellen. In dit hoofdstuk wordt een raamwerk met lage computationele complexiteit voorgesteld om een houding-invariant SSM op te stellen. Dit gebeurt door het afsplitsen en corrigeren van de houding van een persoon. Hierdoor kan lichaamsvorm univariaat geanalyseerd

worden, omdat de ruis door het verschil in houding wordt geëlimineerd.

Statistische vormmodellen zijn typisch een statische representatie van een populatie. In Hoofdstuk ?? wordt beweging, opgemeten is door een motion capture systeem, geïntegreerd in het SSM. Dit gebeurt door eerst herkenningpunten op het SSM te selecteren en dan een lichaamsvorm te voorspellen op basis van lichaamskenmerken. Vervolgens wordt een virtueel skelet relatief tot de herkenningpunten gegenereerd en gelinkt aan de lichaamsvorm. Hierdoor kan de houding aangepast worden op een realistische manier en kan ook vooraf opgenomen beweging toegepast worden op verschillende lichaamsvormen.

In Deel III van het manuscript worden sommige toepassingen van SSMs in detail uitgewerkt. Hoofdstuk ?? is de beschrijving van SSMs van horticulturele producten. De methode werd toegepast op Jonagold appels, paprika's en courgettes, welke gereconstrueerd werden uit X-stralen CT scans. Het algoritme is in staat om een grote dataset van realistische instanties te genereren voor simulatie doeleinden, zoals stapelalgoritmes.

Hoofdstuk ?? geeft meer inzicht in de vorm van de schedel en hoofdhuid. Een SSM is een waardevolle tool voor het ontwerpen van hoofddeksels omdat het de variabiliteit van de hoofdgeometrie weergeeft, waardoor de relatie tussen de vorm van de schedel en hoofdhuid gedetailleerd geanalyseerd kan worden. Dankzij een gecombineerd SSM van het hoofd kunnen we werken naar een finite element model gebaseerd op de gehele populatie, voor bijvoorbeeld veiligheid- en comfort predicties bij het dragen van helmen.

In Hoofdstuk ?? wordt het middenoor geanalyseerd. De grote morfologische variaties kunnen onze perceptie van horen beïnvloeden en verklaren de grote variaties in experimenteel verkregen transfer functies. De statistische vormanalyse is gebaseerd op klinische cone beam CT scans van 100 patiënten. Uit de vormanalyse kan afgeleid worden dat de transfer functie van het middenoor niet enkel door anatomische kenmerken en inertie eigenschappen wordt beïnvloed, maar dat de mechanische eigenschappen van de ligamenten ook een groot effect op deze transfer functie hebben.

In Deel IV wordt een conclusie van het manuscript gevormd, gevolgd door een bibliografie. Vervolgens is er een samenvatting van de software die werd ontwikkeld tijdens dit onderzoek. Ten slotte wordt een curriculum vitae van de auteur gegeven, alsook een lijst van publicaties die dit manuscript vooraf zijn gegaan.

List of Abbreviations

CAD	Computer Aided Design
CT	Computed Tomography
DHM	Digital Human Model
FE	Finite Element
ICP	Iterative Closest Points
LBS	Linear Blend Skinning
MRI	Magnetic Resonance Imaging
N-ICP-A	Nonrigid ICP Affine
N-ICP-T	Nonrigid ICP with Translation vectors
PCA	Principal Components Analysis
RN-ICP-T	Rigid initialization + N-ICP-T
RNM-ICP-T	RN-ICP-T with shape model prior
SSM	Statistical Shape Model
UCD	User Centered Design

Part I

Introduction

1

Introduction

Contents

1.1	User Centered Design	4
1.1.1	Digital Human Models	4
1.2	Statistical Shape Model	5
1.2.1	SSM-based DHMs versus Traditional DHMs	5
1.2.2	3D Scanning	5
1.2.3	3D Representation of Objects	7
1.3	Applications	7
1.4	Manuscript Organization	8

1.1 User Centered Design

Designing and developing a good solution for a problem is often a laborious process. User Centered Design (UCD) is a method to split this process in several subtasks and leads to a more user-friendly result. The process of UCD is structured in four phases: analysis, design, evaluation and implementation. UCD cannot be regarded as a linear process, as every step of the cycle will usually be repeated multiple times to become an optimal result, as visualized in Figure 1.1.

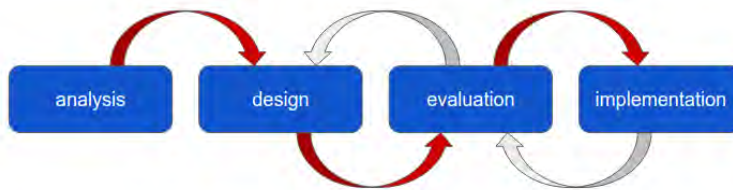


Figure 1.1: Schematic overview of User Centered Design. Every step of the cycle will usually be repeated multiple times to become an optimal result.

For developers of near-body products, anthropometry is an important factor to take into account. Anthropometry is the science of measuring the dimensions of groups of people, to numerically represent the body dimensions and variations. On the one hand there is the classic anthropometry, that is most often uni-, bi-, or multivariate. This type of anthropometry is based on a small set of 1D measurements and leads to compact datasets, often represented by tables, that can be used by a product developer. Surface-based anthropometry, on the other hand, takes the whole 3D shape into account. Therefore, it contains more measurements and thus more shape information that can be used by designers compared to traditional anthropometry.

1.1.1 Digital Human Models

When designing wearables, it is important that the users like the product. To be comfortable, the product should fit the body dimensions of the user. Therefore, realistic virtual mannequins that represent body shapes that occur in a specific target population, are valuable tools for product developers. Such tools (Digital Human Models - DHM) use computer aided design technology to create and manipulate a 3D human model in a virtual environment. DHMs are already widespread, but are often an oversimplified representation of the population, based on 1D measurements, so 3D shape variation is not incorporated [Moes, 2010; Blanchonette, 2010; Van Der Meulen and Seidl, 2007]. Some examples of body shapes generated by the DHM tool Jack are shown in Figure 1.2. The body shape is modified by scaling the body parts in a univariate way. This is not sufficient for designing products that have to fit tightly to the body [Bragança et al., 2016]. There, it is preferable that the DHM is fully customizable in body shape and pose, so it is employable for designing for a broad range of persons and actions.



Figure 1.2: Examples of body shapes generated by Jack [Godin, 2011].

1.2 Statistical Shape Model

An alternative way to capture the variability of shapes in a population is to represent these shapes by statistical shape models (SSMs) [Park and Reed, 2015]. An SSM represents the average shape of the object class and the main variations that occur in the population. Thanks to SSMs, the UCD cycle can be shortened, as it is possible to virtually evaluate the design for a broad range of realistic body shapes that can occur in the population. In Chapter 2, a more detailed explanation of the methods used in this thesis for constructing SSMs are described.

1.2.1 SSM-based DHMs versus Traditional DHMs

The advantage of SSM-based DHMs over traditional DHMs is that they are built from real data. Therefore it contains information about the whole population that can be analyzed. Because of the real data, a simulated shape will always lie in the shape space of the model. As a result, it will generate realistic shapes, in contrast to shapes generated by traditional DHMs. The difference between the two is visualized in Figure 1.3. From this figure can be seen that an SSM-based DHM has a realistic body shape, while a traditional DHM [3D human model, 2017] is a simplified representation built from a collection of body parts.

1.2.2 3D Scanning

A 3D scanner is a device that analyses a real-world object or environment to collect data of its shape and possibly its appearance (e.g. color). The collected data can then be used to construct digital 3D meshes, which in turn can be used to generate an SSM.

There are many different technologies that can be used to capture the 3D shape of an object. Each technology comes with its own limitations, advantages and costs.

Contact scanner this technology relies on the sampling of several points on a surface by physical touch, measured by the articulation of a probe.

Time-of-flight scanner this 3D laser scanner is an active scanner that uses laser light to probe the subject. The laser range finder determines the distance of a

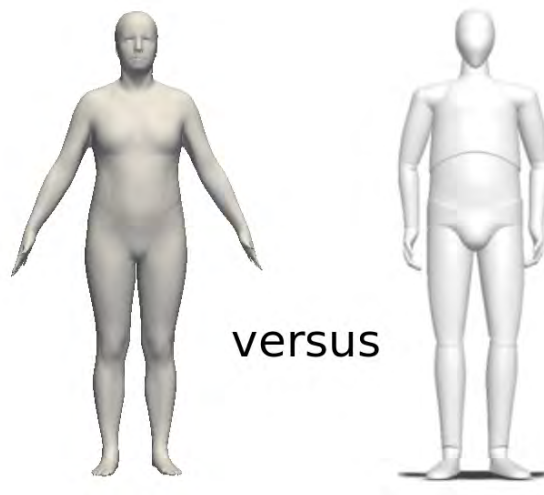


Figure 1.3: Comparison of the shape of an SSM-based DHM (left) and a traditional DHM [3D human model, 2017] (right).

surface by timing the round-trip time of a pulse of light. This type of scanner detects the distance of a point in its direction of view.

Triangulation this type of scanner also relies on laser light to probe the environment. With respect to time-of-flight 3D laser scanning, the triangulation laser shines a laser on the subject and exploits a camera to look for the location of the laser dot. Depending on how far away the laser strikes a surface, the laser dot appears at different places in the camera's field of view. The dot, camera and laser emitter form a triangle. The length between the camera and laser emitter is known and the angle of the laser emitter corner is known. The angle of the camera corner can be determined by looking at the location of the laser dot in the camera's field of view. Therefore, the shape and size of the triangle can fully be determined, hence the location of the laser dot can be calculated.

Hand-held laser scanner this type of scanners create a 3D image through the triangulation mechanism described above: a laser dot (or line) is projected on an object from a hand-held device and a sensor measures the distance to the surface. Data is collected in relation to an internal coordinate system and therefore to collect data where the scanner is in motion the position of the scanner must be determined. The position can be determined by the scanner using reference features on the surface being scanned or by using an external tracking method.

Structured light structured light 3D scanners project a pattern of light on the subject and look at the deformation of the pattern on the subject. A camera looks at the shape of the pattern and calculates the distance of every point in the field of view. The advantage of structured light 3D scanners is speed and precision. Instead of scanning one point at a time, structured light scanners scan multiple points of the entire field of view at once. Therefore, they are less sensitive to distortion from motion.

Volumetric techniques techniques such as CT and MRI generate a 3D image of

the inside of an object from a large series of 2D images. These techniques produce a discrete 3D volumetric representation that can be directly visualized, manipulated or converted to traditional 3D surfaces.

In this thesis, multiple scanning techniques were used to generate 3D surfaces from objects. For every experiment is specified which technique was used.

1.2.3 3D Representation of Objects

There are multiple ways to represent a 3D object. Below, the most common manners are summed up:

Point cloud The surface is represented by a group of points, with each point its own 3D coordinates

Triangular mesh The surfaces is represented by vertices, connected by triangles

Quadrilateral mesh The surface is represented by vertices, connected by quadrilateral elements.

Basis functions The surface is represented by basis functions such as B-splines, radial basis functions,...

Level-sets The surface is represented by gray value functions, that code the distance to the object in every point.

In this thesis, we have exclusively worked with triangle meshes.

1.3 Applications

Statistical shape modeling has a wide range of applications. In this section, some of the popular applications are discussed.

SSMs are often used for image segmentation [Heimann and Meinzer, 2009; Fritscher et al., 2014; Saito et al., 2016]. Image segmentation is the process of partitioning a digital image into multiple meaningful sets of pixels. An SSM contains a lot of information about the shapes to be expected in a specific object class, because common shape variations are included in the model. This means that an SSM can be used as prior knowledge. The shape of the SSM is adapted to the most plausible shape of the object that has to be segmented. An SSM is a robust shape segmentation tool because only shapes that could occur in the object class can be formed. They are able to complement missing data by calculating the most plausible points based on the existing data. Therefore, they are a valuable tool to predict the 3D shape of an object from 2D pictures, such as photo's, MRI scans, CT scans,... [Blanz and Vetter, 1999; Smoger et al., 2017].

Another important application of SSMs is landmark detection [Lindner et al., 2017; Canavan et al., 2015; Baluwala et al., 2015]. For such applications, an SSM is built and trained with manually annotated landmarks. Therefore, if the SSM is registered to another shape, those landmarks end up on the same anatomical locations. This is useful for e.g. medical applications or design applications, where the design has to fit to specific anatomical locations on the body.

An SSM can be deployed as virtual design mannequin that is adaptable in shape by intuitive parameters. Product developers may exploit SSMs to design virtual

design mannequins and explore the body shapes belonging to a percentile of a target group, for example to visualize extreme shapes. Moreover, an SSM allows to simulate a specific 3D body shape [Park et al., 2015], which is useful for customization in a (possibly automated) workflow. This application is discussed in Chapter 3

SSMs are also often deployed to analyze the difference between groups of the same object class [Woods et al., 2017; Crum et al., 2016]. By applying statistical tests, such as ANOVA on the data, the researcher can investigate whether the groups differ and how they differ, by highlighting the areas where shapes significantly diverge.

In the case of using an SSM to detect abnormalities in shapes [Alomari et al., 2014; Stanković et al., 2016], an unknown input surface is compared with an SSM that contains the shape variations that may occur in a "normal" population. If a point on the surface is in the extreme ranges, it is regarded as an outlier and thus abnormal. By applying the test for every point on the input surface, the region where the shape is abnormal, can be marked.

Moreover, an SSM is employable as a tool for shape recognition [Lopes et al., 2014; Ferrari et al., 2010; Blanz and Vetter, 2003], to find a specific part or object in a larger scan.

1.4 Manuscript Organization

The remainder of this manuscript is organized as follows:

Part II details the methods for constructing statistical shape models

Chapter 2 details the surface registration algorithm and the method for building an SSM. To build an accurate SSM, it is important that the input surfaces are in anatomical correspondence with each other, ensuring that each instance has the same number of vertices ordered in the same fashion. A statistical shape model is built by applying principal component analysis (PCA) on the matrix containing the corresponding points of the input surfaces.

Chapter 3 explains how to predict a 3D body shape based on features. For design purposes, it is useful to be able to quickly simulate a virtual mannequin of a costumer. Therefore, a mapping between the shape model parameters and specific features can be calculated, which allows adjusting the body shape, in an intuitive way. In this chapter, we have investigated how accurate a body shape can be predicted based on a set of features and which features are most suitable for this purpose.

Chapter 4 describes the posture normalization algorithm. Shape variances captured by an SSM are often polluted by motion variances present in the database, not related to body shape. The goal of this algorithm is to correct for these motion differences, so a posture-invariant SSM can be built.

Chapter ?? demonstrates an approach to integrate movement acquired by a motion capture system with a body shape. This was done by selecting landmarks on an SSM, and predicting a body shape based on features. Then, a virtual skeleton was generated relative to those landmarks. This skeleton was parented to a body shape, allowing to modify its pose and to add pre-recorded motion to different body shapes in a realistic way.

Part III presents the applications, using the developed techniques in Part II.

Chapter ?? in this chapter, an SSM of horticultural products is built. The surfaces are obtained from X-ray CT scans. The method is applied to 30 Jonagold apples, 30 bell peppers, and 52 zucchini. All shape models are shown to be an excellent representation of their specific population, as they are compact, able to generalize to an unseen sample of the population and can randomly generate shapes that resemble those in the training set. By parameterizing the surface, the SSM and every instance that can be formed by the SSM, were described by CAD primitives. Therefore, an SSM is an effective tool for simulation software, such as stacking algorithms.

Chapter ?? explains the framework to build a combined SSM of the outer surface of the scalp and the inner and outer surface of the skull of the human head. Such an SSM is a valuable tool when designing headgear, as it captures the variability of head geometry of a given population, enabling detailed analysis of the relation between the shape of the scalp and the skull. A combined SSM of the head allows to work towards population based finite element models, e.g. for safety and comfort predictions when wearing headgear.

Chapter ?? details about the construction of an SSM of the human middle ear. The shape of the middle ear could affect our perception of hearing and explain large variation in experimentally obtained transfer functions. Statistical shape analysis was applied on clinical cone beam CT scans of 100 patients.

Part IV concludes the manuscript.

Note that the main body of this manuscript, Part II and Part III, is the result of the composition of previously published articles.

Part II

Contributions

This work was previously published as:

Danckaers, F., Huysmans, T., Lacko, D., Ledda, A., Verwulgent, S., Van Dongen, S., and Sijbers, J. (2014). Correspondence preserving elastic surface registration with shape model prior. In Proceedings - International Conference on Pattern Recognition, pages 2143-2148, Stockholm, Sweden. IEEE.

2

Correspondence Preserving Elastic Surface Registration With Shape Model Prior

Contents

Abstract	14
2.1 Introduction	15
2.2 Methods	15
2.2.1 Alignment Initialization	16
2.2.2 Amberg	17
2.2.3 Registration of Two Surfaces	20
2.2.4 Building a Statistical Shape Model	21
2.2.5 Surface Registration with Shape Model Prior	23
2.3 Evaluation	24
2.3.1 Data Sets	24
2.3.2 Shape Model	24
2.3.3 Evaluation of the Geometric Fit	25
2.3.4 Evaluation of the Correspondence Quality	25
2.3.5 Evaluation of the Sensitivity of the stiffness	26
2.3.6 Evaluation of the Timing	28
2.3.7 Influence of the Number of Iterations	28
2.4 Conclusion	29

Abstract

In this chapter, we describe a framework for surface registration. The framework consists of a combination of rigid registration, elasticity modulated registration and the use of a shape model prior. The main of surface registration is to minimize the geometric surface registration error while maintaining correspondences. Experiments show improved geometric fit, correspondence, and timing compared to the current state of the art. Possible applications of the framework are construction of correspondences for shape models, reconstruction of missing parts, and artifact reduction.

2.1 Introduction

Surface registration is a frequently used technique in many applications, such as surface recognition [Guo et al., 2013; Wang et al., 2002] or surface reconstruction [Wang and He, 2013; Zheng et al., 2009]. The goal of surface registration is to deform one surface to another while finding a meaningful mapping between the vertices of the surfaces, by maintaining the correspondences. The distance between corresponding points on the target surface and the deformed source surface must be minimal.

A developer of products that have to fit closely to the human body or a part of it, needs to gain insight into the shape variability of that specific part of the body of a target population. Statistical shape modeling is a promising approach to map out this variability [Brunton et al., 2014]. The construction of such models, based on surface-to-surface correspondences is, however, a challenging task. 3D surface registration is an elegant approach to obtain such correspondences. Based on the distribution of the shape variances, ergonomic products can be developed and tested on characteristic shapes. Furthermore, shape models are useful in intelligent systems for made-to-measure products [Jones and Rioux, 1997].

Obtaining surface correspondences can be done manually [Hasler et al., 2009], but this is time-consuming and error prone. The current challenges for surface registration are flexibility, robustness and performance [Brunton et al., 2014]. Surface registration can be done by parametrization [Cootes et al., 1995; Allen et al., 2003; T. and J., 2009; Huysmans et al., 2010]. A mapping between the source and target surface is obtained through parameterization to a common mathematical domain, such as a sphere or cylinder. The disadvantage of such a technique is that the surfaces must have the same non-complex topology, because they have to be deformed to the same target space.

Another approach is spatial registration, where features are matched [Maes et al., 2010; Lowe, 2004; Wang et al., 2002]. With these techniques, each vertex is transformed individually. Amberg et al. [2007] presented an algorithm in which each vertex is displaced separately by an affine transformation matrix, but with constraints. They introduced a stiffness, causing a vertex to be displaced along with its neighbors. The stiffness value decreases during the iterations, allowing a more elastic deformation. This results in a good geometric fit, but often poor correspondences.

In this chapter, a method for surface registration with automatic transfer of correspondences from the source to the target surface is described. The proposed framework extends Amberg's approach by splitting the registration step into a local and global part and by exploiting prior knowledge i.e. a shape model [Heimann and Meinzer, 2009] in elastic surface registration. The shape model has the advantage that realistic deviations of the mean are known. The combination with elasticity makes the framework more flexible and a better geometric fit is obtained with improved correspondences.

2.2 Methods

In this section, the developed framework is described. It extends the elegant algorithm of Amberg et al. [2007] by separating the global registration from the local registration step and adding a shape model prior, resulting in a more efficient algorithm. The framework is illustrated in Figure 2.1.

The surfaces are represented by triangle meshes and no landmark information

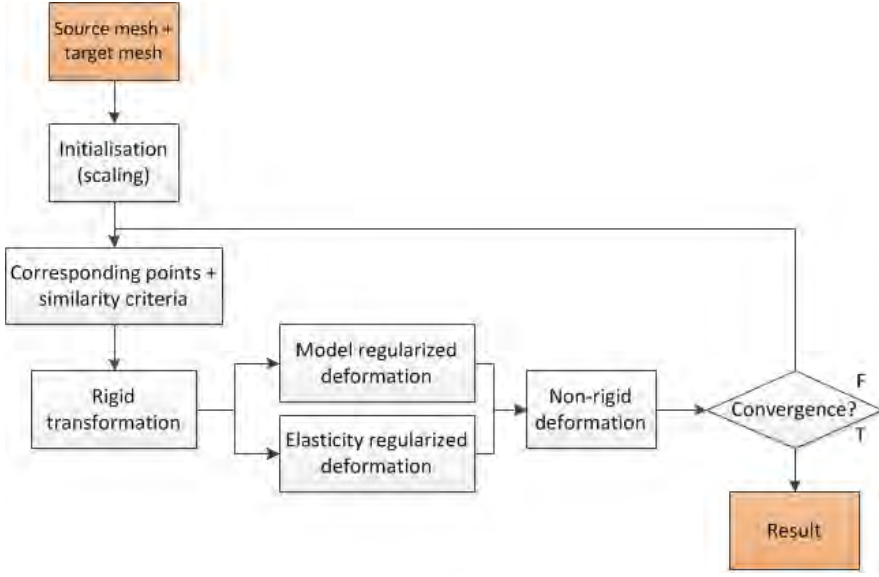


Figure 2.1: The framework of the proposed algorithm.

is used. The algorithm is however trivially expandable to include prior landmark correspondences cfr. Amberg.

2.2.1 Alignment Initialization

Before bringing the surfaces into correspondence, the reference surface is rigidly aligned to the target surface by matching their principal axes. Therefore the optimal rotation matrix and translation vector are calculated by following steps:

1. The centroids \mathbf{c}_S and \mathbf{c}_T of the uncentered source (\mathbf{S}^u) and uncentered target (\mathbf{T}^u) surface, respectively, are determined. These centroids are subtracted from each point of the surface to align both datasets to the center, resulting in the centered source matrix $\mathbf{S} \in \mathbb{R}^{3 \times n_S}$ and centered target matrix $\mathbf{T} \in \mathbb{R}^{3 \times n_T}$, with n_S the number of source vertices and n_T the number of vertices in the target surface.

$$\mathbf{c}_S = \frac{1}{n_S} \sum_{i=1}^{n_S} \mathbf{S}_{*,i}^u \quad (2.1)$$

$$\mathbf{c}_T = \frac{1}{n_T} \sum_{i=1}^{n_T} \mathbf{T}_{*,i}^u \quad (2.2)$$

2. The covariance matrices of \mathbf{S} and \mathbf{T} are computed, to obtain the symmetric matrices $\mathbf{\Sigma}_S \in \mathbb{R}^{3 \times 3}$ and $\mathbf{\Sigma}_T \in \mathbb{R}^{3 \times 3}$, respectively.

$$\mathbf{\Sigma}_S = \frac{1}{n_S - 1} (\mathbf{S} \cdot \mathbf{S}^T) \quad (2.3)$$

$$\mathbf{\Sigma}_T = \frac{1}{n_T - 1} (\mathbf{T} \cdot \mathbf{T}^T). \quad (2.4)$$

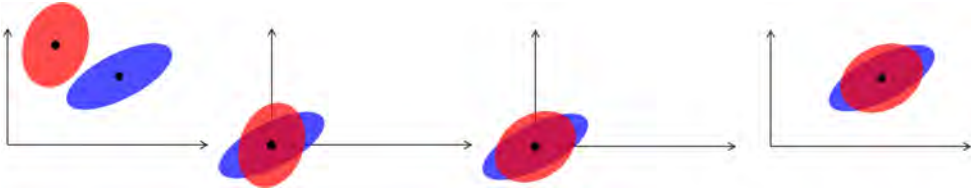


Figure 2.2: Schematic 2D visualization of the alignment of two surfaces. The red and blue ellipse represent the source and target surface, respectively. First, the centroids of both surfaces are calculated. Next, the surfaces are aligned to the origin. The following step is rotation of the source surface such that its principal axes align with those of the target surface. Finally, both surfaces are translated to the optimal location by the centroid of the source surface.

3. The singular value decompositions (SVD) of both matrices Σ_S and Σ_T are calculated to find the principal axes of each surface. The columns of both \mathbf{U}_S and \mathbf{U}_T correspond with the eigenvectors of Σ_S and Σ_T , respectively.

$$\Sigma_S = \mathbf{U}_S \mathbf{W}_S \mathbf{U}_S^T \quad (2.5)$$

$$\Sigma_T = \mathbf{U}_T \mathbf{W}_T \mathbf{U}_T^T \quad (2.6)$$

4. The rotation matrix \mathbf{R} is found by

$$\mathbf{R} = \mathbf{U}_S \cdot \mathbf{U}_T^T \quad (2.7)$$

and applied to the vertices of the source surface \mathbf{S} .

5. The source and target vertices \mathbf{S} and \mathbf{T} are translated by \mathbf{c}_S .

The alignment algorithm is schematically visualized in Figure 2.2.

2.2.2 Amberg

2.2.2.1 N-ICP-A

In Amberg et al. [2007], Amberg et al. presented the nonrigid optimal step iterative closest points (ICP) algorithm with affine transformation matrices (N-ICP-A). Each vertex undergoes a transformation, while motion is restricted by a stiffness factor β that regulates the strength of the connection with the neighboring vertices and which decreases during the iterations. In this way, the movement of neighboring vertices is constrained, resulting in similar movements for nearby vertices, as displayed in Figure 2.3. This affine transformation matrix implies also a global alignment.

By applying weights to each vertex, the importance of this vertex can be set. When there is no corresponding point found for a vertex of the target mesh, its weight is set to zero. In that case, this vertex simply translates along with its neighboring vertices. While many weighting schemes are possible, we used binary weights for simplicity, which were observed to be sufficient.

For a surface with n vertices and e edges, the algorithm works as follows. Let $\mathbf{X}_A \in \mathbb{R}^{3n \times 4}$ be a matrix that stores a 3×4 affine transformation matrix for each vertex of the source surface. \mathbf{X}_A can be determined by solving a linear system that consists of three expressions:

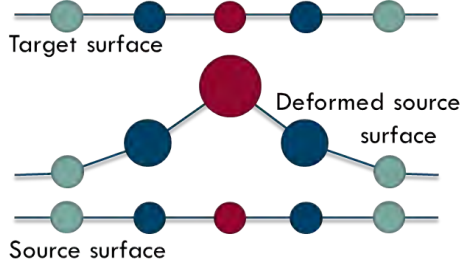


Figure 2.3: Schematic representation of elasticity. If one vertex, in this case the red dot, is transformed, the neighboring vertices are forced to move along with this vertex. The closest neighbors (blue dots) are the stiffest and move more than the distant neighbors (green dots).

- The stiffness term $E_s(\mathbf{X}_A)$ is the Frobenius norm $\|\cdot\|_F$ of the Kronecker product \otimes of incidence matrix $\mathbf{C} \in \mathbb{R}^{e \times n}$ and matrix $\mathbf{G} \in \mathbb{R}^{4 \times 4}$. \mathbf{C} indicates the start (-1) and end (+1) vertex of each edge. \mathbf{G} is a diagonal matrix $\text{diag}(1, 1, 1, 1)$. Hence:

$$E_s(\mathbf{X}_A) = \|(\mathbf{C} \otimes \mathbf{G})\mathbf{X}_A\|_F^2 \quad (2.8)$$

- The distance term $E_d(\mathbf{X}_A)$ is built up from a diagonal weight matrix $\mathbf{W} \in \mathbb{R}^{n \times n}$, which indicates the weight of each vertex. Let $\mathbf{V} \in \mathbb{R}^{n \times 4n}$ be a sparse matrix that holds the coordinate vectors \mathbf{v} of the source surface, with $\mathbf{v}_i = [x \ y \ z \ 1]^T$, where \mathbf{v}_i starts at position $(i, 4i)$ of \mathbf{V} . Furthermore, $\mathbf{T} \in \mathbb{R}^{n \times 3}$ holds the coordinates of the corresponding point for each vertex on the target surface. Then,

$$E_d(\mathbf{X}_A) = \|\mathbf{W}(\mathbf{V}\mathbf{X}_A - \mathbf{T})\|_F^2 \quad (2.9)$$

- The landmark term $E_l(\mathbf{X}_A)$ consists of $\mathbf{T}_L \in \mathbb{R}^{n \times 3}$ and $\mathbf{S}_L \in \mathbb{R}^{n \times 4n}$, which are the landmark matrices.

$$E_l(\mathbf{X}_A) = \|\mathbf{S}_L\mathbf{X}_A - \mathbf{T}_L\|_F^2 \quad (2.10)$$

The sum of the terms must be minimized. All terms together give a system that must be solved for \mathbf{X}_A :

$$\begin{bmatrix} \beta\mathbf{C} \otimes \mathbf{G} \\ \mathbf{W}\mathbf{V} \\ \gamma\mathbf{S}_L \end{bmatrix} \mathbf{X}_A = \begin{bmatrix} \mathbf{0} \\ \mathbf{W}\mathbf{T} \\ \mathbf{T}_L \end{bmatrix} \quad (2.11)$$

In Equation (2.11), β represents the stiffness factor that limits the deformation and γ is the landmark weight, used to control the importance of the landmarks. Landmarks are, however, not used in this chapter.

2.2.2.2 N-ICP-T

In the nonrigid optimal step ICP algorithm with translation vertices (N-ICP-T) of Amberg et al. [2007], the vertices are only allowed to translate, such that the geometric distance between those surfaces becomes minimal while retaining optimal point correspondences. This is a simplified version of the N-ICP-A method and results in larger geometric and correspondence errors, as rotation of the object is not possible. In the first stage, a closest point correspondence is presumed. Throughout

the iterations, the point correspondences gradually improve because of the improved geometric fit. The reference surface is uniformly resampled by the Poisson-disk sampling algorithm [Corsini et al., 2012; Cignoni et al., 2008]. A global rigid registration and an elasticity modulated registration are iteratively repeated. During the iterations, the stiffness gradually decreases, allowing the surface to become more elastic throughout the iterations to assure a robust registration algorithm. Hence, in the first iterations a rough alignment is performed to avoid getting stuck in a local minimum, while in the last iterations, the surface will be highly elastic to ensure a perfect geometric fit.

In the first step of the iterative process, the surfaces are rigidly aligned. To that end, corresponding points are found using normal-ray casting from each vertex of the reference surface to the target surface. The intersection point, that lies on the target surface and is not necessarily a vertex, may be a corresponding point. A number of constraints are imposed on the corresponding points:

1. The normal of the intersection has to point in the same direction (within a tolerance of 30°) as the normal of the source point.
2. The distance between corresponding points has to be smaller than $20\times$ the average distance between the two surfaces as measured from the previous iteration. In the first iteration, the previous average distance is set to infinity.
3. The casted ray may not intersect the source and target surface multiple times before reaching the corresponding point.

If no corresponding point is found, it has no influence on the alignment of the surfaces. Based on the corresponding points, a linear least squares alignment is performed to determine the transformation matrix that minimizes the distance between the corresponding points.

In the elastic part of the registration the vertices are allowed to move separately, while motion is restricted by a stiffness parameter β that regulates the strength of the connection with the neighboring vertices and which gradually decreases during the iterations. Hence, the movement of neighboring vertices is constrained, resulting in similar movements of neighboring vertices, as displayed in Figure 2.3. By applying weights to each vertex the influence of this vertex can be set. If no corresponding point for a vertex of the source mesh is found, its weight is set to zero. In that case, this vertex simply moves along with its neighboring vertices. Let n be the number of vertices of the surface and e the number of edges.

The weights corresponding to the vertices are stored as elements of the diagonal matrix $\mathbf{W} \in \mathbb{R}^{n \times n}$, which are either 0 or 1. In this algorithm, the weight can be either 0 or 1. Matrix $\mathbf{S} \in \mathbb{R}^{n \times 3}$ and matrix $\mathbf{T} \in \mathbb{R}^{n \times 3}$ hold the coordinates of the corresponding source and target vertices, respectively. The optimal translation vectors, the matrix $\mathbf{X}_T \in \mathbb{R}^{n \times 3}$, are found by solving following linear system:

$$\begin{bmatrix} \beta \mathbf{C} \\ \mathbf{W} \mathbf{I}_n \end{bmatrix} \mathbf{X}_T = \begin{bmatrix} \mathbf{0} \\ \mathbf{W}(\mathbf{T} - \mathbf{S}) \end{bmatrix}, \quad (2.12)$$

with $\mathbf{C} \in \mathbb{R}^{e \times n}$ the incidence matrix of the reference surface that indicates the start- and end vertex of each edge. The $n \times n$ identity matrix is denoted by \mathbf{I}_n . The rigid registration step and elastic registration steps are iteratively repeated until convergence is reached, which is calculated by comparing the current distance between

the source and reference surface d_t and the previous distance between the source and reference surface d_{t-1} . Convergence is reached if

$$\frac{|d_t - d_{t-1}|}{d_t} < 0.001.$$

2.2.3 Registration of Two Surfaces

Before building an SSM of a population of shapes, the surfaces need to be in correspondence with each other. This means that for every surface, the same point has to represent the same anatomical location. The goal of surface registration is to deform one surface to another while finding a meaningful mapping between the vertices of the surfaces, by maintaining the correspondences, as visualized in Figure 2.4. The distance between corresponding points on the target surface and the deformed source surface must be minimal.

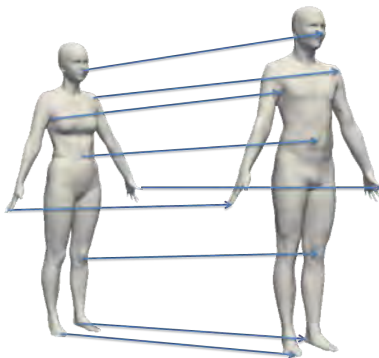


Figure 2.4: Visualization of surface correspondences.

First, a rigid registration is performed. The next part of the registration procedure is done by iteratively repeating a rigid registration combined with an elasticity modulated registration.

$$\mathbf{S}_i = (1 - \alpha) \cdot R(\mathbf{T}, \mathbf{S}_{i-1}) + \alpha \cdot E(\mathbf{T}, \mathbf{S}_{i-1}, \beta) \quad (2.13)$$

In Equation (2.13), $\mathbf{S}_i \in \mathbb{R}^{n \times 3}$ contains the coordinates of the vertices of the source surface at iteration i . Furthermore, $R(\cdot)$ and $E(\cdot)$ represent the rigid and elastic registration, respectively. The combination of both techniques is balanced with a weight factor $\alpha \in [0, 1]$. At the first stage of the registration, the rigid registration is more important. Later, the elastic registration becomes more apparent. During the iterations, α will increase and β will decrease. This makes that the elastic deformations will become more prominent with respect to the rigid transformation through the iterations. β is updated every u iterations.

$$u = \frac{N}{\beta_{start} - \beta_{end}} \quad (2.14)$$

with N the total number of iterations. β is determined by

$$\beta_i = \beta_{i-1} - \left(\frac{\beta_{start} - \beta_{end}}{N} \right)^2 \quad (2.15)$$

Appropriate values for these weights have been obtained empirically. For this chapter, α goes from 1 to 0 and β goes from 50 to 5. In Section 2.3.5, the influence of the stiffness term is investigated.

We will refer to the above algorithm as RN-ICP-T, because it combines a rigid registration and the N-ICP-T algorithm of Amberg. In the following subsection, the RN-ICP-T algorithm is discussed in more detail.

2.2.3.1 Rigid Registration

By this step, a rigid transformation is performed. First, in both surfaces corresponding points are identified. This is done by casting a ray along the normal $\mathbf{n}_s \in \mathbb{R}^3$ of a vertex of the source surface to the target surface. The intersection point does not have to be a vertex, but can be any location on the target surface. The direction of the normal $\mathbf{n}_t \in \mathbb{R}^3$ of this intersection point of the ray with the target surface is compared with the direction of \mathbf{n}_s by

$$d = \mathbf{n}_s \cdot \mathbf{n}_t \quad (2.16)$$

If the dot product $d > 0.5$, the points can be considered as corresponding points. Multiple intersections of the normal ray with the target surface are possible. The vertices with normals for which $d > 0.5$ and at the shortest Euclidean distance from each other, are corresponding points. The second constraint is that two points can only be corresponding if the line segment between them does not intersect the surface.

The corresponding points are mapped onto each other to find the optimal affine transformation matrix for the surface, by least-squares minimization. This means that the distance between corresponding points is minimal.

2.2.3.2 Elasticity Modulated Registration

Apart from a global transformation, also local deformations are needed to obtain an accurate geometric fit. It is implemented by using the N-ICP-T formula of Amberg's algorithm, which minimizes the difference between the translations of neighboring vertices.

We chose for the N-ICP-T algorithm because it has four times less linear equations than the N-ICP-A algorithm, what leads to a much shorter calculation time for solving the linear system. In combination with a rigid transform, N-ICP-T even gives an improved geometric fit and a smaller correspondence error regarding to the current state of the art.

2.2.4 Building a Statistical Shape Model

This part of our framework consists of building a statistical shape model based on the corresponded surfaces that resulted from the surface registration part. The process is shown in Figure 2.5. To build a shape model, it is important that the surfaces are superimposed by optimally translating and rotating the surfaces. The optimal poses are determined by Procrustes alignment [Dryden and Mardia, 2016; Gower, 1975; Kendall, 1989].

The model is built by performing principal components analysis (PCA) on the matrix containing the corresponding points to compute the eigenvectors and eigenvalues of the covariance matrix across all training shapes. This corresponding points

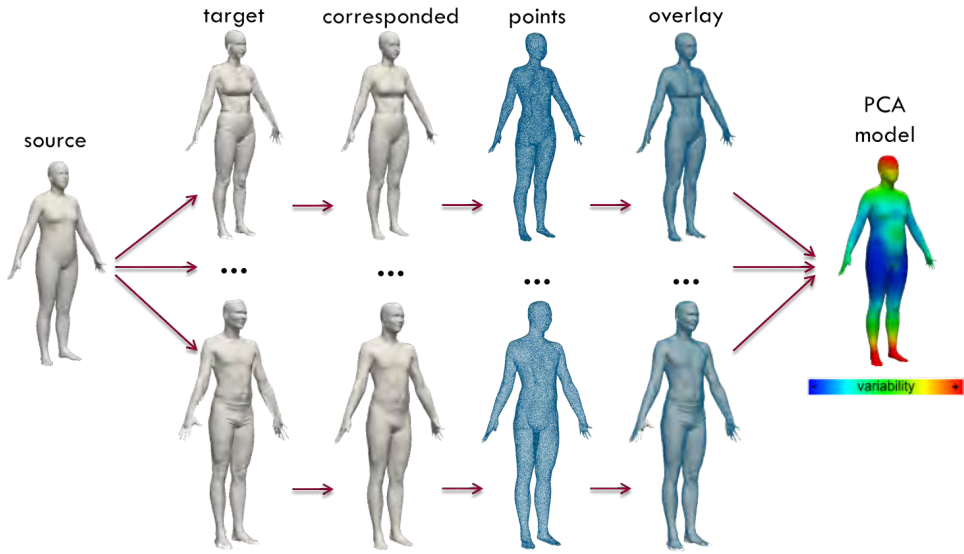


Figure 2.5: Framework for building a statistical shape model. First, a source surface is registered to each surface of the population. From these registered surfaces, a statistical shape model is built.

matrix $\mathbf{X} \in \mathbb{R}^{N \times 3n}$ is given by

$$\mathbf{X} = \begin{bmatrix} x_{0,0} & y_{0,0} & z_{0,0} & \cdots & x_{0,n} & y_{0,n} & z_{0,n} \\ x_{1,0} & y_{1,0} & z_{1,0} & \cdots & x_{1,n} & y_{1,n} & z_{1,n} \\ \vdots & \vdots & \vdots & \vdots & \vdots & \vdots & \vdots \\ x_{N,0} & y_{N,0} & z_{N,0} & \cdots & x_{N,n} & y_{N,n} & z_{N,n} \end{bmatrix},$$

with n the number of points and N the number of shapes. The i -th row of this corresponding points matrix is denoted by $\mathbf{x}_i \in \mathbb{R}^{3n}$.

In the statistical shape model, the mean surface $\bar{\mathbf{x}} \in \mathbb{R}^{3n}$ and the main variances $\mathbf{P} \in \mathbb{R}^{N \times 3n}$ are incorporated. The population of N shapes is represented by a point cloud with N points in an $3n$ -dimensional space, where each point represents a vegetable or fruit. This cloud can be represented by $N - 1$ eigenmode vectors, where the first eigenmode corresponds to the direction of the largest variance in the population, the second eigenmode corresponds to the second direction of the largest variance perpendicular to the first, etc.

The calculation of the statistical shape model is as follows. First, the average shape vector $\bar{\mathbf{x}}$ is calculated by

$$\bar{\mathbf{x}} = \frac{1}{N} \sum_{i=1}^N \mathbf{x}_i. \quad (2.17)$$

The normalized corresponding points matrix $\hat{\mathbf{X}} \in \mathbb{R}^{N \times 3n}$ is given by

$$\hat{\mathbf{X}} = \begin{bmatrix} \mathbf{x}_0 - \bar{\mathbf{x}} \\ \mathbf{x}_1 - \bar{\mathbf{x}} \\ \vdots \\ \mathbf{x}_N - \bar{\mathbf{x}} \end{bmatrix}.$$

Then, the normalized covariance matrix $\mathbf{V} \in \mathbb{R}^{N \times N}$ is computed as follows:

$$\mathbf{V} = \frac{1}{N-1} \hat{\mathbf{X}} \hat{\mathbf{X}}^T. \quad (2.18)$$

Next, the eigenvalues $\mathbf{\Lambda} \in \mathbb{R}^{N \times N}$ and eigenvectors $\mathbf{P} \in \mathbb{R}^{3n \times (N-1)}$ are obtained from the SVD of this covariance matrix \mathbf{V} as

$$\mathbf{V} = \mathbf{U}_V \mathbf{\Lambda}_V \mathbf{U}_V^T, \quad (2.19)$$

where $\mathbf{\Lambda} \in \mathbb{R}^{3n \times 3n}$ is the diagonal matrix that holds the eigenvalues corresponding to the eigenvectors in the columns of the matrix \mathbf{P} , which is calculated by

$$\mathbf{P} = \hat{\mathbf{X}} \cdot \mathbf{U}_V. \quad (2.20)$$

Any instance $\mathbf{y} \in \mathbb{R}^{3n}$, that lies in the shape space of the input population, can be approximated by the average surface $\bar{\mathbf{x}}$ and a weighted sum of principal component parameters \mathbf{P} as follows:

$$\mathbf{y} = \bar{\mathbf{x}} + \mathbf{P}\mathbf{b}, \quad (2.21)$$

where $\mathbf{b} \in \mathbb{R}^{N-1}$ holds the shape parameters, which are normally distributed with a certain standard deviation, calculated by PCA. This means that a new, realistic surface can be formed by adapting the shape model parameters.

2.2.5 Surface Registration with Shape Model Prior

In this section, the approach for registration with a shape model prior is discussed. A shape model contains more information than a single surface, so it is expected that this will give improved correspondences than registration starting from a single surface. The goal is to minimize the distance between the corresponding points, by deforming the shape model in combination with a further elastic deformation.

Surface registration with a shape model is done by combining a model regularized registration with an elasticity regularized registration to obtain good results on both geometric fit and correspondences. The elasticity regularized registration is the same as described before in Section 2.2.3.2, but the model regularized registration requires a different approach because the model variances are incorporated.

We will refer to the above algorithm by RNM-ICP-T. This algorithm is similar to the RN-ICP-T algorithm, but makes use of prior shape model knowledge instead of registration with a random source surface.

2.2.5.1 Model Regularized Registration

First, a fitting of the PCA model to the target surface is done, effectively deriving the contributions for each of the shape modes. The goal is to adjust the principal component contributions so that the model approaches the shape of the target surface.

The number of shape modes m that are included in each iteration i are calculated by following formula.

$$m_i = \text{ceil}\left(\frac{m_{i-1}}{4} \cdot \frac{4 \cdot (i + 1)}{N}\right) \quad (2.22)$$

where N stands for the total number of iterations. m_0 is the total number of shape modes of the shape model.

The model parameters \mathbf{b} can be found by solving

$$\mathbf{P}_{m_i}^T \cdot \mathbf{W} \in \mathbb{R}_{m_i}^{e \times v} \cdot \mathbf{b} = \mathbf{P}_{m_i}^T \cdot \mathbf{W}(\mathbf{t} - \bar{\mathbf{s}}) \quad (2.23)$$

In Equation (2.23), $\mathbf{W} \in \mathbb{R}^{3n \times 3n}$ is a diagonal matrix that holds the weights, $\mathbf{t} \in \mathbb{R}^{3n}$ holds the positions of the vertices of the target mesh and $\bar{\mathbf{s}} \in \mathbb{R}^{3n}$ holds the positions of the source mesh. $\mathbf{P}_{m_i} \in \mathbb{R}^{3n \times m_i}$ holds the first m_i shape modes. A new surface is formed by the mean shape and a linear combination of the principal components, with parameters \mathbf{b} .

The algorithm for registration with a shape model is a combination of both model regularized registration M and elasticity regularized registration E .

$$\mathbf{S}_i = (1 - \alpha) \cdot M(\mathbf{T}, \mathbf{S}_{i-1}) + \alpha \cdot E(\mathbf{T}, \mathbf{S}_{i-1}, \beta) \quad (2.24)$$

2.3 Evaluation

In this section, the results of the performed tests are described. Due to the large calculation time, only the results of the human head registration are compared with the N-ICP-A algorithm of Amberg. The framework is tested on the full body and specific body parts. Each registration technique is set to run for a minimum of 50 iterations and a maximum of twice the set number of iterations or when convergence is obtained. This is when the convergence ratio c is less than 0.0001. The calculation is based on the current (i) and previous ($i - 1$) mean distance d between the source and target surface.

$$c = \frac{d_i - d_{i-1}}{d_i} \quad (2.25)$$

In Section 2.3.3, tests are performed on the quality of the geometric fit, in Section 2.3.4 the quality of the correspondences and in Section 2.3.6 the execution time of the algorithm. The influence of the stiffness term and number of iterations are also tested in resp. Section 2.3.5 and Section 2.3.7.

2.3.1 Data Sets

For the performed tests, four classes of data sets are used. There are 106 full-body scans, 150 ear scans, 90 clavicle scans, and 100 head scans.

2.3.2 Shape Model

For this illustration, a shape model is built from 100 MRI scans of human heads, that are registered with one surface. The five first shape modes of the model are displayed in Figure 2.6.

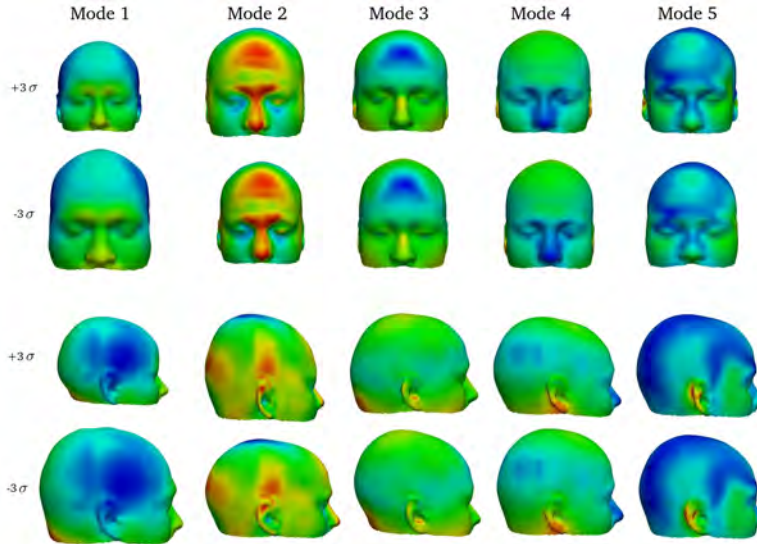


Figure 2.6: The first five eigenmodes of the head model, plus and minus 3 standard deviations (σ). The model is created from 100 surfaces. The colors indicate the magnitude of the landmark covariance tensor from blue (little variation) to red (many variation).

2.3.3 Evaluation of the Geometric Fit

It is important that the registration results in an accurate geometric fit. This means that the distance between the deformed source surface and the target surface must be minimal. In Table 2.1, the error on the geometric fit (in mm) from the deformed target surface on the source surface are summarized. There, the distance from each point of the deformed source mesh is measured to the closest point on the target mesh.

	N-ICP-A	RN-ICP-T	RNM-ICP-T
head	0.022 ± 0.006	0.006 ± 0.007	0.006 ± 0.001
body	-	0.092 ± 0.072	0.053 ± 0.040
ear	-	0.346 ± 0.334	0.095 ± 0.067
clavicle	-	0.065 ± 0.007	0.052 ± 0.005

Table 2.1: Geometric error (mm).

It can be seen that the proposed algorithms result in an improved geometric fit compared to the N-ICP-A algorithm.

2.3.4 Evaluation of the Correspondence Quality

For evaluating the correspondences, some characteristic points are annotated on the source mesh. The same anatomical locations are annotated on the target mesh. When the registration is done, these locations can be loaded again on the deformed mesh. The Euclidean distance between corresponding points in the target mesh and deformed source mesh is calculated. The smaller this distance, the better. In Figure 2.7, the validation of the correspondences is shown for a typical surface.

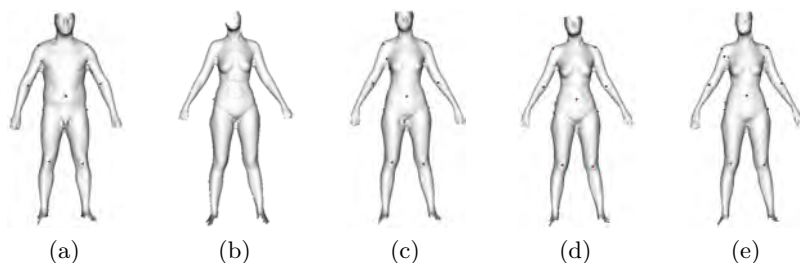


Figure 2.7: Validation of the correspondences, displayed by an example. The source and target surface are displayed in Figure 2.7a and Figure 2.7b respectively. Figure 2.7c shows the annotations on the result of RN-ICP-T and Figure 2.7d for the result of RNM-ICP-T. Figure 2.7e is the result of N-ICP-A.

With N-ICP-A, the vertices are deformed to the closest point without aligning the surface features properly. While it leads to negligible geometric errors, the correspondence error is generally large. This is clearly visible in the shoulder area in Figure 2.7e. When using a shape model, the surfaces are globally well registered before local deformations are allowed.

In Table 2.2 the results of the tests are shown. The algorithm is performed on 10 surfaces of each class. The mean correspondence error (in *mm*) is displayed in the table.

	N-ICP-A	RN-ICP-T	RNM-ICP-T
head	6.13 ± 1.16	4.23 ± 0.89	4.14 ± 0.89
body	-	26.84 ± 3.61	25.88 ± 3.35
ear	-	4.09 ± 2.75	2.18 ± 0.51
clavicle	-	4.42 ± 1.33	4.50 ± 1.36

Table 2.2: correspondence error (mm)

The N-ICP-A algorithm of Amberg gives significantly larger errors. This is because there is no overall rigid alignment step, so the chances are higher that the source vertices migrate to a wrong position on the target vertex. Once such an error is made, the algorithm is not capable of repairing this. The proposed technique makes use of a separate, overall rigid step and also a global non-rigid registration by the shape model, which makes the registration more robust.

Evidenced by the results, the RN-ICP-T and RNM-ICP-T algorithms give the smallest errors. The results of the RNM-ICP-T algorithm are the most stable. It is clear that the algorithm of Amberg gives the worst results on correspondence.

2.3.5 Evaluation of the Sensitivity of the stiffness

For this test, the stiffness value evolves from 50 to 5. This value is empirically determined. The smaller the stiffness value, the more freely the vertices can move. The influence of the stiffness depends on the number of triangles on the surface. The more triangles, the smaller the distance between neighboring points. This means that a surface with many triangles will be less elastic than a surface with less triangles. When a surface is highly curved, finding corresponding points will be more difficult

and it is less likely that all corresponding points can be found. In that case it is better that the source surface migrates slowly to the target surface to reduce the chance on errors. Once a vertex has migrated to the wrong corresponding point, this fault is less likely to be repaired. The more similar the surfaces, the more elastic the source surface can behave. In any case, it is best to end with a small stiffness value close to 5.

In Figure 2.8, the influence of the stiffness value is tested on 10 clavicle surfaces. The RNM-ICP-T algorithm ran from a start value of 100 to an end-value $\in [0, 100]$, with a step size of 5. The algorithm also ran from a start value $\in [0, 100]$ to an end value of 0. In Figure 2.9 the influence of the stiffness factor is shown on a highly simplified surface.

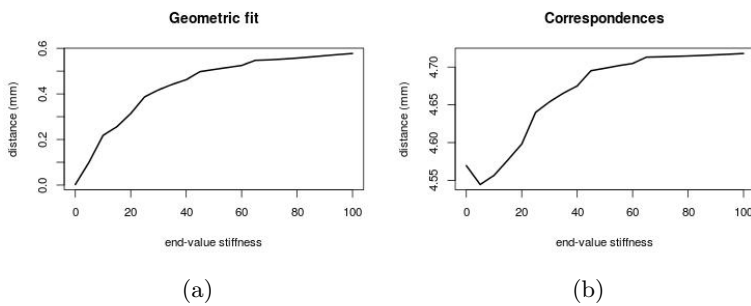


Figure 2.8: Evaluation of the influence of the end stiffness value, tested on 10 clavicle surfaces.

It is clear that it is best to end with a small stiffness value. From Figure 2.8b, it can be observed that a stiffness value of 0 gives a worse result on correspondences than a value of 5. This is because the vertices have too much freedom to migrate to an inaccurate position, due to drift of the vertices because there are no restrictions. On the other hand, ending with a stiffness of 0 gives the best results on geometric fit. For the start stiffness value has little influence on the results, but a starting with a low stiffness value (less than 20) results in too much freedom of movement and a high stiffness value (more than 80) leads to a registration that is too rigid. From tests it

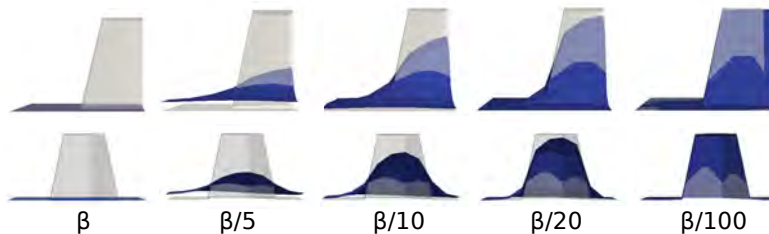


Figure 2.9: Influence of the elasticity parameter on the elastic surface deformation, shown from two viewpoints. In each figure, the target surface is visualized in transparent white and the deformed source in blue. The left example is created with a very high stiffness factor. The right example is created with a very low stiffness factor. From left to right, the stiffness factor decreases.

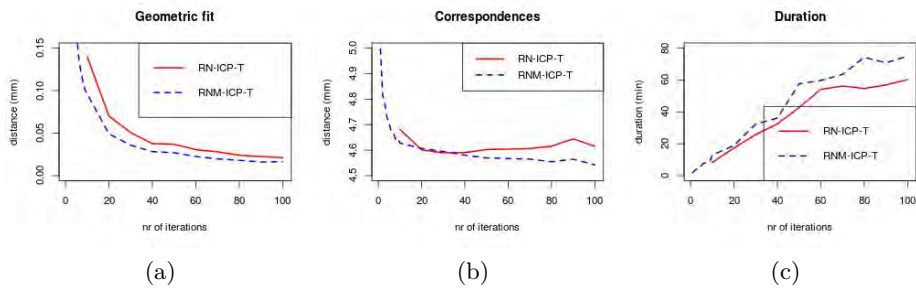


Figure 2.10: The more iterations, the smaller the geometric error. It is seen in Figure 2.10a that this applies to both RN-ICP-T and RNM-ICP-T. Figure 2.10b shows that the correspondence error decreases more for RNM-ICP-T than for RN-ICP-T. The execution time of both algorithms increases linearly, as seen in Figure 2.10c.

turned out that a start value of 50 gives acceptable good results on correspondence and geometric fit for all types of surfaces.

2.3.6 Evaluation of the Timing

The execution time of the algorithm depends on the number of vertices, because this determines how many times there must be searched for corresponding points and the size of the linear system. A test is performed on 10 surfaces, registered by the three techniques for 50 iterations. The results are shown in Table 2.3.

	N-ICP-A	RN-ICP-T	RNM-ICP-T
head	578 ± 102	14 ± 4	16 ± 4
body	-	5 ± 1	6 ± 1
ear	-	166 ± 62	127 ± 30
clavicle	-	12 ± 2	15 ± 2

Table 2.3: Run times of the algorithm (min)

Amberg’s algorithm has the largest calculation time. The most time consuming parts of the RN-ICP-T and RNM-ICP-T algorithms are the solving of the linear system and the determination of the corresponding points. Solving the linear system takes about 1/3 of the total time of an iteration. The determination of the corresponding points takes about 1/3 of the time for as well the rigid as elastic registration. For Amberg’s algorithm, the solving of the linear system takes most of the time, about 99% of the total time of an iteration. In our implementation, this is because the number of unknowns is four times larger relative to the one used in this presented framework. This leads to a factor 40 increment in time, compared to the proposed algorithms in this chapter.

2.3.7 Influence of the Number of Iterations

For the previous tests, the RN-ICP-T, RNM-ICP-T and N-ICP-A algorithms ran 50 iterations. The number of iterations determines how fast the stiffness decreases and the weight factor α increases, because these parameters evolve linearly to a fixed end

value. During the first iterations, the registration is more global because of the low weight factor α and the small number of eigenmodes. At the end it becomes elastic and the deformation is more refined.

When the number of iterations is small, e.g. less than 30, there is not much time to obtain a good rough and fine registration. This may lead to an inexact registration. On the other hand, by setting the number of iterations too high the algorithm will take too long without improvement with respect to less iterations. The number of iterations will depend on the desired precision of the surface registration.

Tests are performed on registration of 10 surfaces of the human head. Each surface is registered by 10 to 100 iterations, with a step size of 10. For RN-ICP-T, the number of iteration only has a significant influence on the geometric fit and the execution time. There is no improvement on correspondences, while the geometric fit gets better. When registering with a shape model, the correspondences also improve over the iterations. These factors must be taken into account when choosing the number of iterations. For our applications, 50 iterations is sufficient.

2.4 Conclusion

In this chapter, two new techniques for surface registration were described. They proved to score well on geometric fit, correspondences, and duration, compared to the N-ICP-A algorithm of Amberg. Another advantage over Amberg's algorithm is that the proposed algorithms run about 40 times faster.

The optimal stiffness value depends on the type of surface, or more specifically the number of triangles and the curvature on the surface. The optimal number of iterations also depends on the type of surface and the application. The more similar the surfaces, the fewer iterations are needed for good correspondences and a good geometric fit. For the tests in this chapter, all surfaces are resampled to 10000 vertices, which makes that all surfaces could be registered with the same start and end stiffness value.

The choice of the number of iterations depends on the desired accuracy of the results. More iterations will yield improved results on correspondence and geometric fit, but the execution time will increase. The tests show that 50 iterations gives good results within an acceptable time frame for each class of surfaces considered in this chapter.

Acknowledgment

The authors would like to thank Amit Bernat M.D. for the clavicle scans and Philips for the ear scans.

This work was previously published as:

Danckaers, F., Huysmans, T., Van Dael, M., Verboven, P., Nicolai, B., and Sijbers, J. (2015). Building a Statistical Shape Model of the Apple from Corresponded Surfaces. Chemical Engineering Transactions, 44:49–54.

3

Evaluation of 3D Body Shape Predictions Based on Features

Contents

Abstract	32
3.1 Introduction	33
3.2 Methods	33
3.2.1 Shape prediction	33
3.3 Evaluation	34
3.3.1 Shape Model	34
3.3.2 Feature Validation	36
3.4 Conclusion	40

Abstract

The human body comes in many sizes and shapes. For design purposes, it is useful to be able to quickly simulate a virtual mannequin of a customer. A statistical shape model can be used for this purpose, because it describes the main variations of body shape inside the model's population. From this model, the specific features of each person in the population are known. Therefore, a mapping between the shape model parameters and specific features can be calculated, which allows adjusting the body shape, in an intuitive way. In this work, we have investigated how accurate a body shape can be predicted based on a set of features and which features are most suitable for this purpose. Height, weight, and hip circumference appeared to be the most suitable features to accurately predict the body shape.

3.1 Introduction

When designing a near-body product, it is useful to be able to quickly simulate a virtual mannequin of a customer [Domingo et al., 2014]. This mannequin must closely resemble the actual body shape of the customer. Such models (Digital Human Modeling Tools - DHM) are already available [Blanchonette, 2010; Moes, 2010; Van Der Meulen and Seidl, 2007; Park et al., 2015], but their applicability is still limited. Indeed, the current models are a simplified representation of the body and the 3D variation in shape of the population is usually not included. Moreover, the changes in shape are often univariate (body stature). As a result, they are not suitable for the design of products while focusing on comfort.

Detailed, realistic models are not available yet, but would have an added value for the design process. These models should be accurate, easy to adjust and require a minimum number of parameters [Otake et al., 2015; Ma and Luximon, 2014; Wuhrer and Shu, 2013].

During the design process, the products could be virtually validated with a broad range of body shapes included in the body model. A statistical shape model [Cootes et al., 1995] of the population is an elegant approach to obtain detailed mannequins that are adjustable in body shape [Blanc et al., 2012; Lacko et al., 2015].

In this work, we evaluate a data-driven technique to extract specific feature parameters from a statistical shape model [Liu et al., 2014]. We have investigated how accurate a body scan can be predicted based on measured features and which features are most suitable for this purpose.

3.2 Methods

3.2.1 Shape prediction

Each subject of the population has specific shape model parameters and specific features. A link between the shape model parameters and features is sought by multiple multivariate linear regression, so a specific feature is represented by a linear combination of eigenmodes. Such a feature vector can be calculated. As a result, a specific feature, such as the height of a person, can be adapted by multiplying this feature vector with a factor.

Suppose we know F features $\mathbf{f}_i = [f_1 f_2 \cdots f_F]^T \in \mathbb{R}^{F+1}$ and the PC weights $\mathbf{b}_i \in \mathbb{R}^{N-1}$ of each shape i from the dataset. Then, a mapping matrix $\mathbf{M} \in \mathbb{R}^{(N-1) \times (F+1)}$, describing the relationship between the PC weights matrix $\mathbf{B} = [\mathbf{b}_1 \mathbf{b}_2 \cdots \mathbf{b}_N] \in \mathbb{R}^{(N-1) \times N}$ and the feature matrix $\mathbf{F} = [\mathbf{f}_1 \mathbf{f}_2 \cdots \mathbf{f}_N] \in \mathbb{R}^{(F+1) \times N}$ is calculated by

$$\mathbf{M} = \mathbf{B}\mathbf{F}^+, \quad (3.1)$$

where \mathbf{F}^+ is the pseudoinverse of \mathbf{F} [Allen et al., 2003]. With this mapping matrix, new PC weights \mathbf{b} can be generated from given features \mathbf{f} by

$$\mathbf{b} = \mathbf{M}\mathbf{f}. \quad (3.2)$$

Feature-specific vectors were calculated. By adapting the weights of these vectors, the most plausible body shape is simulated. We performed two experiments to validate the feature-shape modeling. First, the extracted feature-specific vectors were varied from -3 to $+3$ standard divisions and visualized on the body as a color map. Second,

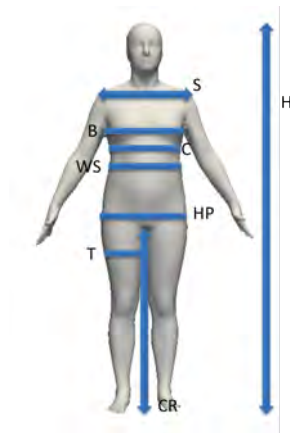


Figure 3.1: Features used in this chapter

a body surface was predicted from a subset of its features and compared to the ground truth, to find the most relevant features for body shape prediction. The comparison was done by calculating the Euclidean distance between the corresponding points of the predicted shape and its ground truth.

3.3 Evaluation

3.3.1 Shape Model

To validate the technique, we used 290 3D scans (145 men and 145 women) from a Dutch population in standing pose from the CAESAR database. The specific features of each person were known. The features used in this chapter were gender (G), age (A), height (H), weight (W), waist circumference (WS), chest circumference (C), hip circumference (HP), thigh circumference (T), crotch height (CR), shoulder breadth (S), and breast circumference (B). The measurements are shown in Figure 3.1.

The surface registration algorithm was performed for 60 iterations. From the registered surfaces, a statistical shape model was built. The first four shape modes of the CAESAR body model are displayed in Figure 3.2. The colors indicate the amount of variation on that location on the surface for the specific eigenmode. The first mode represents mainly height and gender, while the second mode represents mainly weight and gender. It is not possible to link a specific feature with a specific mode. A specific feature consists of a linear combination of multiple eigenmodes.

The largest variations of the body shape are described in the first modes of the model. This is validated by calculating the compactness of the shape model. The compactness measure describes how the model captures the variation. The compactness test results are visualized in Figure 3.3 and shows that the model captures more than 90% of the shape variation within the first six modes.

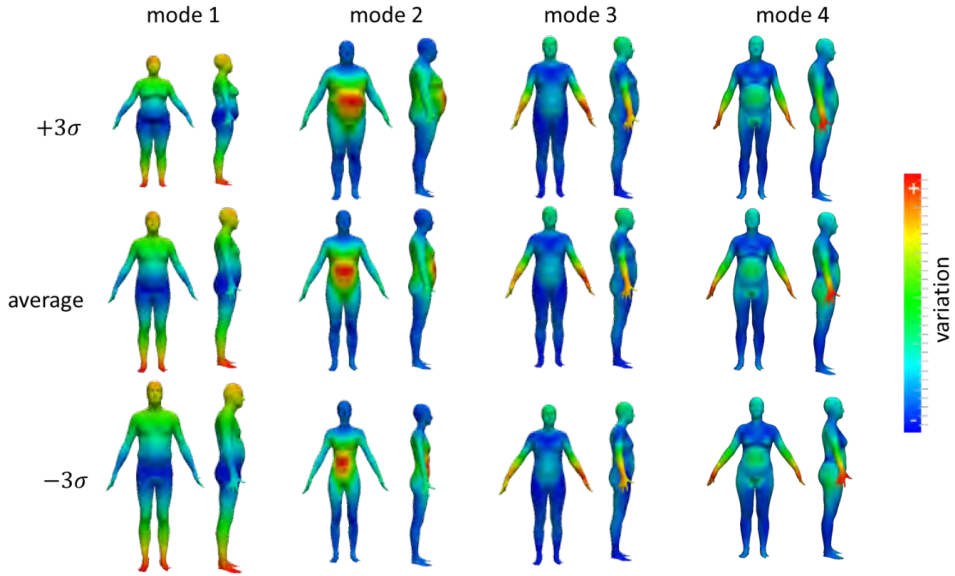


Figure 3.2: First 4 eigenmodes of the statistical body shape model.

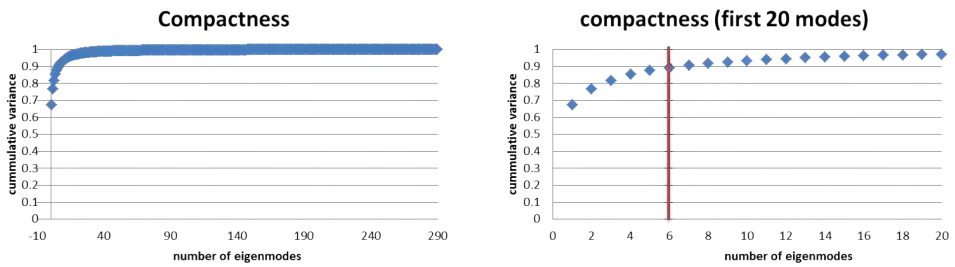


Figure 3.3: Compactness of the model.

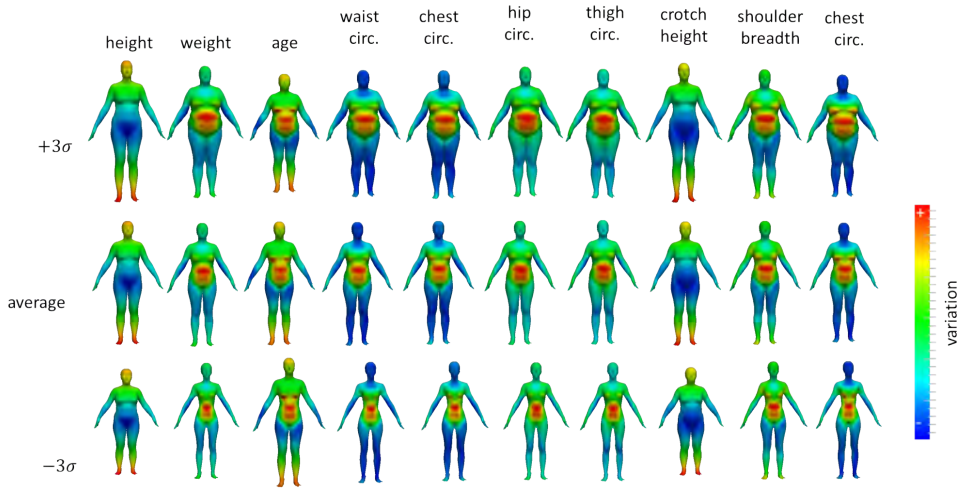


Figure 3.4: Feature vectors male + female.

3.3.2 Feature Validation

3.3.2.1 Feature vectors

First, we extracted the feature vectors from the model, using the given features of each sample of the training set. The features of the complete shape model are shown in Figure 3.4. We could observe a difference in gender for extracting the feature vector. In the male population (Figure 3.5), a change in weight affects the whole upper body, while in the female population (Figure 3.6) weight change is more prominent around the waist.

From these results, we can observe some linear relations between features. Visually, it can be observed that a correlation exist between waist circumference, breast circumference, and chest circumference. There is also a correlation between gender and height. However, no correlation can be observed between breast circumference and height. In Figure 3.7, the relationship between the features is displayed as a pair plot. For each pair of features, the Pearson correlation coefficient is calculated.

From the results of the pair plot we can conclude that there is indeed a high correlation between waist circumference, breast circumference, and chest circumference. However, age has little influence on the overall body shape, because there is no significant correlation with any other feature. Height, too, has little influence on the shape since it is only correlated with crotch height.

Furthermore, a difference in gender can be distinguished. For the male population, there is a very high correlation between chest circumference and breast circumference. However, the correlation is less distinct for the female population. Another notable difference is that for the same weight, women have a larger hip circumference and thigh circumference than men, which could also be visually observed from the previous figures.

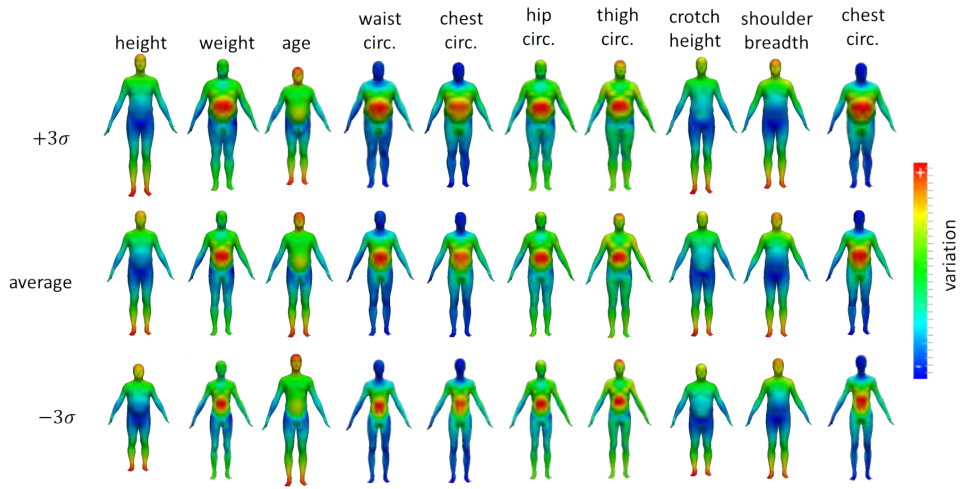


Figure 3.5: Feature vectors male.

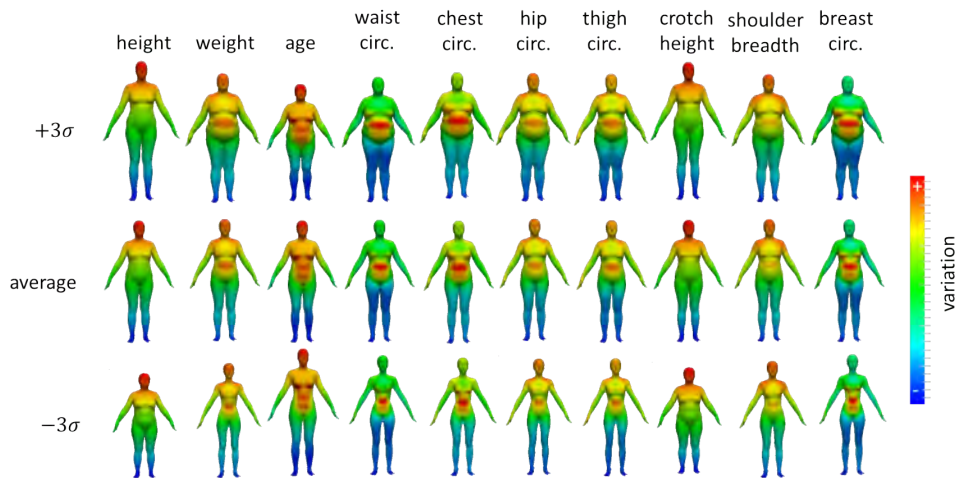


Figure 3.6: Feature vectors female.

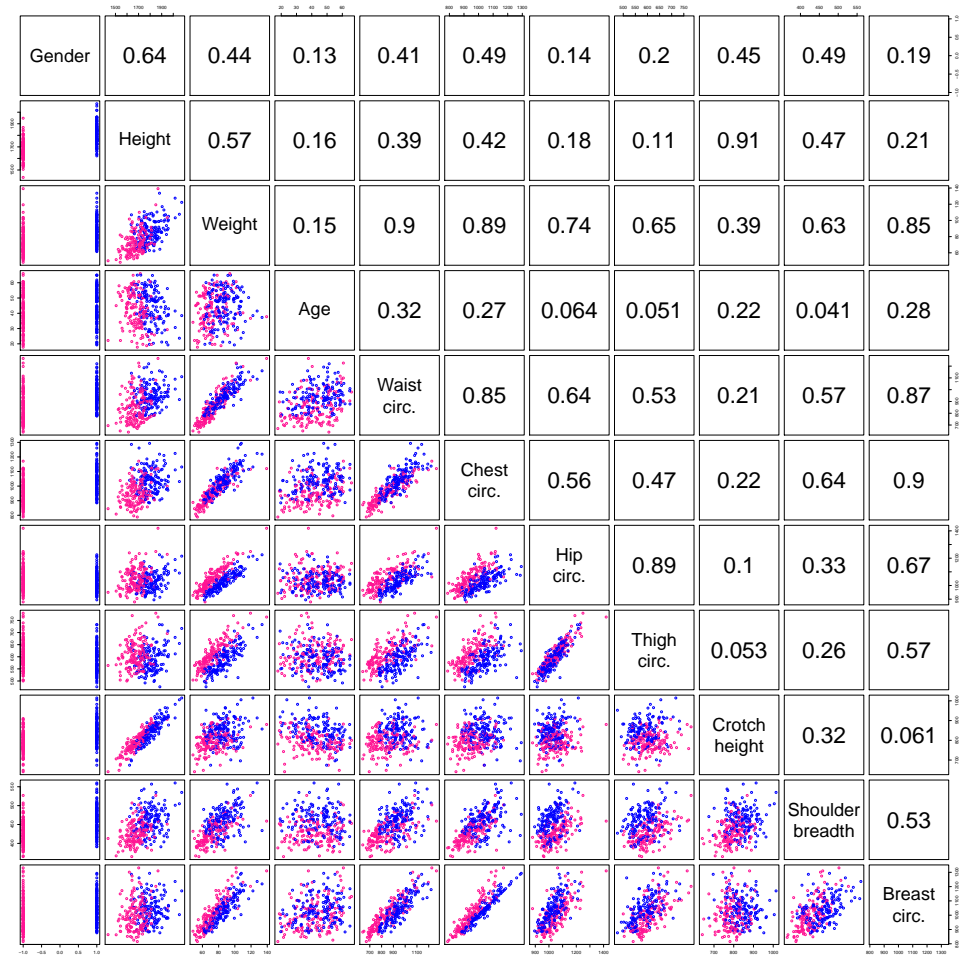


Figure 3.7: Pair plot of features. Pink denotes female subjects and blue denotes male subjects. For each pair of features, the Pearson coefficient is displayed.

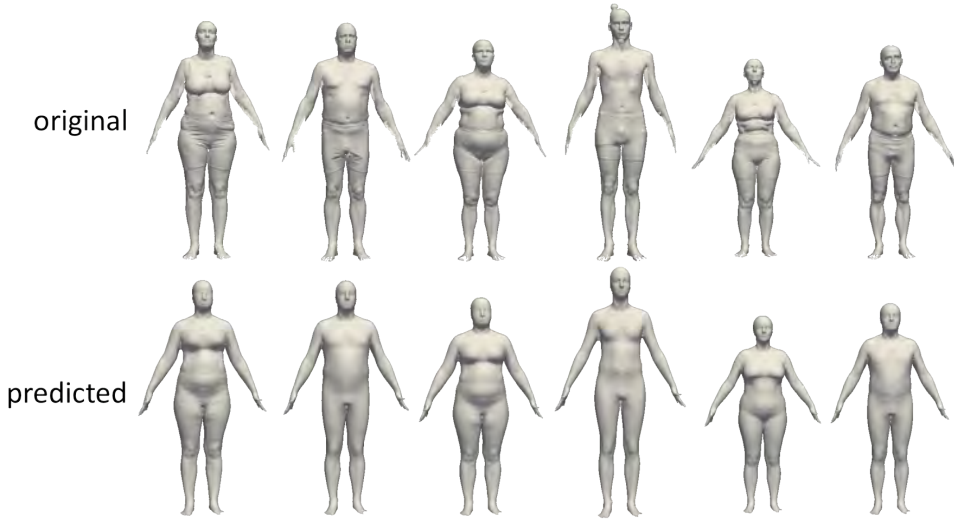


Figure 3.8: examples of predicted shapes.

3.3.2.2 Shape Prediction

This experiment is performed to find the most useful features to predict a body shape. In Figure 3.8, some of the predicted shapes from the test set are displayed. All features were used to predict these surfaces.

This experiment is performed with 10 subjects (5 men and 5 women), not included in the training set. Each surface is predicted from a subset of its features. The predicted surface is compared to the original surface, by calculating the Euclidean distance between both surfaces as a better prediction results in a smaller Euclidean distance. The best performing features were calculated by predicting the surface from all possible combinations of its features. The prediction errors for the optimal combinations are summarized in Table 3.1.

H	H W	H W HP	G H W HP	G H W HP S	G H W C HP S	G H W A HP CR S	G H W A HP T CR S	G H W A C HP T CR S	G H W A WS C HP T CR S
12.16± 3.32	10.34± 2.47	9.25± 2.18	9.10± 2.09	9.07± 2.04	9.17± 1.96	9.09± 2.27	9.17± 2.31	9.18± 2.17	9.24± 2.25

Table 3.1: Mean error when predicting a surface using optimal combination of features (in mm). G = gender, H = height, W = weight circumference, A = age, WS = waist, C = chest circumference, HP = hip circumference, T = thigh circumference, CR = crotch height, S = shoulder breadth, B = breast circumference.

We can deduct from the results in Table3.1 that height, weight, and hip circumference



Figure 3.9: Mean errors for the predicted surfaces of Table 3.1 in *mm*.

are important features to predict the body shape. Breast circumference and thigh circumference have little influence on the quality of the predictions, or even lead to worse shape predictions due to overfitting. The mean surface errors for above predictions, projected on the average body are visualized in Figure 3.9.

The largest errors appear around the arms, due to differences in pose. Pose normalization is not included in the shape model.

3.4 Conclusion

In this work, we built a shape model that is adjustable in shape by intuitive parameters. Strong correlations exist between gender and height, and waist circumference, breast circumference and chest circumference, whereas no correlation was observed between breast circumference and height.

With this algorithm, it is possible to predict the most plausible shape. Height, weight, and hip circumference are the most relevant features to predict the shape of a person. The largest errors appear at the arms, due to differences in pose. In future work, the prediction will be improved by incorporating pose normalization in the shape model.

This work was previously published as **Danckaers, F., Huysmans, T., Hallemaans, A., De Bruyne, G., Truijen, S., and Sijbers, J. (2018a). Full Body Statistical Shape Modeling with Posture Normalization. In Advances in Intelligent Systems and Computing, volume 591, pages 437–448. Springer, Cham**

4

Posture Normalization of 3D Body Scans

Contents

Abstract	42
4.1 Introduction	43
4.2 Methods	44
4.2.1 Identity Removal	44
4.2.2 Posture Normalization	45
4.3 Evaluation	46
4.3.1 Statistical Shape Model	46
4.3.2 Posture-normalized Shape Model	46
4.3.3 Posture Normalization Case	46
4.3.4 Model Performance - Compactness	48
4.3.5 Feature Selection	48
4.4 Discussion	57
4.5 Conclusion	61

Abstract

Realistic virtual mannequins that represent body shapes within a target population, are valuable tools for product developers. Statistical shape modeling is a promising approach to map out the variability of body shapes. Unfortunately, the shape variation captured by statistical shape models (SSMs) of human bodies is often polluted by variations in posture, which negatively affects the compactness of those models. In this chapter, we propose a framework that has low computational complexity to build a posture invariant SSM, by capturing and correcting the posture of an instance. The posture-normalized SSM is shown to be substantially more compact than the non-posture-normalized SSM.

4.1 Introduction

When scanning people in standing pose, posture differences may occur over the population. If SSMs are built from these 3D scans, body posture will have a significant and often undesired influence on the shape modes. Even when the subjects are instructed to maintain a standard pose, slight posture changes are unavoidable, especially in the region of the arms. As a result, some shape variances are unintendedly correlated with posture. Posture changes are, for example, also present in the Civilian American and European Surface Anthropometry Resource (CAESAR) database [Robinette et al., 1999]. In addition, this results in a non-compact model, as posture variances lead to large deviations from the mean shape. Therefore, it is less suitable for e.g. classification applications, where a new subject is assigned to a specific body shape group. Furthermore, the computational cost when using more compact SSM will be significantly reduced as less modes are necessary to describe the population. The main goal of this chapter is to construct posture invariant SSMs from a set of 3D body scans. Most posture normalization techniques are based on rotating and translating the body parts, such as arms and legs. In particular, applying linear blend skinning (LBS) to a surface mesh with a simplified skeleton consisting of joints and bones, is a popular approach [Baran and Popović, 2007]. Thereby, posture is commonly normalized by transforming each bone separately. For every bone of the skeleton, a smooth weight map is assigned to the vertices of the 3D body shape. The vertices are subsequently transformed along with the bone and relative to the assigned weights. The disadvantage of LBS is that the result may appear unnatural, because LBS cannot compensate for muscle bulging (except when introducing helper bones, which is cumbersome) and joint rotations may produce a collapsing effect where the skin collapses to a single point, also known as the candy-wrapper artifact [Mohr and Gleicher, 2003].

Another common approach is separating the shape space from the posture space. Wuhler et al. [2012] and Pishchulin et al. [2017] did a posture-invariant shape analysis using the Laplace operator. They optimized the Laplacian coordinates of the average shape of the model, $\bar{\mathbf{X}}$, to be as close as possible to every corresponded input shape \mathbf{X}_i . This leads to meshes that have the body shape of \mathbf{X}_i and the posture of $\bar{\mathbf{X}}$, which is very computationally intensive for surface meshes with many vertices, because an optimization problem needs to be solved for every vertex.

The SCAPE method [Anguelov et al., 2005] is a data-driven method that assumes the body shape and posture to be uncorrelated. The advantage of this technique is that it generates more realistic shapes including the simulation of muscle bulging. However, by considering shape and pose deformations separately, it is not accurate since pose deformation is person-dependent. Another drawback of SCAPE is that it is time-consuming (compared to e.g. LBS) as a least-squares system needs to be solved in order to reconstruct a surface from pose and shape parameters. On the other hand, Chen et al. [2013] generated a tensor-based model, which jointly models shape and pose deformations. The resulting surfaces look more realistic after pose deformation compared to using the SCAPE method. Reed et al. [2016] developed a pose modification technique by calculating a mapping matrix between two SSMs of the same population in a different pose. However, the posture of the input shapes has a high influence on their results. By first applying posture normalization, more accurate results are obtained by pose modification.

In this chapter, we propose a fast, skeleton-less, data-driven method to perform

statistical shape modeling in a posture invariant way by minimizing the influence of posture.

4.2 Methods

In this section, a framework to obtain posture invariant SSMs is described. It is illustrated in Figure 4.1. First, an SSM is built from a population of 3D human body shapes [Danckaers et al., 2014]. The posture of the average shape is defined as the "average posture" and will be the targeted posture in the remainder of this chapter. Next, the identity of these shapes is removed, by modifying the appearance of each shape so that its new features (such as height, weight, gender, etc.) are equal to those of the average shape. Then, the feature normalization technique is described. From the resulting shapes without identity, a posture model is built. This model captures the variation of postures throughout the input population. If such a model is registered to a new input shape, then only posture is retained. Next, the deformation from the captured posture to the average posture is calculated and applied to the input shape, which results in a posture-normalized shape.

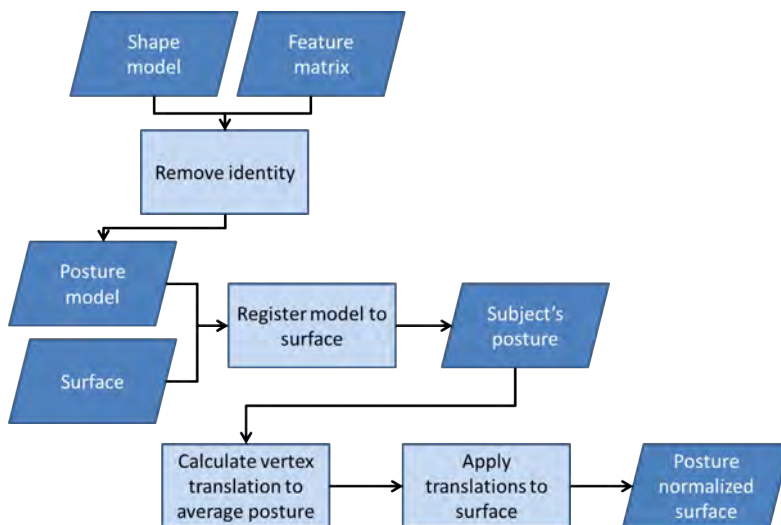


Figure 4.1: The proposed framework for building posture invariant SSMs.

4.2.1 Identity Removal

By removing the identity of each body scan, shape specific deformations are filtered out and only posture related deformations remain. To do so, the features of each shape are adjusted so that they are equal to the features of the average shape of the dataset. As a result, all shapes look similar.

First, the specific PC weight vector \mathbf{b}_i of instance i is extracted from the PC matrix \mathbf{B} . Second, the delta feature vector $\Delta\mathbf{f}$, which is the vector that holds the values that should be added to the current features to become equal to the average features, is calculated by extracting the specific features \mathbf{f}_i (defined as the i th column of \mathbf{F}) of

instance i from the average features $\bar{\mathbf{f}}$ of the population:

$$\Delta\mathbf{f} = \bar{\mathbf{f}} - \mathbf{f}_i. \quad (4.1)$$

Next, the delta PC weights vector $\Delta\mathbf{b}$ that should be added to the current PC weights to adjust the body shape, is calculated by multiplying the mapping matrix \mathbf{M} with the calculated delta features $\Delta\mathbf{f}$:

$$\Delta\mathbf{b} = \mathbf{M} \cdot \Delta\mathbf{f}. \quad (4.2)$$

These delta weights are subsequently added to the original PC weights \mathbf{b}_i to obtain the PC weights \mathbf{b}'_i of the shape with average features:

$$\mathbf{b}'_i = \mathbf{b}_i + \Delta\mathbf{b}. \quad (4.3)$$

Finally, new shapes without identity, \mathbf{x}'_i , are calculated by multiplying the new weights \mathbf{b}'_i with the PC vectors \mathbf{P}_s of the SSM and adding them to the mean shape $\bar{\mathbf{x}}$:

$$\mathbf{x}'_i = \bar{\mathbf{x}} + \mathbf{P}_s \mathbf{b}'_i. \quad (4.4)$$

From the set of shapes without identity, a new SSM is built [Danckaers et al., 2014] that represents a posture model. The result is a posture model, whose variances are mainly the posture variances.

4.2.2 Posture Normalization

To normalize the posture of a shape, that shape is corresponded with the statistical posture model by elastic surface registration [Danckaers et al., 2014]. Note that the posture model and the new shape do not have to stem from the same dataset. It is sufficient that they have roughly the same pose. From the corresponded posture model, the PC weights are calculated. Because this model mostly contains posture variations, only the posture of the target shape is captured.

First, the input shape, \mathbf{x}_i , is scaled, such that it has the same height as the posture model. Then, the posture PC weights \mathbf{b}_i of \mathbf{x}_i are calculated by multiplying the inverse PC matrix \mathbf{P}_p of the posture model by the distance vector between each vertex of the input surface mesh and the mean surface mesh $\bar{\mathbf{x}}$. These posture PC weights only denote differences in posture compared to the mean posture.

$$\mathbf{b}_i = \mathbf{P}_p^T (\mathbf{x}_i - \bar{\mathbf{x}}). \quad (4.5)$$

Next, the posture \mathbf{x}'_i of the input shape is reconstructed from the calculated posture PC weights \mathbf{b}_i :

$$\mathbf{x}'_i = \bar{\mathbf{x}} + \mathbf{P}_p \mathbf{b}_i \quad (4.6)$$

Finally, the normalized shape $\hat{\mathbf{x}}_i$ is calculated by subtracting the posture influence $\mathbf{P}_p \mathbf{b}_i$ on the shape from the original shape \mathbf{x}_i :

$$\hat{\mathbf{x}}_i = \mathbf{x}_i - \mathbf{P}_p \mathbf{b}_i. \quad (4.7)$$

In case the user wants to correct a shape to a posture that differs from the average posture, it suffices to calculate the PC weights \mathbf{b}^* of that specific posture and subsequently calculate the posture corrected shape $\check{\mathbf{x}}$ as follows:

$$\check{\mathbf{x}} = \mathbf{x}_i - \mathbf{P}_p (\mathbf{b}_i - \mathbf{b}^*). \quad (4.8)$$

4.3 Evaluation

To validate the algorithm, we used scans from the Dutch CAESAR database [Robinette et al., 1999]. This is an extensive database that contains 3D scans, measurements and other meta-data of over 1000 people in standing pose. All subjects were scanned using the Vitronic Vitus Pro laser scanner [Vitronic, 1995] with a resolution of $2mm \times 2mm \times 2mm$ and a point density of 300 points/cm³s.

In the following subsections, an SSM in standing pose is built and the different steps to build a posture-normalized SSM are illustrated. The compactness of the non-normalized model is compared to the compactness of the normalized model and an optimal set of features for posture normalization was calculated.

4.3.1 Statistical Shape Model

An SSM was built from 700 subjects (350 men, 350 women) in standing pose from the CAESAR database [Robinette et al., 1999]. The 3D scans were registered using the same template surface mesh, a digitally modeled body consisting of 100k [Valette et al., 2008] uniformly distributed vertices. No posture changes were made to these meshes yet.

In Figure 4.2, the first three PC modes of the SSM built from the original shapes are shown. Influence of posture is visible in the third mode.

4.3.2 Posture-normalized Shape Model

In Figure 4.3, two examples of identity removal are shown. The resulting shapes look more similar than the original shapes. The features that were used for identity removal are: gender, acromial height sitting, ankle circumference, spine-to-shoulder, spine-to-elbow, arm length (spine to wrist), arm length (shoulder to wrist), arm length (shoulder to elbow), armscye circumference (scye circumference over acromion), bizygomatic breadth, chest circumference, bust/chest circumference under bust, buttock-knee length, chest girth (chest circumference at scye), crotch height, elbow height sitting, eye height sitting, face length, foot length, hand circumference, hand length, head breadth, head circumference, head length, hip breadth sitting, hip circumference maximum, hip circ max height, knee height, neck base circumference, shoulder breadth, sitting height, stature, subscapular skinfold, thigh circumference, thigh circumference max sitting, thumb tip reach, TTR 1, TTR 2, TTR 3, triceps skinfold, crotch length, vertical trunk circumference, waist circumference preferred, waist front length, waist height preferred, weight.

The posture model is shown in Figure 4.4. It was cut off at 12 shape modes to reduce shape related variations and remove noise from higher modes. This number was empirically determined by manually inspecting the shape modes. Then, the posture of every input shape of the original SSM was corrected. These shapes served as input to build a new, posture normalized, SSM. The first three shape modes of this posture normalized SSM are shown in Figure 4.5.

4.3.3 Posture Normalization Case

Six instances of the same shape with slightly different postures were artificially generated by rotating skeleton parts and applying linear blend skinning [Baran and Popović, 2007] on the shape. Then, the posture of every modified shape was

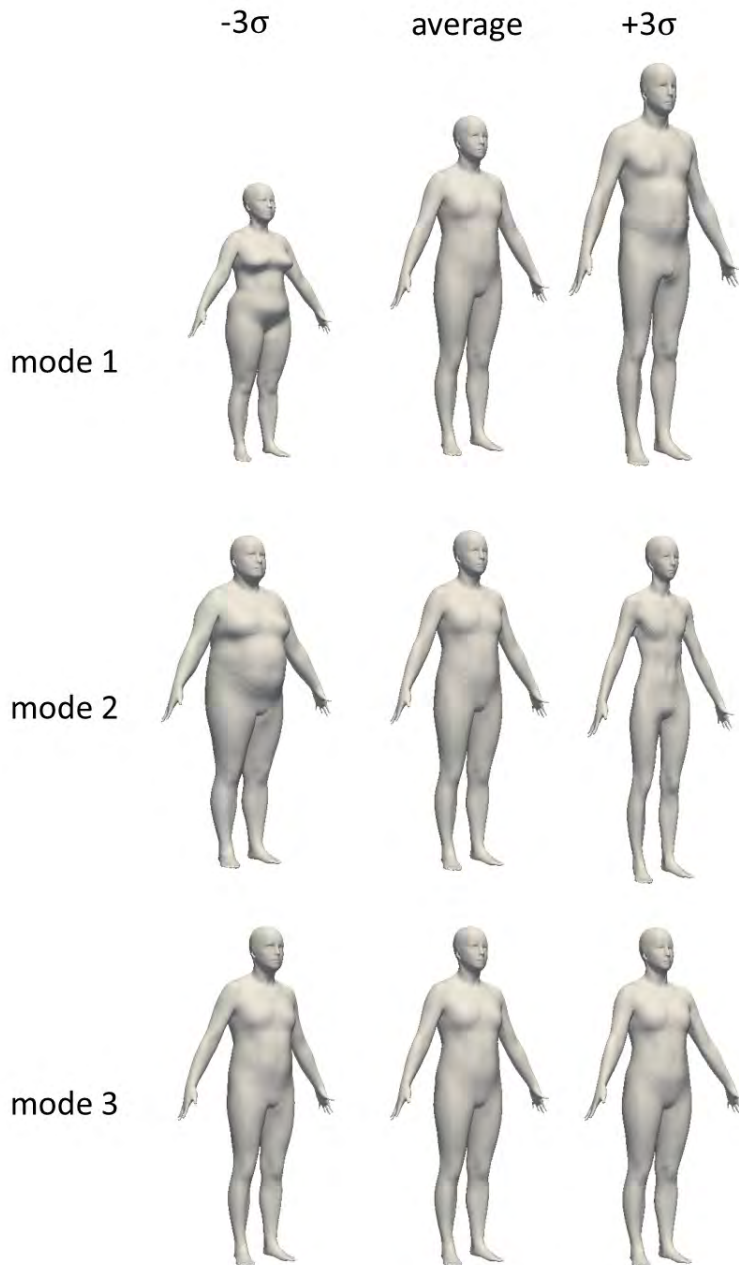


Figure 4.2: The first three eigenmodes of the non-normalized SSM, built from the original shapes. A posture variation is clearly noticeable in the third mode, where the position of the arms and shoulders differs.

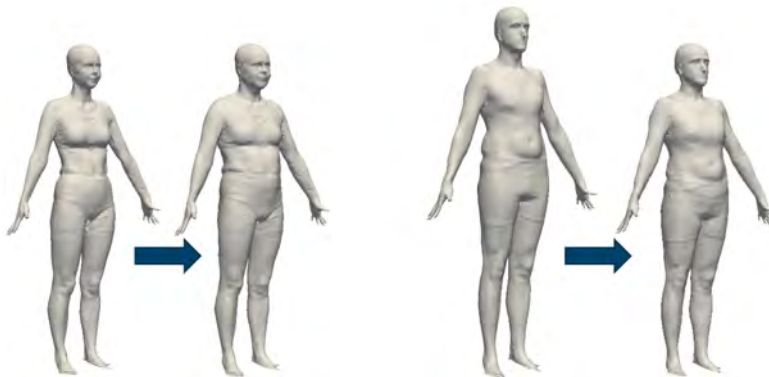


Figure 4.3: Two examples of identity removal.

normalized. The result of the posture deformation and posture normalization is shown in Figure 4.6. The average distance between the posture normalized shapes was $(2.91 \pm 0.99)mm$. Normalizing the posture of a shape took around 10s on a computer with an Intel® Core™ i7-5960X CP @ 3.00GHz processor and 32 GB memory.

4.3.4 Model Performance - Compactness

Compactness is a widely used measure for quantifying the correspondence quality of an SSM [Davies et al., 2002; Su, 2011]. A compact SSM is a model that has as little variance as possible and requires as few parameters as possible to define an instance. This suggests that the important information is captured in a plot of cumulative variance. Therefore calculation time decreases significantly when using the SSM for shape prediction from parameters, for example [Danckaers et al., 2015]. The compactness $C(m)$ is expressed as the sum of variances of the SSM using m shape modes,

$$C(m) = \sum_{i=1}^m \lambda_i, \quad (4.9)$$

where λ_i is the variance in mode i .

Figure 4.7 shows the compactness as a function of the number of shape modes. The normalized SSM is more compact than the non-normalized SSM. For example, to describe more than 90% of the shape variation inside the population, the non-normalized SSM requires seven shape modes, while only two shape modes were sufficient for the normalized SSM. Using only one shape mode, the normalized SSM is 16% more compact than the non-normalized SSM. For five shape modes, an improvement of 23% was observed, and an improvement of 25% using ten shape modes. The normalized SSM is substantially more compact than the non-normalized SSM and more of its variance is captured in the first modes, compared to the variance distribution of the non-normalized SSM.

4.3.5 Feature Selection

An SSM is a mathematical model that can be controlled by parameters. These parameters do not necessarily have a physical meaning. A more intuitive way of

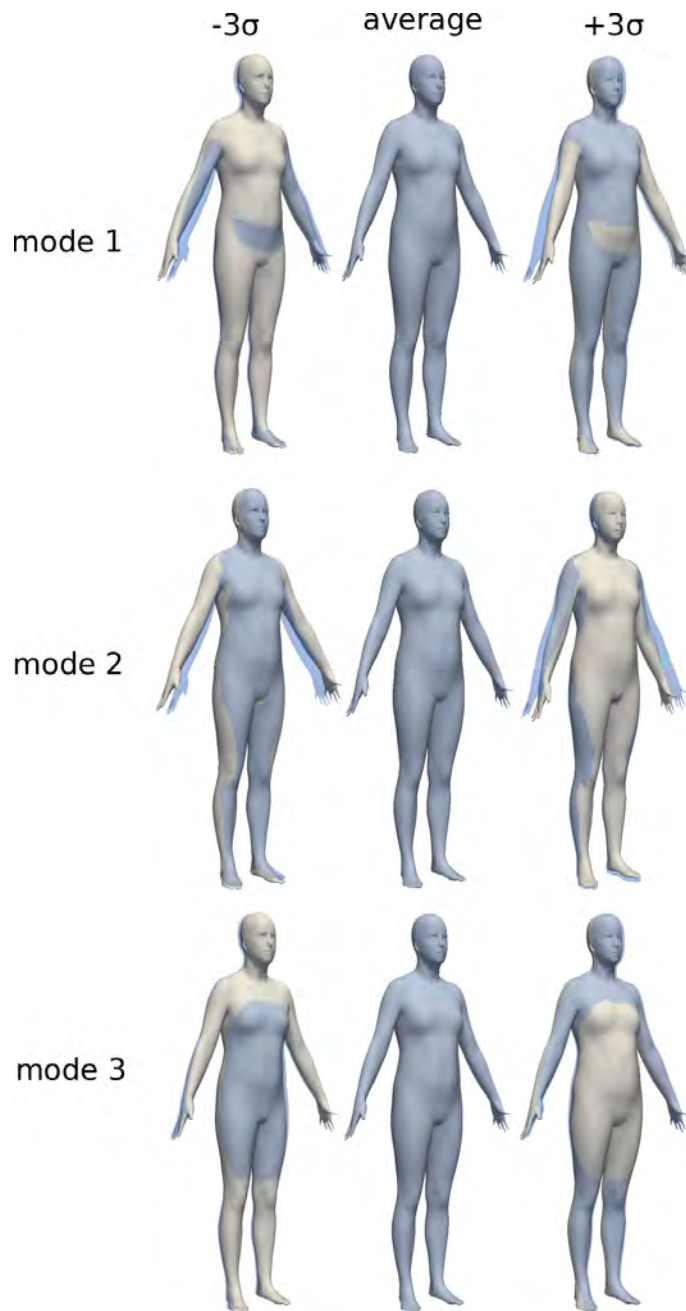


Figure 4.4: The first three eigenmodes of the posture model. Posture variation is mainly visible in the region of the arms and torso. For every shape, the average shape is overlaid in blue to show the difference in posture more clearly.

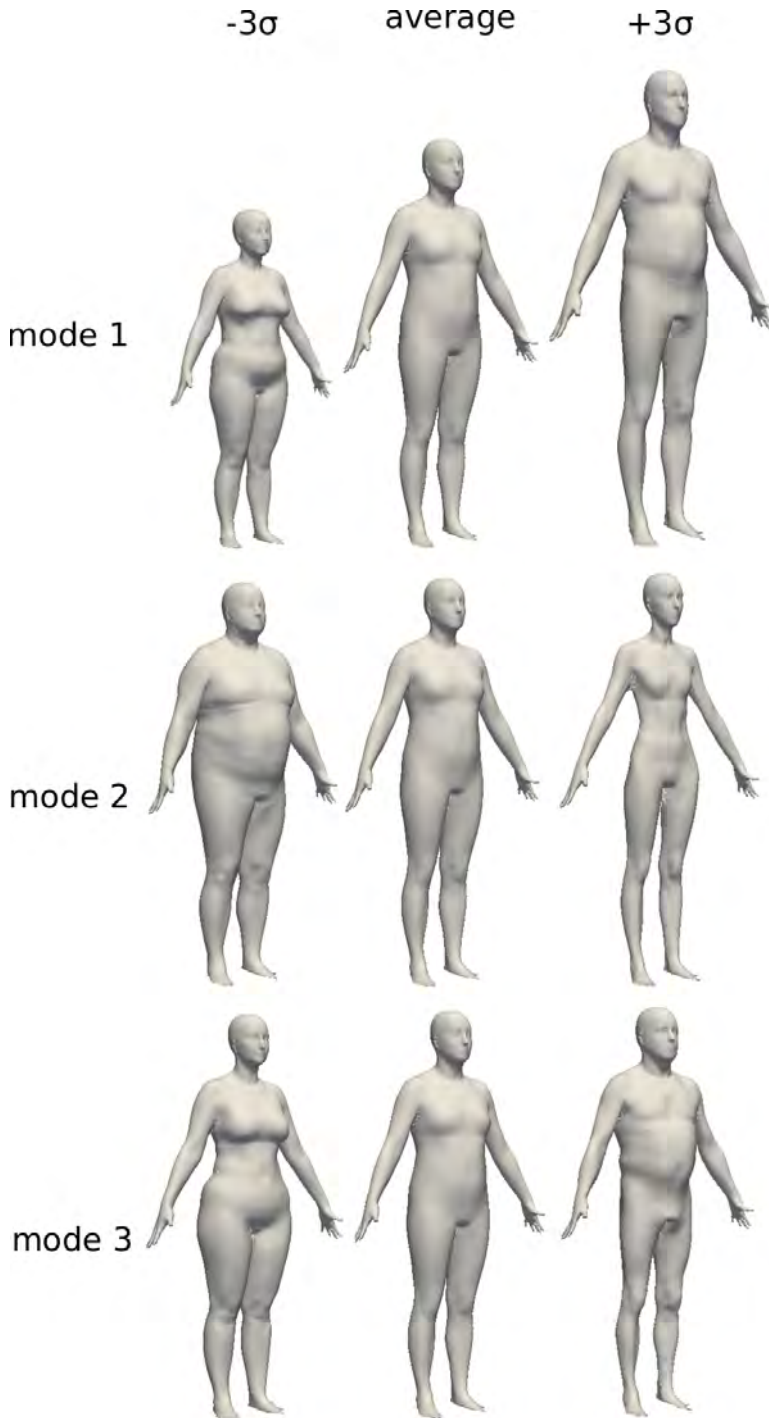


Figure 4.5: First three eigenmodes of the posture normalized SSM. The modes describe body shape variances better compared to the shape modes of the non-normalized SSM, shown in Figure 4.2. Note that the third mode of the normalized SSM describes mainly gender, while the third mode of the non-normalized SSM describes mainly the position of the arms.

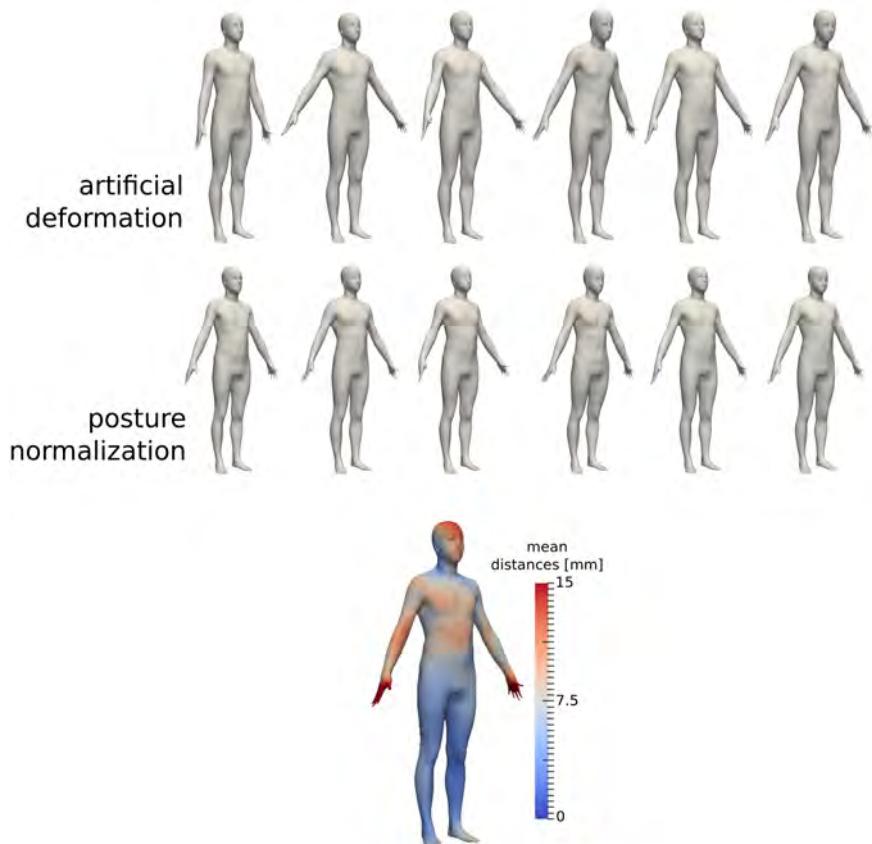
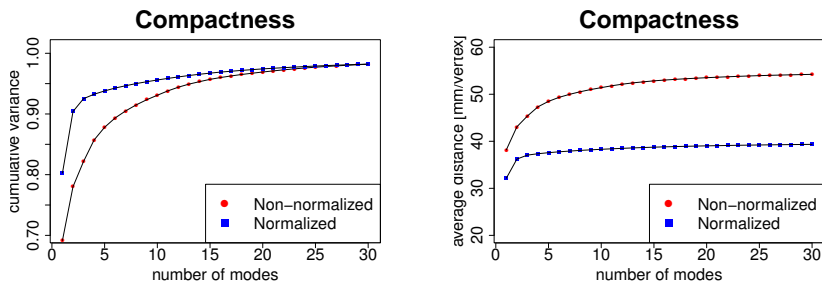


Figure 4.6: Posture normalization case. The same input shape was artificially deformed by rotating skeleton parts and applying LBS (upper row). The result of the posture normalization algorithm is shown in the lower row. The average distance between the posture normalized shapes and the original (non-modified) shape is shown below in $mm/vertex$, mapped on the ground truth.



(a) The average deviation from the mean shape of a shape described by a specific number of shape modes is shown.

(b) The average deviation from the mean shape of a shape described by a specific number of shape modes is shown in mm/vertex.

Figure 4.7: Compactness graphs, with only the first 30 shape modes plotted.

adjusting a body shape, is linking those parameters to physical features, such as height, weight, gender,... so the body shape is adaptable by changing the feature values. It is important to know which features influence body shape to generate an accurate posture model. An optimal set of features to predict a body shape was selected by cross-validation. The importance of each feature for predicting a body shape was determined by simulating a body shape based on features and comparing this shape with the real shape. The CAESAR database contains a lot of meta-data that do not necessarily influence the body shape. In this chapter, we used all available data for posture normalization. Missing meta-data in the CAESAR database were estimated through imputation [Wold, 1973].

The test was applied to 20 non-normalized shapes (10 men and 10 women) for the 14 easiest to measure features, using only a balance and a tape measure: gender (G), age (A), arm length (AL), breast circumference (BC), chest circumference (CC), crotch height (CH), hip circumference (HC), knee height (KH), shoulder breadth (SB), sitting height (SH), stature (S), thigh circumference (TC), waist circumference (WC), and weight (W). For every test subject, the body shape was predicted from every possible combination of its features. The average distance per vertex from the predicted body shape to the true body shape is calculated. The results are shown in Table 4.1. From a set of five features on, there is little improvement noticeable.

The average distance is visualized for every set of features on the average body shape and visualized in Figure 4.8 and Figure 4.9. These results show that the largest errors occur on the region of the arms and the head. This is due to posture related differences in the dataset. This test was repeated with the posture normalized SSM. The results are shown in Table 4.2 and Figure 4.8 and Figure 4.9.

4.3.5.1 Posture Normalization with a Small Set of Features

From the complete set of features included in the CAESAR database a posture model was built. To validate the influence of the used number of features on posture normalization, the experiment was repeated for the best feature set using 5 features and the best feature set using 11 features, selected from the 14 easiest to measure features. The posture models are shown in Figure 4.10. The posture normalized

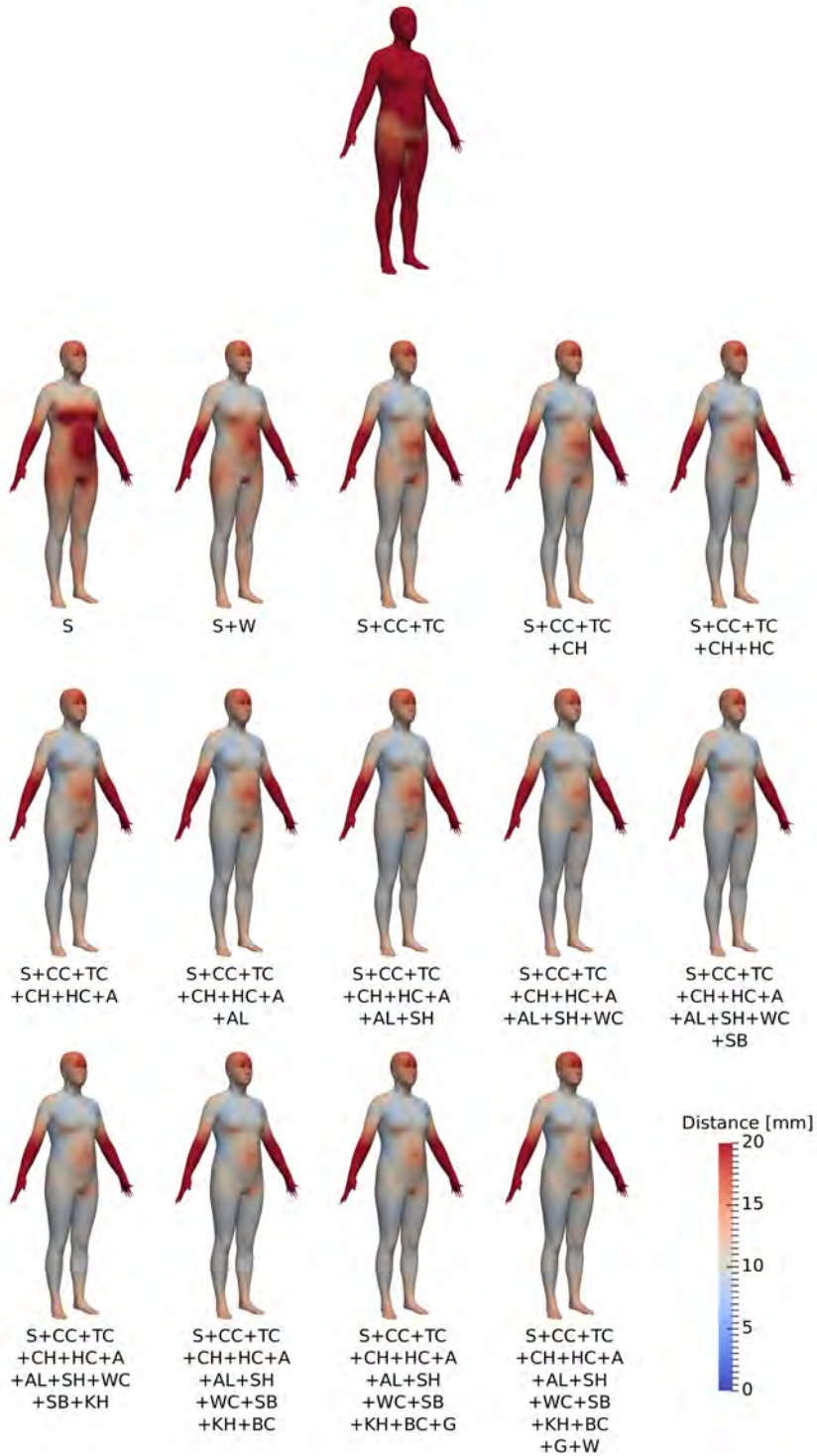


Figure 4.8: Regular non-normalized SSM, in mm/vertex. The largest errors appear in the regions of the arms and the head, due to posture differences. From five features on, little improvement in shape prediction is noticeable.

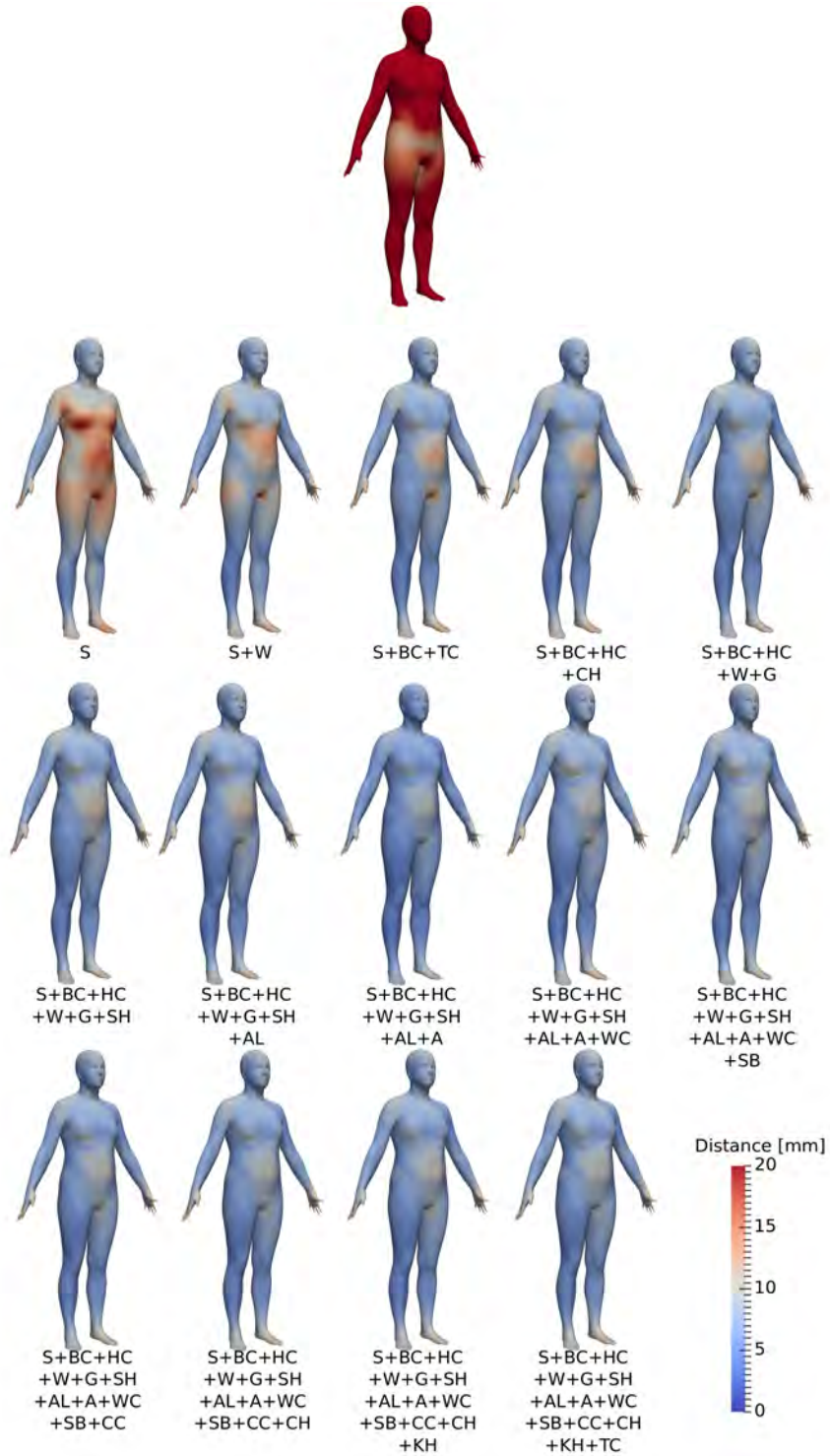


Figure 4.9: Posture normalized SSM, in mm/vertex. The largest errors appear in the stomach region. The previously noticeable errors in the regions of the arms and the heads are strongly reduced. From five features on, little improvement in shape prediction is noticeable.

Table 4.1: Average distance from the predicted body shape to the true shape using the non-normalized SSM, in mm/vertex. Only the two best results per number of features is shown. The test was applied for the 14 most relevant features: gender (G), age (A), arm length (AL), breast circumference (BC), chest circumference (CC), crotch height (CH), hip circumference (HC), knee height (KH), shoulder breadth (SB), sitting height (SH), stature (S), thigh circumference (TC), waist circumference (WC), and weight (W). The best set of features is marked in bold. Note that the last feature of the second best combination using n features is the last feature of the best combination using $n + 1$ features.

	Features	Average distance [mm]
0		31.17 ± 18.01
1	S	15.44 ± 3.27
	SH	18.22 ± 3.78
2	S + W	13.99 ± 2.92
	S + CC	14.04 ± 3.00
3	S + BC + TC	13.14 ± 2.80
	S + BC + HC	13.22 ± 2.73
4	S + BC + TC + CH	13.01 ± 2.81
	S + BC + TC + HC	13.01 ± 2.70
5	S + BC + TC + CH + HC	12.86 ± 2.69
	S + BC + TC + CH + A	12.90 ± 2.73
6	S + BC + TC + CH + HC + A	12.75 ± 2.58
	S + BC + TC + CH + HC + AL	12.78 ± 2.57
7	S + BC + TC + CH + HC + A + AL	12.68 ± 2.46
	S + BC + TC + CH + HC + A + SB	12.69 ± 2.52
8	S + BC + TC + CH + HC + A + AL + SH	12.65 ± 2.45
	S + BC + TC + CH + HC + A + AL + WC	12.65 ± 2.47
9	S + BC + TC + CH + HC + A + AL + SH + WC	12.62 ± 2.44
	S + BC + TC + CH + HC + A + AL + SH + SB	12.63 ± 2.42
10	S + BC + TC + CH + HC + A + AL + SH + WC + SB	12.60 ± 2.41
	S + BC + TC + CH + HC + A + AL + SH + WC + KH	12.61 ± 2.56
11	S + BC + TC + CH + HC + A + AL + SH + WC + SB + KH	12.59 ± 2.53
	S + BC + TC + CH + HC + A + AL + SH + WC + SB + CC	12.62 ± 2.46
12	S + BC + TC + CH + HC + A + AL + SH + WC + SB + KH + CC	12.62 ± 2.55
	S + BC + TC + CH + HC + A + AL + SH + WC + KH + CC + G	12.65 ± 2.54
13	S + BC + TC + CH + HC + A + AL + SH + WC + SB + KH + CC + G	12.66 ± 2.54
	S + BC + TC + CH + HC + A + AL + SH + WC + SB + KH + CC + W	12.79 ± 2.55
14	S + BC + TC + CH + HC + A + AL + SH + WC + SB + KH + CC + G + W	12.83 ± 2.55

Table 4.2: Average distance from the predicted body shape to the true shape using the posture-normalized SSM, in mm/vertex. Only the best result per number of features are shown. The most important features to predict a person’s body shape. The test was applied for the 14 most relevant features: gender (G), age (A), arm length (AL), breast circumference (BC), chest circumference (CC), crotch height (CH), hip circumference (HC), knee height (KH), shoulder breadth (SB), sitting height (SH), stature (S), thigh circumference (TC), waist circumference (WC), and weight (W). The best set of features is marked in bold.

	Features	Average distance [mm]
0		26.67 ± 20.04
1	S KH	10.09 ± 2.84 14.07 ± 5.81
2	S + W S + BC	8.08 ± 1.54 8.16 ± 1.62
3	S + BC + HC S + W + HC	7.11 ± 1.20 7.14 ± 1.42
4	S + BC + HC + CH S + BC + HC + G	6.94 ± 1.14 6.94 ± 1.30
5	S + BC + HC + W + G S + BC + HC + SH + G	6.84 ± 1.30 6.85 ± 1.35
6	S + BC + HC + W + CC + SH S + BC + HC + W + G + SH	6.75 ± 1.32 6.75 ± 1.35
7	S + BC + HC + W + CC + SH + AL S + BC + HC + W + G + SH + AL	6.67 ± 1.31 6.67 ± 1.35
8	S + BC + HC + W + G + SH + AL + A S + BC + HC + W + CC + SH + AL + A	6.63 ± 1.30 6.63 ± 1.34
9	S + CC + HC + W + G + SH + AL + A + WC S + BC + HC + W + G + SH + AL + A + WC	6.61 ± 1.30 6.61 ± 1.35
10	S + BC + HC + W + G + SH + AL + A + WC + SB S + BC + HC + W + G + SH + AL + A + WC + CC	6.60 ± 1.27 6.60 ± 1.31
11	S + BC + HC + W + G + SH + AL + A + WC + SB + CC S + BC + HC + W + G + SH + AL + A + WC + SB + CH	6.59 ± 1.28 6.60 ± 1.23
12	S + BC + HC + W + G + SH + AL + A + WC + SB + CC + CH S + BC + HC + W + G + SH + AL + A + WC + SB + CC + TC	6.59 ± 1.24 6.62 ± 1.29
13	S + BC + HC + W + G + SH + AL + A + WC + CH + TC S + BC + HC + W + G + SH + AL + A + WC + CC + CH + KH	6.63 ± 1.26 6.65 ± 1.26
14	S + BC + HC + W + G + SH + AL + A + WC + SB + CC + CH + KH + TC	6.69 ± 1.28

models are shown in Figure 4.11

The first three modes are similar for every set of features. However, in the seventh shape mode, a difference in shape is noticeable. This has influence on posture normalization, as those shape differences will be filtered out.

4.4 Discussion

The main innovation presented in this chapter is a methodology to generate posture invariant statistical shape models. Consequently, shape variation of a human 3D body scan population can be analyzed in a more precise way. The shapes were described in a detailed, realistic way and focus mainly on shape variation, compared to the current SSMs where posture variation is incorrectly regarded as shape variation. The algorithm is applicable to any body shape of any dataset, standing in A-pose. No prior knowledge of shape dimensions is required when a posture model is already available. With a posture model available, it took 10s to normalize a body shape.

Advantages of a posture normalized model is that the shape remains consistent for all generated body instances using the SSM. For product designers that use the model to generate design mannequins, it is preferred to keep a constant posture for different body shapes. Shape and posture are treated as two different things when designing, so it is a benefit to be able to regard them as two separate things when creating a virtual mannequin as well. By separating posture from body shape, a designer can start from the same preconditions for designing for different sizes. Hence, a designer can link a virtual design to the SSM so the design changes along with the body shape. Furthermore, the shape modes are easier to interpret and can be linked to specific features, which in turn may simplify shape prediction. Additionally, with a posture normalized SSM, clustering will not be polluted by posture, so it is less likely that shapes with similar posture will unintendedly be regarded as similar shapes.

The normalized SSM is more compact than the non-normalized SSM. For example, to describe more than 90% of the shape variation inside the population, the non-normalized SSM requires seven shape modes, while only two shape modes are sufficient for the normalized SSM. Using only one shape mode, the normalized SSM is 16% more compact than the non-normalized SSM. For five shape modes, an improvement of 23% was observed, and an improvement of 25% using ten shape modes. A compact model has many advantages. It will decrease the need for storage space. Indeed, if almost all of the variance is captured by K modes with $K \ll N$, only K rows of matrix $B \in \mathbb{R}^{(N-1) \times N}$ need to be stored. Another advantage of a compact model, is that less computation time is consumed when using the model for applications such as shape prediction. The complexity of calculating mapping matrix $\mathbf{M} = \mathbf{B}\mathbf{F}^+$, with principal component (PC) weights matrix $\mathbf{B} \in \mathbb{R}^{(N-1) \times N}$ and feature matrix $\mathbf{F} \in \mathbb{R}^{(F+1) \times N}$ is $O((N-1)N(F+1))$. When the model is compact, it means that only the first shape modes, or the first elements of matrix \mathbf{B} are needed to describe a specific percentage of the shape variance, so we can delete the last rows such that $\mathbf{B} \in \mathbb{R}^{K \times N}$, with $K \ll N$. In that way, the complexity of the multiplication is reduced from $O((N-1)N(F+1))$ to $O(KN(F+1))$ with $K \ll N$. Also, a more compact model will lead to less energy consumption. The energy efficiency is directly linked to the relative profit obtained by a reduced computation time. Furthermore, a compact model will decrease chances for overfitting. The more shape modes present in the shape model, the worse the precision of the estimated shape model parameters. Hardly any difference is noticeable between the posture normalized SSM using all

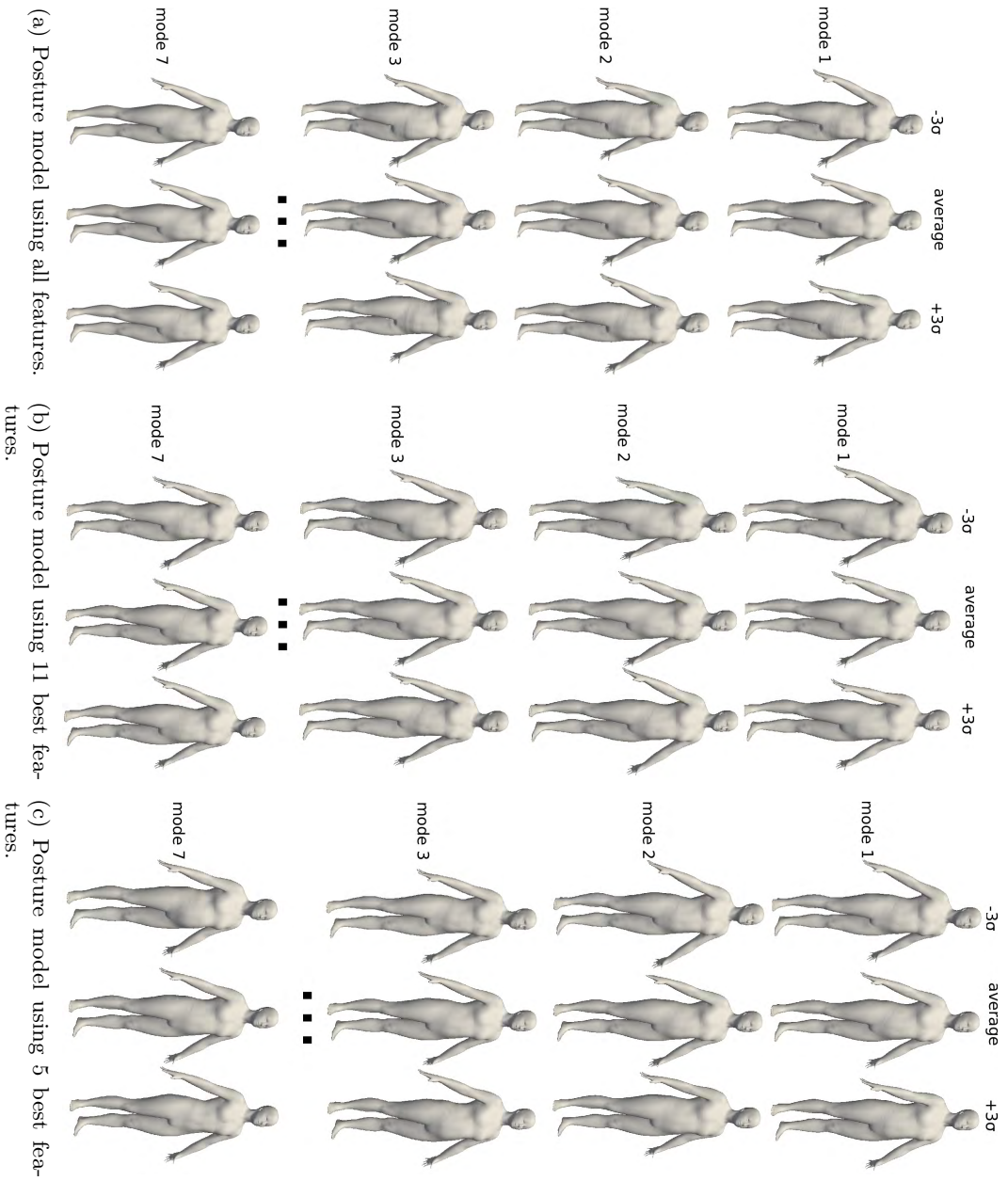
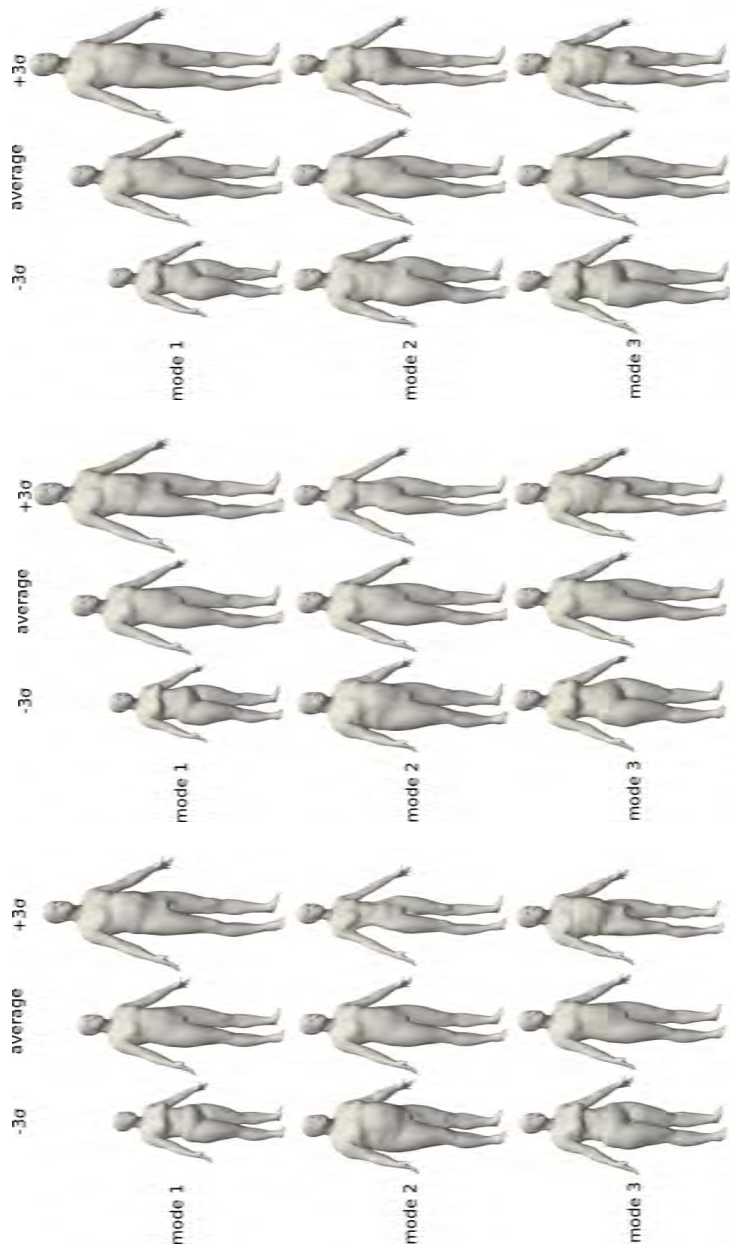


Figure 4.10: Posture model with varying number of features.



(a) Posture normalized SSM using all features. (b) Posture normalized SSM using 11 best features. (c) Posture normalized SSM using 5 best features.

Figure 4.11: Posture normalization with varying number of features.

features and the posture normalized SSM using the 11 best features. These features are: stature, breast circumference, thigh circumference, crotch height, hip circumference, age, arm length, sitting height, waist circumference, shoulder breadth, and knee height. Therefore, the approach is reproducible with another dataset and some simple meta-data. It may be noted that stature is the most important feature to predict a person's body shape. Using only 5 features, a vast difference in shape can be observed in the second shape mode. This is because too many shape differences were incorporated in the posture model and thus filtered out in the posture normalized SSM.

A method for simulating a body shape from simple measurements is a valuable tool for product developers that design near-body products. With our technique, a virtual 3D mannequin can be created. Such tools (Digital Human Models - DHM) are already widespread, but are often an oversimplified representation of the population, based on 1D measurements, so 3D shape variation is not incorporated [Moes, 2010; Blanchonette, 2010; Van Der Meulen and Seidl, 2007]. The body shape is modified by scaling the body parts. Therefore, these DHMs are not as realistic as the models that we can create using a posture normalized SSM. Because we use a data-driven technique, the whole variation within the complete shape population is captured and simulated shapes are a realistic representation of a body with those measurements. Our tests have shown that we could predict a body shape using 11 features, using the non-normalized SSM, with an error of $(12.59 \pm 2.53)mm$. Furthermore, starting from the posture normalized SSM, we could reduce this error to $(6.59 \pm 1.28)mm$. The method is also useful to visualize feature percentiles. In Figure 4.12, we show some body shapes simulated from one given feature.

For validation of our proposed framework, we used the existing CAESAR database [Robinette et al., 1999]. The subjects got strict posture instructions before scanning. Their feet had to be placed on foot outlines positioned $10cm$ apart at the inside of the heel and were positioned on the scanner platform at a 30° angle. The researchers used a $20cm$ long dowel to adjust the subject's arm position so the hands were $20cm$ away from the most lateral point of the hip/thigh area. The arms and wrists were kept straight and the palms of the hands faced the body, with fingers spread. They were instructed to stand straight and look straight ahead. Because of these instructions, little posture variances, especially in the legs area, was observed. If the subjects from the CAESAR dataset would have been scanned with less strict instructions, more posture variation (e.g. angle between the legs, angle between the arms and the body, bending of the knees) would have been observed, leading to a posture model that is able to filter out more posture variation. Another option would be to generate a dataset with explicitly different postures, to assure a more robust normalization algorithm for large posture variations. More research is needed to see how a posture model built from a different dataset with more posture variation could cope with larger posture differences.

Note that in this manuscript, all posture deviations were filtered out. This means that posture deviations related to natural posture are filtered out as well. In some cases, the influence of those posture deviations on the shape, is valuable information. A possible approach to keep these specific variations, is to look into detail to the shape modes of the posture model, and manually removing modes that have to do with natural posture variation. In other words, keeping the mode where the arms are bent and flexed, while removing the mode where the spine goes from kyphosis to lordosis, as this is related to natural posture.

One limitation of the described framework is that it uses a linear methodology. Therefore, it can not handle large rotational posture differences, such as torso flexion and rotation of the elbow. Our algorithm is able to correct for rotational deformations (to a certain accuracy) using multiple shape modes, as shown in Fig 4.6. Further investigation is needed to be able to cope with this type of posture differences.

A logical next step in this work, is adding motion to the statistical shape model. In that way, the shape model would be usable for reachability tests (e.g. when designing a vehicle, to test whether the driver is able to reach everything) or designing near-body products (e.g. to test whether the clothes will fit the user, and to validate this for a whole range of motions).

The software for the described algorithms was written in Python and based on the Visualization ToolKit (VTK) libraries [Schroeder et al., 1997] and the Scientific Python (SciPy) libraries [Oliphant, 2007]. VTK is an open-source software systems for 3D computer graphics, image processing, and visualization. SciPy is a scientific computing library.

4.5 Conclusion

In this work, we proposed a technique to perform statistical shape analysis in a posture-invariant way. It allows us to study the shape variations in a database of human body shapes in slightly varying postures. The posture model can be used to normalize any shape that is brought into correspondence with this model in a fast and precise way.

The results have shown that statistical shape analysis of a posture normalized population results in more shape related variations than performing the same analysis on a non-normalized population. The normalized SSM is a more compact representation of the population, compared to the non-normalized shape SSM. Hence, less shape modes are needed to describe a certain percentage of the population.

Our SSM is a valuable tool for product designers for creating more realistic, virtual mannequins, which can be used to improve the ergonomics of their products. It is also a first step towards posture invariant statistical shape analysis of body shapes in varying poses, e.g. for predicting the body shape in seated pose from a body shape in standing pose. Therefore, one scan is sufficient for product developers to design products that require simulating the body shape in different poses.

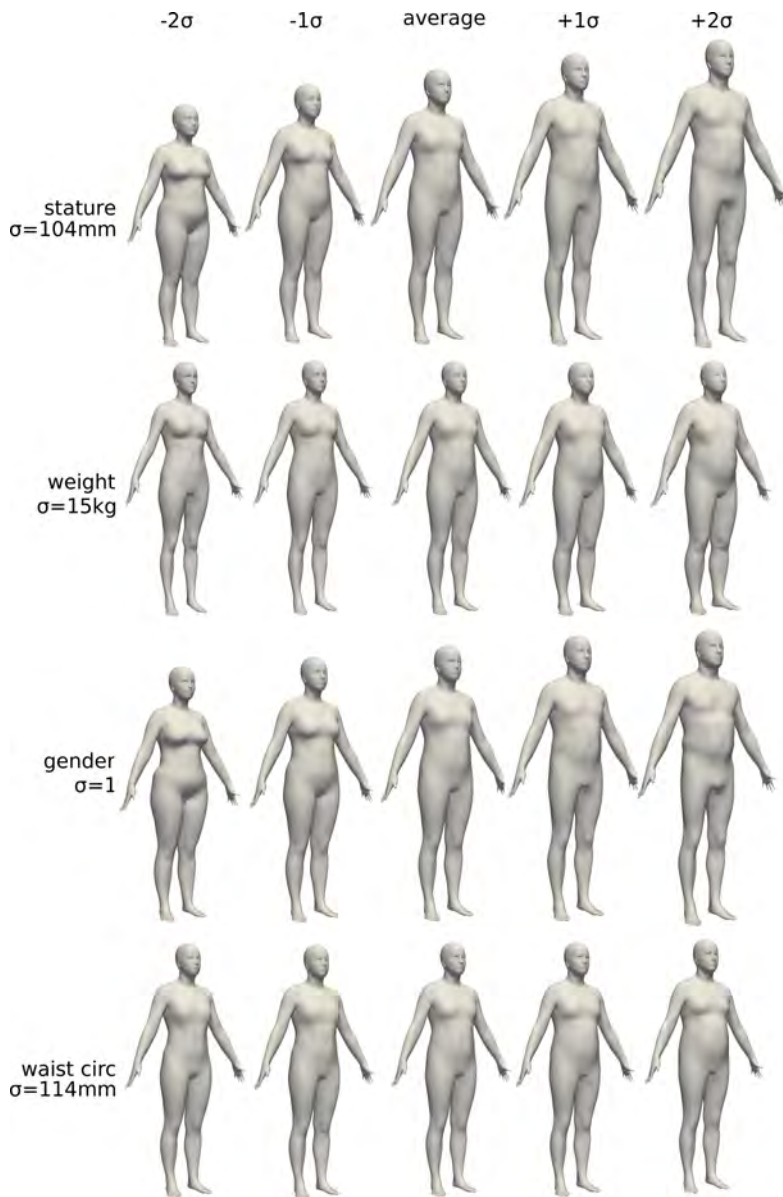


Figure 4.12: The most plausible body shapes from one given feature. The standard deviation σ of the feature is calculated and the body shape is simulated for -2σ , -1σ , the average body shape μ , $+1\sigma$ and $+2\sigma$.

This work was previously published as:

Danckaers, F., Scataglini, S., Haelterman, R., Van Tiggelen, D., Huysmans, T., and Sijbers, J. (2019). Automatic generation of statistical shape models in motion. In Advances in Human Factors in Simulation and Modeling, pages 170-178. Springer, Cham.

5

Automatic Generation of Statistical Shape Models in Motion

Contents

Abstract	64
5.1 Introduction	65
5.2 Methods	65
5.2.1 Building a statistical shape model	65
5.2.2 Skeleton generation	66
5.2.3 Modification of movement file	67
5.3 Experiments and Results	68
5.3.1 Shape prediction and skeleton generation	68
5.3.2 Adding movement	68
5.4 Conclusion	70

Abstract

Statistical body shape modeling (SBSM) is a well-known technique to map out the variability of body shapes and is commonly used in 3D anthropometric analyses. In this chapter, a new approach to integrate movement acquired by a motion capture system with a body shape is proposed. This was done by selecting landmarks on a body shape model, and predicting a body shape based on features. Then, a virtual skeleton was generated relative to those landmarks. This skeleton was parented to a body shape, allowing to modify its pose and to add pre-recorded motion to different body shapes in a realistic way.

5.1 Introduction

Statistical body shape modeling (SBSM) is a well-known technique to map out the variability of body shapes and is commonly used in 3D anthropometric analyses. Statistical body shape models (SBSMs) can describe the variability of body shapes for a population of individuals. By adapting the parameters of the SBSM, a new realistic shape can be formed. Product developers may exploit SBSMs to design virtual design mannequins and explore the body shapes belonging to a specific percentile of a target group, allowing to visualize extreme shapes. Moreover, an SBSM allows to simulate a specific 3D body shape [?], which is useful for customization.

Nowadays, inertial motion tracking sensors (IMU) allow capturing human motion and acquiring the kinematic of the subject during a physical task. This information is translated as a skeletal animation as a Biovision Hierarchy (BVH) character animation file. In this study, we acquired the subject's motions with a real-time inertial motion tracking system (Yost Labs 3-Space Sensor).

This is especially relevant for people who have to perform physically demanding tasks in non-ideal circumstances. Their gear must have an optimal fit, to reduce the impact on their body. For example, reachability tests in vehicles or testing the freedom of movement when wearing their equipment or heavy backpacks [??].

Unfortunately, to date, there is no framework available to generate body shapes in motion where both body shape as articulation is adaptable. Another possibility is to add motion to a specific body scan. We propose a new approach to integrate the movement acquired by an inertial motion capture system with the statistical body shape. This allows product developers to validate their designs for multiple poses and movements.

5.2 Methods

In this section, a framework to create moving SBSMs is described. First, a SBSM is built from a population of 3D human body shapes [?]. Next, the method to generate a body shape based on features is explained [?]. Finally, modification of a motion file and adding motion to a specific body shape is discussed.

5.2.1 Building a statistical shape model

First, a reference surface, a digitally modeled body shape [?] with n uniformly distributed vertices, is registered in a marker-less way to N input surfaces to obtain a homologous point-to-point correspondence. All input surfaces were corrected for posture, in a way that every shape was standing in the average posture, determined from a population of 700 scans from the CAESAR database [?]. Then, a statistical shape model is built using principal component analysis of the population of N posture normalized corresponded surfaces. In an SBSM, the mean shape $\bar{\mathbf{x}} \in \mathbb{R}^{3n}$ and the main shape modes, or the principal component (PC) modes of the SBSM, $\mathbf{P} \in \mathbb{R}^{3n \times (N-1)}$ are incorporated. This means that a new shape $\mathbf{y} \in \mathbb{R}^{3n}$ can be formed by a linear combination of the PCs:

$$\mathbf{y} = \bar{\mathbf{x}} + \mathbf{P}\mathbf{b} \quad (5.1)$$

with $\mathbf{b} \in \mathbb{R}^{N-1}$ the vector containing the SBSM parameters. A specific feature of an person's shape, such as height, can be adapted by adding a linear combination

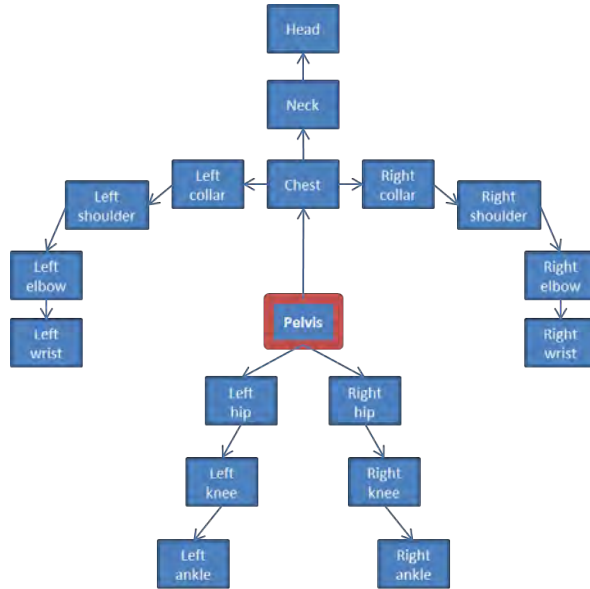


Figure 5.1: Schematic visualization of the skeleton.

of principal components to the person’s shape vector. The weights for this linear combination are computed via multiple linear regression of the PC weights on the body features (such as height, weight, gender, . . .) for the population of individuals. Every feature is defined by a scalar value. A mapping matrix describing the relationship between the biometric features of every input shape and the principal component weights of every input shape is calculated using multivariate regression, by

$$\mathbf{M} = \mathbf{BF}^+ \quad (5.2)$$

with \mathbf{F}^+ the pseudoinverse of \mathbf{F} . By multiplying \mathbf{M} with a given feature vector \mathbf{f} , new principal component weights $\mathbf{b} \in \mathbb{R}^{N-1}$ can be generated:

$$\mathbf{b} = \mathbf{Mf} \quad (5.3)$$

From these principal component weights, a new body shape can be built.

5.2.2 Skeleton generation

The BVH file format is a way to provide skeleton hierarchy information in addition to the motion data. The skeleton is typically in T-pose. In such a BVH file, the skeleton is represented as a tree structure set of 18 joints, relative to each other. This is shown in Figure ???. In most cases, the pelvis is the root of the skeleton. Every other joint is defined by an offset from the previous joint.

Forty-one landmarks available in the CAESAR database, such as olecranon, humeral epycondyle lateral, substernale, etc are selected on the average body shape. Because of the correspondences, every vertex will remain at anatomically the same location, independent of shape. A new skeleton of a Biovision Hierarchy (BVH) character animation file [?] was generated by calculating the optimal joint locations relative to these landmarks. Next, the skeleton is parented to the body shape by calculating

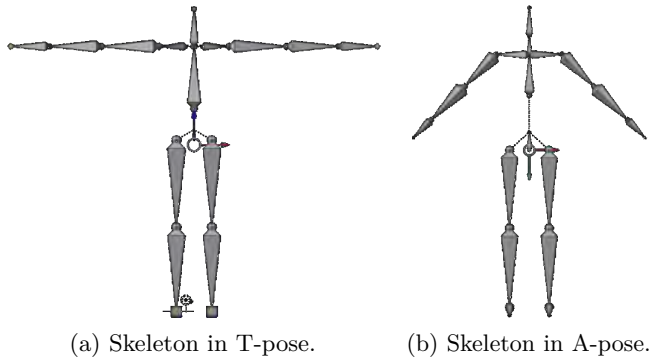


Figure 5.2: The skeleton in rest pose.

skinning weights [?]. As a result, the pose of that body shape can be adapted. This means it can be adapted manually or a pre-defined movement can be executed.

5.2.3 Modification of movement file

Motion is defined per frame, by a rotation offset per joint from the original skeleton. The body shapes available in the CAESAR database are standing in A-pose, as shown in Figure ???. Therefore, the BVH files have to be adapted from T-pose to A-pose, as shown in Figure 2. It is not sufficient to only convert the rest pose, as the motion is defined as rotation of the joints in rest pose. To solve this problem, we wrote Python code that can be run in Blender [?]. This code allows one to change the rest pose to the current adapted pose in Blender and to copy the original joint position to the new skeleton per frame.

A skeleton $S \in \mathbb{R}^{3 \times j}$ is defined as a set of j joints $\mathbf{J} \in \mathbb{R}^3$, whereas every joint per frame contains a rotation matrix $R \in \mathbb{R}^{3 \times 3}$ from the rest pose to the pose of the current frame.

$$\mathbf{S} = [\mathbf{J}_1 \ \mathbf{J}_2 \ \mathbf{J}_3 \ \cdots \ \mathbf{J}_j] \quad (5.4)$$

The work flow is as follows: first, the original skeleton $S_0 \in \mathbb{R}^{3 \times j}$ is manually put in A-pose by rotating the joints, by a transformation \mathbf{T} , resulting in a transformed skeleton $\mathbf{S}_T \in \mathbb{R}^{3 \times j}$. The new pose is applied as rest pose of the skeleton:

$$\mathbf{S}_T = \mathbf{T} \times \mathbf{S}_0 \quad (5.5)$$

The following step is to update the actions per frame, as the movement is defined by rotation of the joints in rest pose. As a first step, the skeleton \mathbf{S}_T is translated in a way so the root joints, in this case the pelvis, are on the same location. The copied joints are rotated to match the orientation of the target joints. This is done by inverting the rest pose matrix and multiplying this with the rotation matrix of the current inverse of the rotation matrix of the parent joint and the rotation matrix of the parent joint in resting position. The resulting rotation matrix has to be applied to the specific frame of the skeleton in A-pose as resting pose:

$$\mathbf{R}'_T = \mathbf{R}_T^{-1} \times \mathit{parent}(\mathbf{R}_{t,rest}) \times \mathit{parent}(\mathbf{R}_T)^{-1} \times \mathbf{R}_0 \quad (5.6)$$

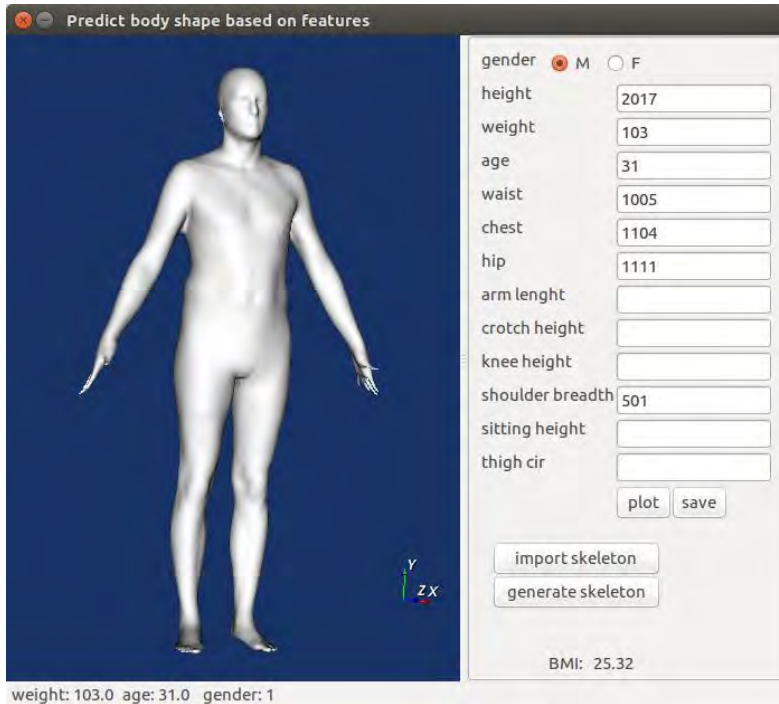


Figure 5.3: Screenshot of body shape prediction and skeleton generation tool. The most plausible body shape of a man with height $2.017m$, weight $103kg$, age 31 , waist $100.5cm$, chest $110.4cm$, and shoulder breadth $50.1cm$ is generated. The remaining values were unknown, so these values were not taken into account.

5.3 Experiments and Results

5.3.1 Shape prediction and skeleton generation

A user interface was designed in which the following values can be specified: height, weight, age, waist circumference, chest circumference, hip circumference, arm length, crotch height, knee height, shoulder breadth, sitting height, and thigh circumference. We acquired the movement of a walking person using an inertial motion tracking system. After the shape had been generated, a new skeleton with associated movement was calculated. A screenshot of our implemented tool is shown in Figure ???. This means that this feature will not be taken into account for shape prediction and the most plausible shape using the remaining values will be calculated.

5.3.2 Adding movement

The generated mesh and associated skeleton were imported in Blender, where the skeleton was parented to the mesh using automatic weights [?]. This approach resulted in a realistic body shape in motion, as can be seen in Figure ???.

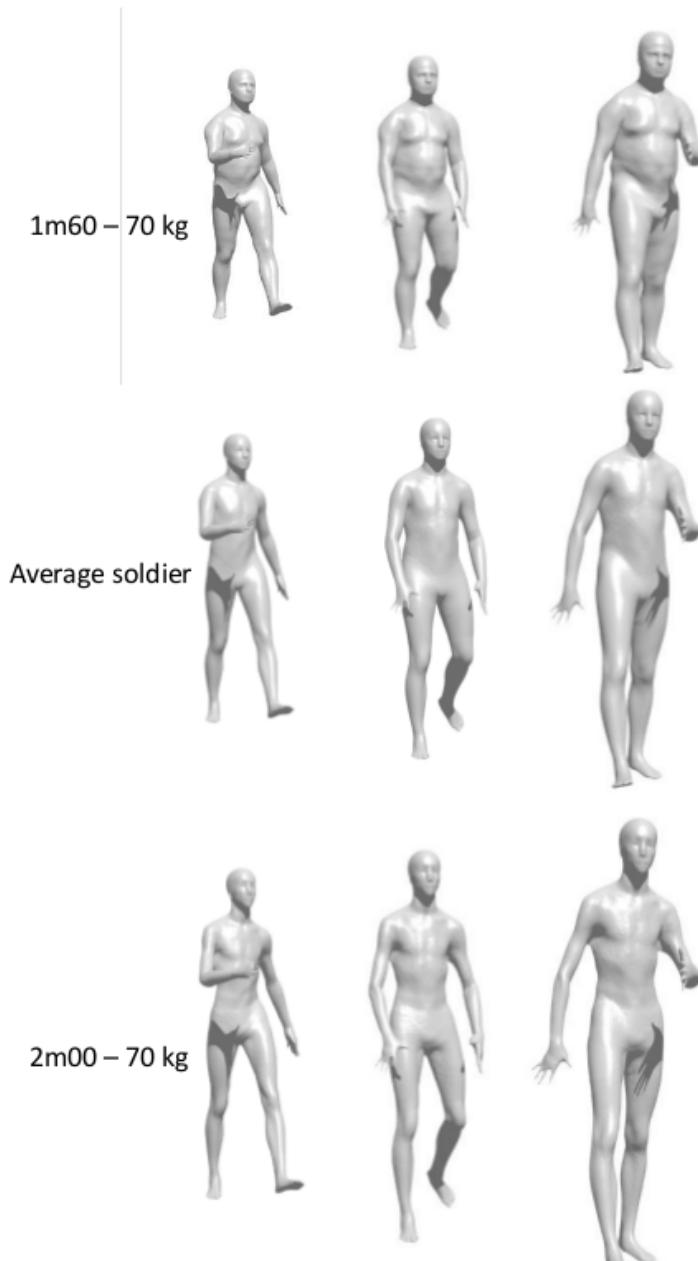


Figure 5.4: Examples of walking persons with different body shapes.

5.4 Conclusion

We proposed an automatic technique to rig a statistical body shape model, allowing to simulate movement on a whole range of body shapes. Results show that our framework leads to detailed, realistic body shapes, that are able to move. This is especially useful for accessibility testing, e.g. when designing a vehicle, where the driver has to be able to perform specific movements to operate it in a correct way, while space is limited, or when optimizing comfort in wearing gear. Furthermore, static pose is adaptable by manipulating the armature, which is useful for designing near body products that require the body to be in a pose that is difficult to scan.

Part III

Applications

This work was previously published as:

Danckaers, F., Huysmans, T., Van Dael, M., Verboven, P., Nicolai, B., and Sijbers, J. (2017). Building 3D Statistical Shape Models of Horticultural Products. Food and Bioprocess Technology, 10(11):2100–2112.

6

Building 3D Statistical Shape Models of Horticultural Products

Contents

Abstract	74
6.1 Introduction	75
6.2 Methods	76
6.2.1 Data Collection	76
6.2.2 Building a Statistical Shape Model	77
6.3 Results and Discussion	78
6.3.1 Surface Registration	78
6.3.2 Shape Model	80
6.3.3 Description with CAD primitives	80
6.3.4 Model Performance	80
6.3.5 Discussion	85
6.4 Conclusions	86

Abstract

A method to build a 3D statistical shape model of horticultural products is described. The framework consists of two parts. First, the surfaces of the horticultural products, which are extracted from X-ray CT scans, are registered to obtain meaningful correspondences between the surfaces. In the second part, a statistical shape model is built from these corresponded surfaces, which maps out the variability of the surfaces and allows to generate new, realistic surfaces. The proposed shape modeling method is applied to 30 Jonagold apples, 30 bell peppers, and 52 zucchini. The average geometric registration error between the original instance and the deformed reference instance is $0.015 \text{ mm} \pm 0.011 \text{ mm}$ for the apple dataset, $0.106 \text{ mm} \pm 0.026 \text{ mm}$ for the bell pepper dataset, and $0.027 \text{ mm} \pm 0.007 \text{ mm}$ for the Zucchini dataset. All shape models are shown to be an excellent representation of their specific population, as they are compact and able to generalize to an unseen sample of the population.

6.1 Introduction

Capturing the variability in geometry of vegetables and fruit is important in many aspects of food processing, such as object detection and shape prediction [?]. ? used digital camera images to detect fruit for automatically picking fruit using robots. Prominent shapes were detected by Canny edge detection and Hough transformation. With a statistical shape model, fruit could be detected from one single view, while simultaneously estimating the 3D shape. [?] predicted the firmness of apple fruit from multispectral scattering images. Light scattering profiles are influenced by the shape of the apple. With a statistical shape model, the shape of the apple could be estimated from limited views to reduce the shape influence, to improve the firmness prediction. ? used RGB-D images to detect fruit hanging on a tree. They combined color with the 3D surface normal features, 3D plane-reflective symmetry, and image plane highlights from elliptic surface points to provide shape-based detection of fruits in 3D space regardless of their color. Their method, however, assumes fruit to be symmetric.

In ?, a regression analysis was used to predict the final size of fruit based on the diameter at different growth stages. Statistical shape models could be used to incorporate a more complex description of the shape in the regression, likely improving the prediction results. Moreover, statistical shape models could be valuable to estimate the volume of a fruit from one single view [?], or to search for a correlation between the stages of growth [?]. A challenging problem is the estimation of the 3D shape to build high resolution dose maps for radiation treatment of heterogeneous food products [??], as it is important to determine the required irradiation dose. Statistical shape models could lead to a more accurate description of the 3D shape, which would in turn allow to better predict dose deposits. Geometry modeling of food is important for the food engineering domain [??]. Realistic 3D models of Conference pears have served to develop nondestructive methods for measuring fruit firmness [?]. Fruit storage designers may use fruit shape models to evaluate the effect of the shape of the fruit on airflow characteristics and thus cooling uniformity [?????], or to solve stacking problems [?].

Statistical shape models are widely used in medical imaging research in a very similar way for modeling organs like the brain [?], the heart [?], to model bones like the incudomalleal complex [?] or the femur [??]. Shape modeling, however, is relatively novel in food science.

To build a shape model, the correspondences between the surfaces in the object class have to be determined. One option is to annotate the corresponding points manually, but this is time-consuming and error prone. A more feasible option is surface registration. With this technique, corresponding points are automatically found by registering each object with the same template surface.

Current methods to build shape models of horticultural products are either based on 2D contour models [??], whereas only a limited number of views is characterized, or simplified 3D models based on contours [??]. The disadvantage of this technique is that the objects have to be star-shaped, so each point of the surface must be reachable with a straight line from a common center without intersecting the surface. In the work of ?, the shape of potato tubers is approached with ellipsoids, combined with spherical harmonics. However, the use of simple 3D geometrical shapes, such as a cylinders, spheres or ellipsoids, may be too restrictive to describe the complexity of object shapes.

? and ? approached the shape of a hazelnut by starting from a conceptual model, which was modified based on some measured features. With our suggested approach, the entire shape of the object is characterized. Therefore, our technique is applicable to more complex shapes, which may lead to better and more accurate decisions in the applications.

The main goal of our work is to introduce a surface registration framework that provides an accurate geometric fit while maintaining the correspondences and apply it to capture the shape variability of horticultural products [?]. Correspondences between the surfaces are obtained by elastic surface registration. An initial alignment step is added to improve correspondence compared to ?. With these correspondences, a model can be generated that is compact, (i.e. has few parameters), is highly specific, (i.e. only describes horticultural products of a certain class), but also with sufficient generalization ability to be able to describe new instances of that class.

The first part of the framework is 3D elastic surface registration to obtain correspondences. ? presented an algorithm in which each vertex is displaced separately by an affine transformation matrix. They introduced a stiffness parameter in the registration procedure, causing a vertex to be displaced along with its neighbors. During the iterations, the stiffness value is decreased, allowing a more elastic deformation, which results in a good geometric fit, but often suboptimal correspondences. In our approach, an initializing globally affine step is added. Therefore, using only translation of the vertices is sufficient. Furthermore, no landmarks are needed. Therefore, the overall computation time is reduced and the correspondence quality is improved [?]. In the second part of our framework, a shape model is built from the corresponded surfaces by performing principal components analysis (PCA) on the corresponding points of the population [?]. In this model, the mean surface and the main variations are incorporated. The last part is the parameterization of the statistical shape model. Because of the correspondences, any shape that can be formed by the model, can also be fit with CAD primitives and consequently can be used for finite element methods such as CFD, e.g. to simulate airflows in fruit packages.

6.2 Methods

In the following sections, the different steps for building a statistical shape model and describing this model with CAD primitives are explained.

6.2.1 Data Collection

Datasets of three types of fruit and vegetables were scanned in 3D to validate our algorithm. In particular, 30 Jonagold apples and 30 bell peppers were scanned using micro-CT. To this end, a set of 938 2D radiographic images were equiangularly acquired over 187 degrees and are reconstructed to a 3D tomography. The result is a 3D image that represents the X-ray attenuation properties of the scanned object. In this case, the data was acquired with a microfocus X-ray CT (AEA Tomohawk, Philips, The Netherlands) using a Philips HOMX 161 X-ray source. The resulting images had an isotropic voxel size ranging between 83 to 138 μ m. The outer surface of each instance was extracted from the reconstructed objects.

For the zucchini dataset, 52 instances were scanned with an Artec EvaTM structured light scanner, with a resolution of the scanner is 0.5 mm and an accuracy of 0.1 mm. This 3D scanner is able to acquire 2M points per second and has an angular field of

	apple	bell pepper	zucchini
width	82.28 ± 3.66	69.30 ± 11.41	83.36 ± 13.30
depth	81.81 ± 4.18	68.07 ± 11.81	70.17 ± 1.97
height	84.50 ± 4.74	84.23 ± 9.72	284.04 ± 38.71

Table 6.1: Average and standard deviation of the dimensions of the fruit and vegetables in *mm*.

view of $30 \times 21^\circ$.

The width, depth and height of the instances were measured. The average dimensions of the cultivars are shown in Table ???. All harvesting dates were within the optimal commercial picking window for each cultivar, as determined by the Flanders Centre of Postharvest Technology (VCBT, Belgium).

6.2.2 Building a Statistical Shape Model

Before bringing the surfaces into correspondence, the reference surface is rigidly aligned to the target surface by matching their principal axes. Then, the reference surface is registered to a target surface, such that the geometric distance between those surfaces becomes minimal while retaining optimal point correspondences. The approach is the same as the RN-ICP-T algorithm, which is also described in 2. Finally, a SSM is built from the corresponded surfaces.

6.2.2.1 Description with CAD primitives

For simulation applications, such as CFD and FEM environments, a shape must be representable with CAD primitives, which are basic geometric shapes such as spheres, cubes, toroids, cylinders, pyramids, and b-splines. These are considered to be primitives in 3D modeling because they are the building blocks for many other shapes and forms. To use a shape model of vegetables or fruit in a CAD environment, shape parameterization is needed.

Parameterization of a surface is the task of defining a map between the surface and a simple parameter domain, such as a plane, sphere, or cylinder. Such a map links each point of the surface with a coordinate in the space of the parameter domain. In this chapter, the surfaces are represented with a triangle mesh and the map is only defined explicitly for the vertices. Parameterization can be seen as the result of a continuous deformation of the surface into the parameter domain. By parameterizing the shape model, each instance in the model can be easily described with a set of basis functions, like spherical harmonics or B-splines.

The cylindrical parameter domain is chosen in order to be able to select the poles. Therefore, two holes are manually created in the top and bottom of the surface, to be able to work in this domain [?]. A mapping from the cylinder to the triangle mesh of the surface is needed. Therefore the surface mesh is represented by a progressive mesh. With this representation, the number of triangles is reduced until the simplest shape, an open prism with six vertices, is left. This simple shape can be easily parameterized by equidistant placement of its six vertices on the two boundaries of the cylindrical domain. The next levels in the progressive mesh are parameterized by inserting the removed vertices one at a time and optimizing their positions on the cylinder in a way that the mapping between the cylinder and the surface introduces a minimum of

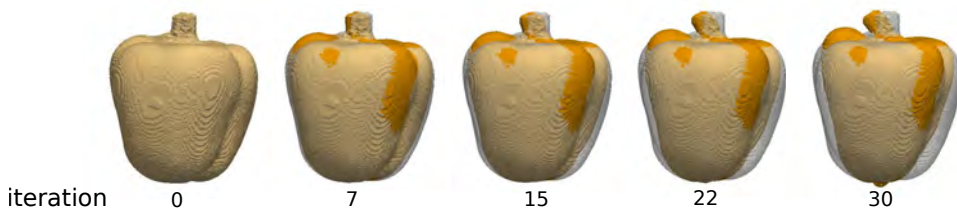


Figure 6.1: Iterative shape deformation of a reference bell pepper towards a target bell pepper. For each iteration, the deformed reference mesh in orange and the original reference mesh is visualized in light gray.

apple	bell pepper	zucchini
0.015 ± 0.011	0.106 ± 0.026	0.027 ± 0.007

Table 6.2: Average and standard deviation of the distance between the deformed reference surface and target surface in *mm*.

distortion. After re-inserting all vertices, the parameterization of the original surface surface is obtained and each vertex has a (u, v) coordinate in the cylindrical coordinate system.

The statistical shape model is parameterized by only parameterizing the average surface. Because of the correspondence, all instances of the model also have B-spline parameter coordinates. With this technique, the point-based models can be described by B-splines, which describe a surface by a set of control points. The 3D locations of the control points are optimized to obtain the best surface approximation. This is a very compact representation and is suited for CAD and finite-element environments.

6.3 Results and Discussion

6.3.1 Surface Registration

To obtain meaningful correspondences, a reference surface was registered to each surface of the population. For each class, a reference surface was randomly chosen from the population. The apple was resampled to 30000 points, the bell pepper to 40000 points and the zucchini to 13000 points. The reference surface of each class was registered to each surface of the population. The stiffness parameter decreased linearly from 50 to 1. Registering one instance took ± 1 *min* CPU time for 30 iterations. Then, the average surface was calculated and served as a new template surface to register to each instance to avoid a bias towards a specific shape of the population. In Figure ??, the deformation of the reference surface to a target surface of the bell pepper object class is visualized through the iterations. From the results of this registration, a statistical shape model was built.

The average error between the source surface and the deformed reference surface for each class is shown in Figure ?? and summarized in Table ?. The largest errors appeared around the top of the surfaces, where the stem was located. The bell pepper surfaces had the largest errors, because the shape and length of the stem greatly varies over the instances.

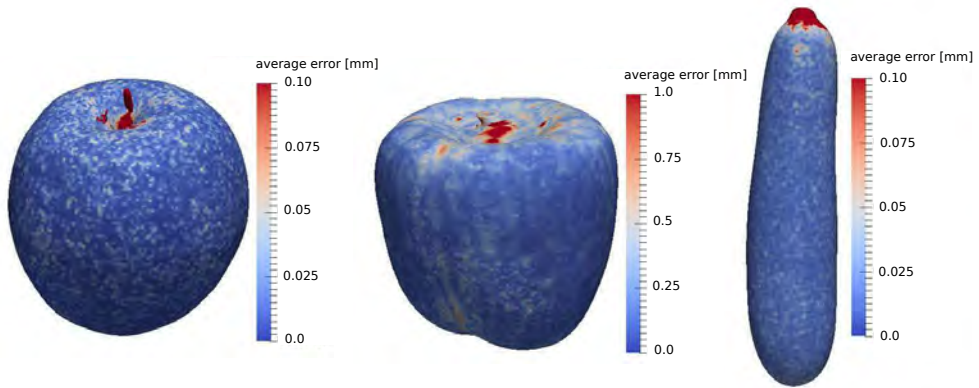


Figure 6.2: Geometric error maps of the apple, bell pepper and zucchini. The errors were calculated for each instance in the population and averaged per object class.

stem	bottom	average
3.97 ± 2.60	4.84 ± 3.15	4.41 ± 2.32

Table 6.3: Average and standard deviation of the distance between the manually annotated markers and automatically derived markers from the shape model on 10 bell pepper instances in *mm*.

The correspondence quality was evaluated for the bell pepper model by manually placing a marker on the top (of the cut off stem) and a marker on the bottom of the input surfaces. Those marker points were also annotated on the average surface and loaded on each instance incorporated in the model. Next, the Euclidean distance between the manually placed marker and automatically loaded marker was calculated. The results of this analysis are shown in Table ??.

The correspondence error on the bottom of the bell pepper is relatively high. It is difficult to manually annotate this point, because there are no clear features on the bottom of a bell pepper, so the inter- and intra observer errors are large. Moreover, because there are no distinct features on the bottom, even for suboptimal correspondences the similarity criteria, such as the directions of the normals have to be in the same direction within a tolerance of 30° , are easily achieved. Once a bad correspondence is found, it is very unlikely that the algorithm is capable of correcting this.

The geometric and correspondence errors can perhaps be reduced by adding more vertices to the reference surface or lowering the convergence ratio. The more vertices on the reference surface, the better a shape can be captured. However, computation time and memory requirements increase with the number of vertices. Lowering the convergence threshold could possibly lead to better results on the stem and bottom.

6.3.2 Shape Model

In Figure ?? the first five shape modes of the bell pepper shape model are visualized, since these modes represent over 80% of the variation. The first mode represents

mainly the size of the bell pepper. The second mode shows the ratio between width and height. The third mode describes the location and curvedness of the lobes. The characteristics described in the following modes are harder to interpret. They mostly describe the curvature of the bottom of the bell pepper.

It is assumed that a statistical shape model describes a multidimensional Gaussian distribution of the object's shape. As an example, the model was truncated to 5 eigenmodes, because the first components mostly describe the shape. Five samples were randomly generated by generating a weight vector \mathbf{b} . These weights were between +3 standard deviations and -3 standard deviations of their respective shape mode and followed the Gaussian distribution. Some randomly generated instances are visualized in Figure ??.

6.3.3 Description with CAD primitives

Surface parameterization was applied to the average surface of the apple shape model to be able to describe each model instance with basis functions. In Figure ??, the average apple surface with iso-parametric curves is shown. The apple surface was approximated by B-splines with different numbers of control points. While the size and global shape of an apple can already be described with a 4×4 grid of control points, the difference between the original and the approximation was clearly visible. An approximation with 32×32 control points was nearly identical to the original apple model. Therefore the parameterized shape model could serve as a model in CAD and finite-element environments, so simulations could be performed with these models.

Moreover, the parameterized shape model is a much more compact and memory efficient representation of the triangle model. For example, the triangle model of the apple consisted of 30000 points requiring 703 *kB* of storage per surface. On the other hand, the most detailed parameterized apple shape consisted of 32×32 control points only requiring 24 *kB* per surface. So the required memory for the parameterized shape is almost 30 times smaller than for the triangle model. In addition, for the triangle model the vertex connectivity has to be stored while for the B-spline representation the connectivity is implicit.

6.3.4 Model Performance

Compactness, generalization ability and specificity are widely used measures [??] for quantifying the correspondence quality of a statistical shape model. In this section, the different model performance measures were calculated per object type.

6.3.4.1 Compactness

A compact model is a model that can represent all shapes of the class with as little parameters as possible. Preferably, a shape model can be described with few modes. The compactness is expressed as the sum of variances of the model,

$$C(m) = \sum_{i=1}^m \lambda_i,$$

where λ_i is the variance in shape mode i , and $C(m)$ is the compactness using m modes.

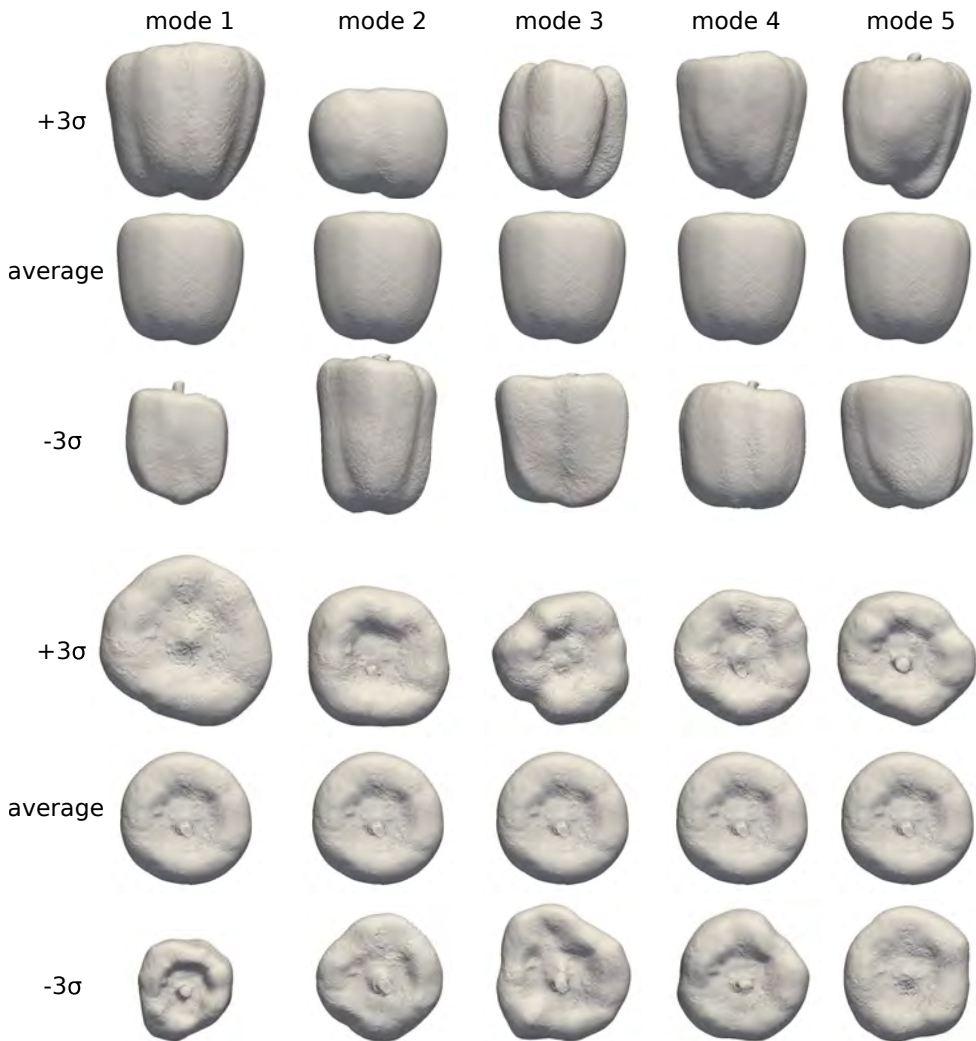


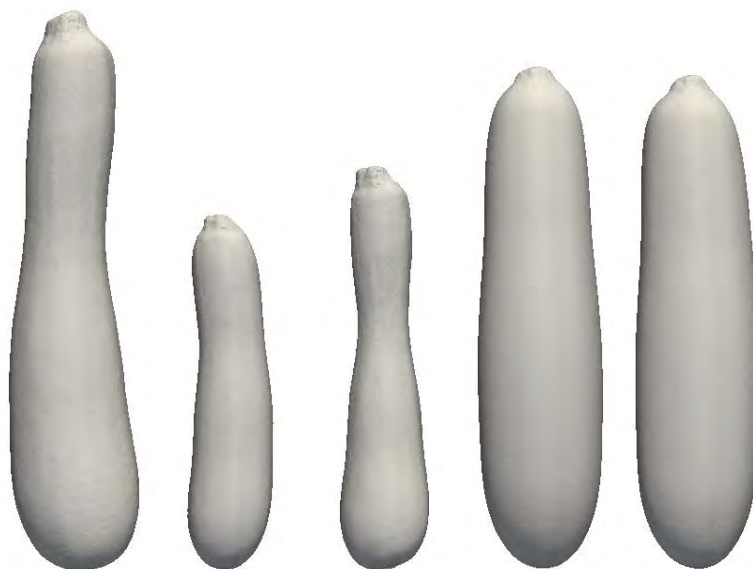
Figure 6.3: A front view and a top view of the first five shape modes of the bell pepper shape model, plus and minus three standard deviations.



(a) Five randomly generated apple instances.



(b) Five randomly generated bell pepper instances.



(c) Five randomly generated zucchini instances.

Figure 6.4: Randomly generated horticultural products, created by applying a random weight vector to the first 5 eigenmodes of the shape model.

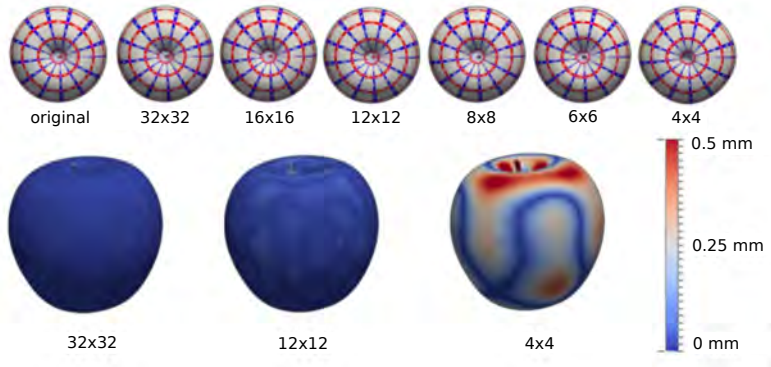


Figure 6.5: Upper row: top view of parameterized apple shape model with iso-parametric curves. B-spline approximations with different number of control points on the B-spline grid. Bottom row: distance, in mm between the original surface and the approximation.

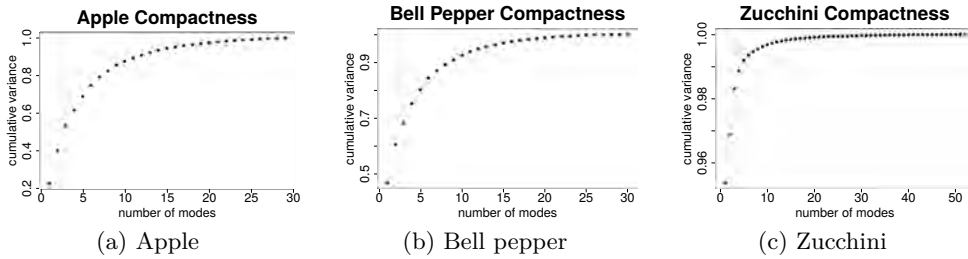


Figure 6.6: The compactness measure for the three types of horticultural products. The cumulative variance was normalized for each model so that the total was 100%.

In Figure ??, the compactness graph for each object class is shown. The cumulative variance was normalized for each model so that the total was 100%. The compactness test shows that the apple model captured more than 85% of the shape variation with the first 10 modes. The bell pepper model captured more than 90% of the shape variation with the first 10 modes.

Note that the zucchini model is a very compact model, since only 5 modes were needed to describe over 99% of the total population. This is because the main shape variance is size, which was described by the first mode.

6.3.4.2 Generalizability

Generalizability is defined as the degree to which the model can be generalized from the study sample to the entire population. The shape model should allow to describe all shapes of the specific class, and not only the shapes of the training set. If a model is over-fitted to the training set, it will not be able to generalize to unseen samples. Generalizability $G(m)$ was measured by performing leave-one-out tests, where a shape model was built by using all training shapes but one. Next, the left-out shape was described by adapting the shape parameters of the model. Generalizability was calculated as the mean error over all left out shapes,

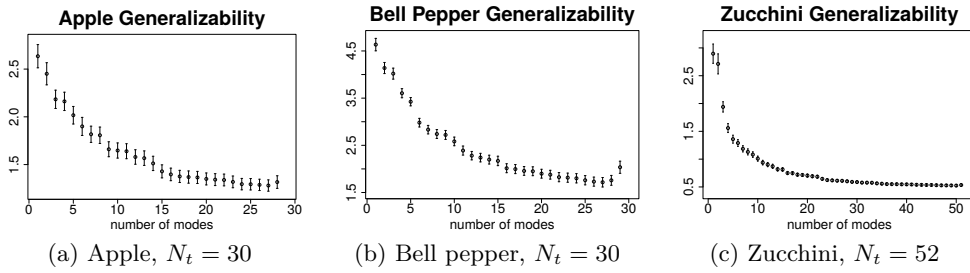


Figure 6.7: The generalizability measure for the three types of horticultural products, in mm per vertex. The error flags represent the standard errors on the mean distance.

$$G(m) = \frac{1}{N_t} \sum_{i=1}^{N_t} \|\mathbf{x}_i - \mathbf{x}'_i(m)\|^2,$$

where \mathbf{x}_i is the left-out shape and $\mathbf{x}'_i(m)$ is the attempted description using the shape model with m modes. The number of trials, or objects in the model, is represented by N_t .

In Figure ??, the generalizability graph for each object class is shown. The generalizability error was calculated in mm per vertex. The error of fitting the apple model to an unseen apple surface was smaller than $1.9 mm$ from 5 shape modes. For the bell pepper shape model, an error of less than $3.5 mm$ occurred when predicting a shape using the first 5 shape modes. The outer surface of a zucchini could be fit with an error of $1.6 mm$ from 5 modes.

6.3.4.3 Specificity

A specific model can only represent instances of the object class that are similar to those in the training set. Specificity was measured by generating an amount of shapes (N_t) by generating a random parameter vector with m modes. Each sample was compared to the most similar shape in the training set. The specificity measure can be expressed as,

$$S(m) = \frac{1}{N_t} \sum_{i=1}^{N_t} \|\mathbf{y}_i - \mathbf{y}'_i(m)\|^2,$$

where \mathbf{y}'_i are shape examples generated by the model and \mathbf{y}_i is the nearest member of the training set to \mathbf{y}'_i .

In Figure ??, the specificity graph for each type of surface is shown. The specificity error was calculated in mm per vertex. The specificity test proved that all three models were able to generate shapes that resemble those in the training set.

6.3.5 Discussion

The most innovative feature of this algorithm is that it leads to accurate statistical shape models of objects with complex, possibly non-star shaped topologies. The shapes were described in a detailed, realistic way, compared to the current 2D contour models or simplified 3D models based on contours. The algorithm is applicable to

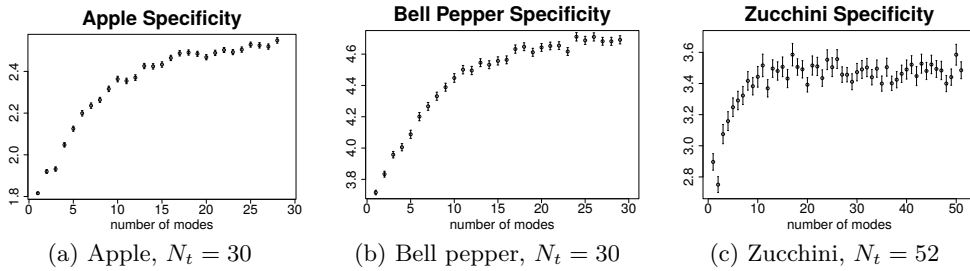


Figure 6.8: The specificity measure for the three types of horticultural products, in *mm* per vertex. The error flags represent the standard errors on the mean distance.

vegetables and fruit with a shape more complex than star-shaped [?]. Star-shaped means that each point of the surface is reachable with a straight line from a common center without intersecting the surface, which was not the case for some of the bell pepper instances. Therefore, the algorithm can also be applied to e.g. mushrooms and bananas.

By applying surface registration to a dataset, all instances were in correspondence with each other. The geometric errors and correspondence errors between the deformed reference surface and the target surface were small, so the registration result is a good representation of the input surface. Geometric and correspondence errors could possibly be reduced by changing the stiffness parameters. A small stiffness value leads to a better geometric fit, because the vertices can move more freely to the optimal position. On the other hand, chances are higher that a vertex migrates to an incorrect location because of this freedom. Once a bad correspondence is found and the surface is incorrectly deformed, the algorithm is not capable of correcting this mistake. A large stiffness value leads to a less optimal geometric fit, but the overall shape of the source surface is maintained, increasing the chances of a good correspondence. Other possibilities to reduce the errors are increasing the number of vertices and a more strict convergence criterion.

The algorithm was capable of rapidly generating 3D statistical shape models that were accurate and compact, while the randomly generated surfaces were similar to the surfaces of their respective training sets. Therefore, a broad dataset of realistic instances can be produced for e.g. simulation purposes.

B-spline surface approximation of the shape model was shown. Because the model was parameterized, all instances that can be formed by the model were also parameterized. Therefore, a statistical shape model can provide input to generate CAD models, which can be loaded in CFD and FEM environments. As a result, the shape model is employable in stacking algorithms [?]. Moreover, the parameterized shape model is a more compact representation of the triangle model, as less numbers have to be stored. The software for the described algorithms was written in C++ and based on the Visualization ToolKit (VTK) libraries [?]. VTK is an open source software system for 3D computer graphics, image processing, and visualization.

6.4 Conclusions

In this chapter, an algorithm for building a statistical shape model of horticultural products was proposed. First, the surfaces from the training set were brought into correspondence with each other. Experiments on the surface registration algorithm proved that the technique is applicable to complex shapes and results in a good geometric fit and good correspondences. From these corresponded surfaces, the statistical shape model was built. The model performance tests showed that our method for building a statistical shape model results in a good representation of the population of the object class, as the shape model is able to generate realistic horticultural product shapes that differ from those in the training set. Furthermore, the model was a compact representation of the shape population and could easily generalize to a formerly unseen instance of the model's object class.

By parameterizing the surface, the shape model and every instance that can be formed by the shape model, were described by CAD primitives. Therefore, a statistical shape model is an effective tool for simulation software. Our approach of modeling and subsequent parameterization is also applicable to other horticultural product shapes. Specifically for elongated shapes, like pears, bananas, and cucumbers, cylindrical parameterization can be useful.

The developed surface registration and modeling techniques proposed in this chapter are also applicable to other horticultural products of more complicated, non-spherical topology.

Acknowledgements

This work was supported by the Agency for Innovation by Science and Technology in Flanders (IWT SB 141520 and IWT SBO 120033 TomFood).

This work was previously published as:

Danckaers, F., Lacko, D., Verwulgen, S., De Bruyne, G., Huysmans, T., and Sijbers, J. (2018). A Combined Statistical Shape Model of the Scalp and Skull of the Human Head. In Advances in Intelligent Systems and Computing, volume 591, pages 538–548. Springer, Cham.

7

Building a combined statistical shape model of the scalp and the skull of the human head

Contents

Abstract	88
7.1 Introduction	89
7.2 Methods	90
7.2.1 Segmentation	90
7.2.2 Statistical shape model (SSM)	91
7.3 Experiments and Results	91
7.3.1 Segmentation	91
7.3.2 Statistical shape model (SSM)	91
7.3.3 Model performance	92
7.3.4 Generalizability	94
7.4 Discussion	95
7.5 Conclusion	96

Abstract

In this chapter, we describe a framework to build a combined statistical shape model (SSM) of the outer surface of the scalp and the inner and outer surface of the skull of the human head. Such an SSM is a valuable tool when designing headgear, as it captures the variability of head geometry of a given population, enabling detailed analysis of the relation between the shape of the scalp and the skull. A combined SSM of the head may allow to work towards population based Finite Element (FE) models e.g. for safety and comfort predictions when wearing headgear. Therefore, a correspondence between the skull and scalp surfaces, originating from MRI scans, is determined using elastic surface registration. The combined SSM shown to be compact, to be able to generalize to unseen instances by adjusting the shape parameters and to be shape specific. Therefore, we can assure that, by adjusting the shape parameters, a broad range of realistic head shapes can be formed.

7.1 Introduction

A statistical shape model (SSM) of the human head is a valuable tool to design headgear, because it captures the variability of head geometry of a population. SSMs are built from 3D scans of a population of shapes. Therefore, they contain much more information than traditional anthropometrical measurements. When designing headgear, SSMs can be employed for ergonomic optimization warranting an optimal fit of the product to the geometry of the head, for a target population [?].

Insight in 3D skin and bone thickness of the human head for specific populations may help to avoid local peak pressure on the head while wearing a helmet in future helmets. Additionally, it may enhance the accuracy of Finite Element (FE) models of the human head that aim at predicting brain damage. The soft tissue layer is expected to be a contributing parameter in the kinematics of head movement during head impact to affect rotational acceleration and velocity of the human brain. The bone tissue layer is a contributing parameter in the prediction of linear acceleration of the human brain during head impact.

A combined SSM of the head may allow to work towards population based FE models for safety and comfort predictions when wearing headgear. Such an FE head model can be used in simulations, to predict the impact on the head in accidents that cause trauma injuries to determine regional responses [????]. Typical FE head models are based on one head shape or the average head, calculated from a population [???]. A typical example is the Strasbourg University Finite Element Head Model [??]. This is a very detailed FE model of the human head, with many internal structures included, and based on a single skull. By building an FE model from an SSM, it is adjustable in shape [??], what can lead to more accurate, customizable FE models. Such a statistical FE model is especially useful when designing helmets [??], because the impact on the head in an accident can be studied on different shapes and sizes of human heads, and thus improve the biofidelic characteristics of current FE head models for impact.

Most SSMs of the head only describe the outer skin layer of the head and do not contain information about the thickness of the scalp and the skull [???], while this information is important for e.g. predicting local skin pressure on the head. ? constructed a combined SSM of the face shape and soft tissue depths for forensic facial reconstruction on an unidentified person's skull. Their technique is labor-intensive, as the researchers had to place manually indicated anatomical landmarks on the surface and measure soft tissue depths at 52 locations.

In this chapter, we describe a technique for building a combined SSM of the human head, more specifically, the outer surface of the scalp and the inner and outer surface of the skull. The chapter is organized as follows. First, the segmentation of the 3D surfaces from the MRI scans is detailed. Second, the construction of a combined SSM is explained. Next, in the results section, the SSM is subject to quality tests to evaluate the model's compactness, generalizability and shape specificity. Finally, the results are discussed and a conclusion is formulated.

7.2 Methods

Scalp and skull surfaces are separately segmented from MRI datasets. A reference mesh (a uniformly resampled surface from the dataset) is constructed for the scalp and for the skull, and is registered to all input meshes of each layer, to obtain a

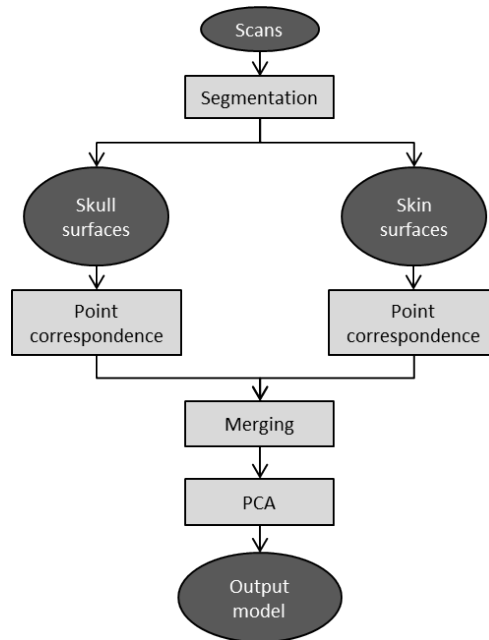


Figure 7.1: Framework for building a combined SSM of the skull and scalp.

homologous point-to-point correspondence. Next, an average mesh is calculated for both the scalp and skull and used as template to register the input scalp and skull meshes for the second time to prevent a biased result. Then, the registered scalp and skull of each subject are merged again. A combined SSM is built using Principal Components Analysis (PCA) on the corresponded heads. In this SSM, the average surface and skull thickness, and the main variances are incorporated. The process is shown in Figure ??.

The training population consisted of 85 MRI T1-FFE-weighted scans (male and female, aged between 20 and 40 years, Western Population) originating from the International Consortium for Brain Mapping (ICBM) database [?]. The scans were acquired using a Philips ACS III 1.5 T scanner in the sagittal acquisition plane, with a slice thickness of 1 mm, an echo time of 10 ms, a repetition time of 18 ms and a flip angle of 30° .

7.2.1 Segmentation

From magnetic resonance imaging (MRI) scans, the scalp and the skull are separately segmented using the Statistical Parametric Mapping (SPM12) [?] package from MATLAB and converting the outcome to 3D meshes. The skin corresponds with layer 3 and the skull corresponds with layer 4 in SPM12. Scalp and skull were constructed separately by segmentation as different surfaces, because finding correspondences between nearby components is error-prone.

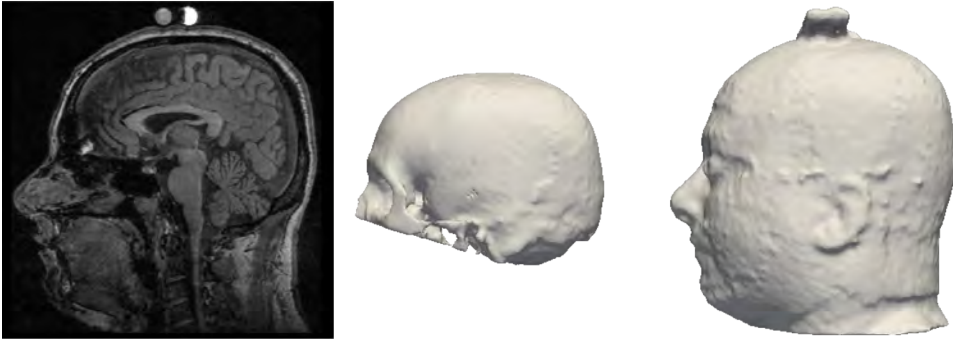


Figure 7.2: Slice of a head scan and a segmented scalp and skull. Note that the skull is not fully segmented, because SPM12 focuses on the brain. A bar is noticeable on the top of the head.

7.2.2 Statistical shape model (SSM)

In this section, the methodology to build a combined skull/scalp SSM is described. The algorithm is based on a previously developed elastic surface registration algorithm ?. The first part of the framework is surface registration. The registered surfaces are used in the second part of the framework, where an SSM is built. The method is applicable to other layered surfaces as well.

7.3 Experiments and Results

In this section, the results of the framework are described.

7.3.1 Segmentation

In the dataset, none of the skulls were completely segmented, because the SPM12 package was constructed with a focus on brain mapping and works with a spatially limited skull template. The dataset was sufficient for our research, because we work on comfort of helmets and therefore focus on the upper part of the head. A slice of the head of a test subject and the resulting skull and scalp surfaces are shown in Figure ???. Note that in some scans a bar is visible on the top of the head, because the heads of the subjects from the ICBM are fixated. This bar is not visible in the model, because a smooth template surface served as input for the elastic surface registration to reduce protrusions and other irregularities. Remaining irregularities were averaged out by calculating the SSM.

7.3.2 Statistical shape model (SSM)

The scalp and the skull were separately segmented from each head scan, and were both registered by the same template surfaces. The skull template surface was uniformly resampled to 100041 vertices, the scalp template surface was uniformly resampled to 89389 vertices. After the surface registration, both scalp and skull of the same subject were merged to become a combined surface, as shown in Figure ???.

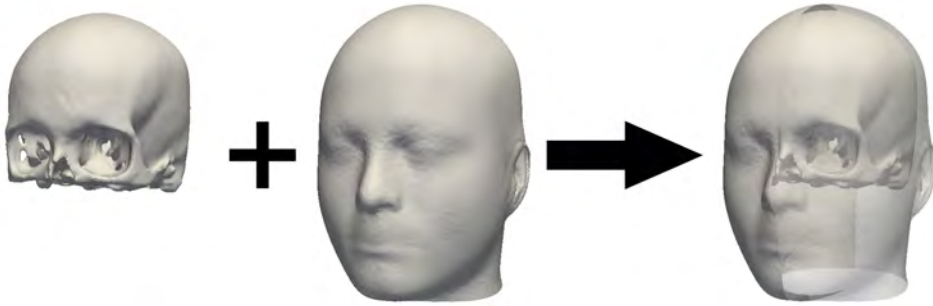


Figure 7.3: Uniting the separate skull and scalp from Figure ?? to result in a combined surface.

In Figure ??, the first three PC modes of the SSM, built from combined surfaces, are shown. These shape modes describe the shape variations inside the population. The first mode describes mainly the size of the head, the second mode describes the width-length ratio of the head, and the third mode describes mainly the curvedness of the skull.

7.3.3 Model performance

Compactness, generalization ability, and specificity are widely used measures [??] for quantifying the correspondence quality of an SSM. In this section, the different model performance measures were calculated for the combined SSM and the separate SSMs of the skull and the head.

7.3.3.1 Compactness

Compactness of a shape model is a measure how well a shape from the population is described by a limited amount of PC modes. Preferably, an SSM is approximated well with few modes. The compactness is expressed as the sum of variances of the SSM:

$$C(m) = \sum_{i=1}^m \lambda_i,$$

where λ_i is the variance on the vertex locations in shape mode i , and $C(m)$ is the compactness using m modes. The results are shown in Figure ?. To describe over 80% of the shape variation inside the population of combined head shapes, six shape modes were needed. Thirteen shape modes describe over 90% of the shape variation. Therefore, our combined SSM is a compact representation of the population.

An example of a surface represented by different numbers of modes is shown in Fig. 6. Using more parameters led to a shape that looked more like the original shape. The more parameters that are used to reconstruct a shape, the less difference is noticeable. Fig. 6. Shape generated with a different number of shape modes. Note the difference in shape of the cheekbones and jaw. The difference between a surface reconstructed by 16 shape modes and 32 shape modes is minimal.

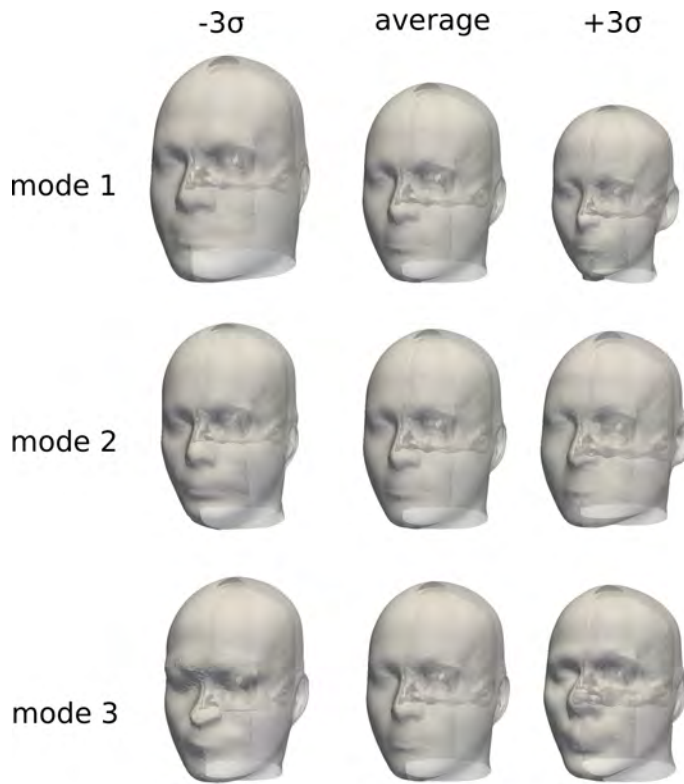


Figure 7.4: First three eigenmodes of the combined SSM of the human scalp and skull.

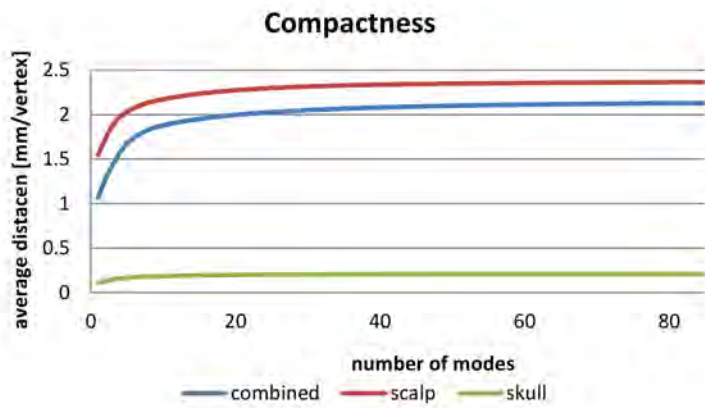


Figure 7.5: Compactness graph. The average deviation from the mean shape to describe shapes with a specific number of shape modes is shown.

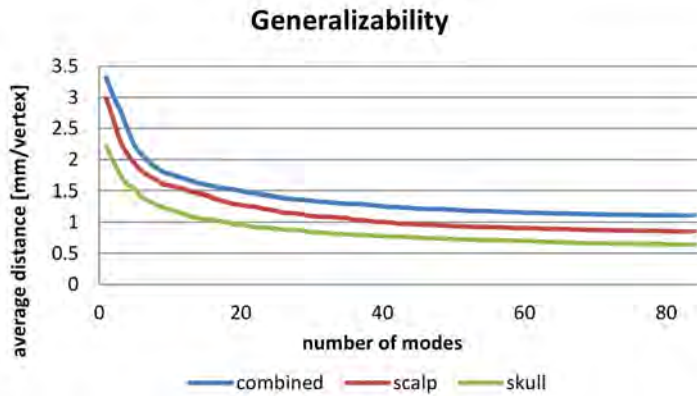


Figure 7.6: The generalizability measure, in mm per vertex. The error flags represent the standard errors on the mean distance.

7.3.4 Generalizability

Generalizability relates to how well the SSM can generalize to a formerly unseen head shape. The SSM should be able to describe all head shapes, not only the head shapes of the training set. If an SSM is over-fitted to the training set, it will not be able to generalize to unseen samples.

Generalizability $G(m)$ was measured by performing leave-one-out tests, where a shape model was built by using all training shapes but one. Next, the left-out shape was described by adapting the shape parameters of the model. Generalizability was calculated as the mean error over all left out shapes,

$$G(m) = \frac{1}{N_t} \sum_{i=1}^{N_t} \|\mathbf{x}_i - \mathbf{x}'_i(m)\|^2,$$

where \mathbf{x}_i is the left-out shape and $\mathbf{x}'_i(m)$ is the attempted description using the shape model with m modes. The number of trials, or objects in the model, is represented by N_t .

In Figure ??, the generalizability graph is shown. The generalizability error was calculated in mm per vertex. The error of fitting a scalp and skull to an unseen instance was $2.2mm$ from five shape modes. Using 20 shape modes, the error was smaller than $1.5mm$. Note that the error for the scalp and skull separately was smaller than the error of the merged surface. This can be explained by the fact that the shape of both scalp and skull were dependent on each other. In future work, we will improve this by corresponding the scalp and skull together instead of corresponding them separately.

7.3.4.1 Specificity

A specific SSM can only represent instances of the object class that are similar to those in the training set. This was measured by generating an amount of shapes ($N_t = 1000$) by generating a random parameter vector with m modes. Each sample was compared to the most similar shape in the training set. The specificity measure

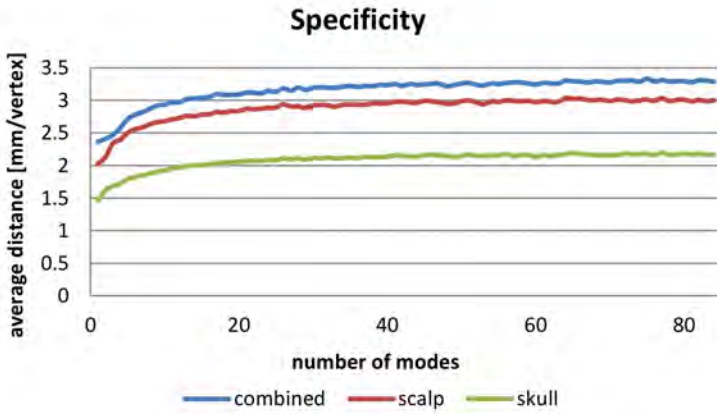


Figure 7.7: The specificity measure, in mm per vertex. The error flags represent the standard errors on the mean distance.

can be expressed as

$$S(m) = \frac{1}{N_t} \sum_{i=1}^{N_t} \|\mathbf{y}_i - \mathbf{y}'_i(m)\|^2,$$

where \mathbf{y}'_i are shape examples generated by the model and \mathbf{y}_i is the nearest member of the training set to \mathbf{y}'_i .

In Figure ??, the specificity graph is shown. The specificity error was calculated in mm per vertex. The specificity test proved that our SSMs were able to generate shapes that resemble those in the training set, even though they differ from the shapes in the training set. The specificity error for the combined SSM is greater than the error for the separate SSMs. This means that the combined SSM represented more shape variation.

7.4 Discussion

This combined SSM can be used as a virtual ergonomic 3D mannequin in Computer Aided Design (CAD) environments or as input for Finite Element (FE) and Computational Fluid Dynamics (CFD) simulations, when designing headgear. For example, it can be exploited in mass customization of all kinds of headgear systems that are built from FE models predicting local pressure. Another application is the development towards patient specific FE head impact models that may give more insight in brain damage due to accidents and can guide medical staff members during brain surgery. The SSM is a compact representation of the population, because only six shape modes were needed to describe over 80% of the shape population. The model is able to generalize to an unseen instance, as six modes were sufficient to describe the instance with a mean error of $2.08mm$. A randomly generated shape using six shape modes is object specific, but differs from the dataset, since the average distance between a randomly generated object using six shape modes and the most similar object in the dataset was $2.77mm$. For helmet designing, a generalizability error of less than $1mm$

is preferable. Our current model has a generalizability error of $1.1mm$ when all shape modes are used to deform the model to an unseen head shape.

7.5 Conclusion

In this work, we proposed a technique to perform statistical shape analysis on combined surfaces of the scalp and skull. Therefore, the relation between the scalp and skull can be analyzed. The constructed combined SSM is compact, so it can represent heads with a limited number of parameters with acceptable accuracy. Furthermore, we have proven that the combined SSM is able to generalize to unseen instances and is shape specific. Therefore, we can assure that by adjusting the shape parameters, a broad range of realistic head shapes can be formed. Our presented method is also applicable to other layered shapes.

The correspondences in the current SSM were split up in a skull part and a scalp part and merged for building a PCA model.

Acknowledgements

This work was supported by the Agency for Innovation by Science and Technology in Flanders (IWT-SB 141520 and IWT 140881).

This work was previously published as:

Soons, J. A., **Danckaers, F.**, Keustermans, W., Huysmans, T., Sijbers, J., Casselman, J. W., and Dirckx, J. J. (2016). 3D morphometric analysis of the human incudomalleolar complex using clinical cone-beam CT. *Hearing Research*, 340:79–88.

8

3D morphometric analysis of the human incudomalleolar complex using clinical cone-beam CT

Contents

Abstract	98
8.1 Introduction	99
8.2 Methods	100
8.2.1 Data acquisition	100
8.2.2 Individual model generation	100
8.2.3 Statistical shape modeling	101
8.2.4 Quantitative data of anatomical features	104
8.3 Results	104
8.3.1 Statistical shape model	104
8.3.2 Anatomical features	105
8.3.3 Correlations	108
8.4 Discussion	108
8.4.1 IM complex measures	108
8.4.2 Cone beam CT	113
8.4.3 Statistical shape modeling	113

Abstract

Human middle ears show large morphological variations. This could affect our perception of hearing and explain large variation in experimentally obtained transfer functions. Most morphological studies focus on capturing variation by using landmarks on cadaveric temporal bones.

We present statistical shape analysis based on clinical cone beam CT (CBCT) scans of 100 patients. This allowed us to include surface information on the incudomalleolar (IM) complex (joint, ligaments and tendon not included) of 123 healthy ears with a scanning resolution of $150\mu m$ and without a priori assumptions. Statistical shape modeling yields an average geometry for the IM complex and the variations present in the population with a high precision.

Mean values, variation and correlations among anatomical features (length of manubrium, combined length of malleus head and neck, lengths of incus long and short process, enclosing angles, ossicular lever ratio, incudomalleolar angle, and principal moments of inertia) are reported and compared to results from the literature. Most variation is found in overall size and the angle between incus and malleus. The compact representation provided by statistical shape modeling is demonstrated and its benefits for surface modeling are discussed.

8.1 Introduction

Human middle ears show large variations [???]. These variations can affect sound transmission, possibly explaining the large variations found in experiments [?] and affect our individual perception of hearing. Nowadays, middle ear computational (finite element, FE) models [?????] are typically based on tomographic data such as CT, MRI, or histological sections [??] and they are used to predict and understand sound transmission. Some studies investigate the effect of adding more detail on certain middle ear structures. These details can have important effects for middle ear functioning: e.g. the synovial joints [?], the malleus-tympanic membrane connection [?], and high resolution scans of soft tissue [?]. Improving our knowledge of these key structures is important. Nevertheless, it is also important to study the effects of variation and uncertainty to understand normal, pathological, or reconstructed middle ear functioning. For material parameters, this can be done by a sensitivity analysis of the involved parameters [????]. The model geometries of current models, however, are mostly based on data from a single or a few specimens.

Two exceptions to the preceding statement are the study of ? and the study of ?. Each study uses a different approach to incorporate geometric variation, but they did not report on the effect for sound transmission. ? showed that it is possible to construct basic 'patient-specific' finite element models based on clinical CT scans (slice thickness $0.625\mu m$) of 31 subjects with normal hearing. Due to the low resolution of their CT scans they lack important details in the model such as tympanic membrane thickness and an incudomalleal (IM) joint. These issues can be overcome by using a parametric hybrid approach. For example the model of ? is based on μ CT images so they can include these important morphological details. Next, their model geometry was made parametric by manually chosen landmarks (distinctive points and dimensions) by a priori assumptions on geometry variation. Finally, the geometric parameters were obtained by fitting this parametric model to clinical cone-beam CT data. Also, some important work has been done by ?. They report of a method for applying a piecewise affine-initialized thin-plate spline transformation to a high-quality model of the middle and inner ear. Their results indicated that minimally supervised model computation for the guidance of ear surgery is feasible.

We now propose a new technique that uses statistical shape models (SSM) to capture these shape variations. In this way we avoid a priori assumptions about morphology. We will show that the principal components (PC) of the SSM approach will allow us to capture and report the natural anatomical variations in the human population. In this work clinical cone beam CT (CBCT) data has been used to capture the IM complex in 100 patients.

As compared to non-clinical μ CT, the resolution and SNR of CBCT is much lower and CBCT cannot be combined with staining protocols. μ CT, on the other hand, can only be used on cadaveric temporal bones [???]. To build a realistic model, this detailed information obtained from temporal bone studies (histological sectioning, stained μ CT) will be needed. Nevertheless, the use of CBCT allows us to get access to clinical data and much larger inter-human variation in middle ear morphology can be captured. Moreover, this could enable clinical applications in the future. Specifically, the low resolution data coming from the CBCT of an individual can be used to generate the 'true' shape of the individual's ossicles by fitting the low res image to the statistical shape model. In this way, it may become possible to pre-operatively prepare custom made prostheses ossicles, especially now micro-3D printing techniques

are coming of age.

The advantages of CBCT over conventional clinical fan beam CT include a lower radiation dose for the patient and a better spatial resolution (in our case $150\mu m$). This provides a more reliable morphologic assessment of middle ears [?]. The disadvantage is the vulnerability to motion artefacts, the longer acquisition time and the lack of Hounsfield units [?].

In this chapter, we report the IM complex shape variations obtained in vivo by using CBCT scans. Mean values and variations of anatomical features will be compared to the literature and the correlations among these measures will be assessed. Finally, the advantages of using the SSM approach in geometry representation and its implications for future FE implementation will be discussed. In particular, it's these FE models that in a later stage will allow us to make further conclusions (e.g. about the functional form).

8.2 Methods

8.2.1 Data acquisition

In this study, clinical cone-beam CT scans of 100 patients were analyzed retrospectively. A NewTom 5G, QR Systems (Italy) with an amorphous silicon flat panel of 20 x 25 cm, a scan field of view of 15 x 8 cm, a voltage of 100 kV resulting in $150\mu m$ spatial resolution was used. Both temporal bones scanned at the same time for patients with various pathologies. This study was approved by the ethics committee of AZ Sint-Jan, Bruges, Belgium (BUN: B049201525222) and all data was anonymized. Diseased ears, e.g. fluid filled, were excluded from this study resulting in a total of 147 healthy middle ears. The average subject age was 51 years with a standard deviation of 17 years (minimum age is 19, maximum is 86). The group included 50 Females and 50 males.

8.2.2 Individual model generation

First, 3D surface triangulated geometrical models were constructed for the 147 middle ears by specifying the portion (segmentation) of each slice image belonging to IM complex using Amira software (version 5.3). This was done in a semi-automatic way by selecting grayscale values above 500. Where necessary, the ligaments of incus and malleus were removed from the segmentation. Occasionally, parts of stapes head and neck also had higher grayscale values and a manual segmentation was needed. On the other hand, the manubrium and/or distal end of the long process of the incus sometimes had lower grayscale values, in this case these features were added manually. Triangulated surface models were created by using a marching cubes algorithm (surfacegen module). Subsequently, these surface models were smoothed by shifting vertices to the average position of neighbors (smoothsurface module) and decimated to about 3000 vertices, as shown in Figure ???. All ears are transformed to left ears.

8.2.3 Statistical shape modeling

Next, a dense correspondence between the CBCT samples was obtained by pair-wise elasticity modulated registration [?].

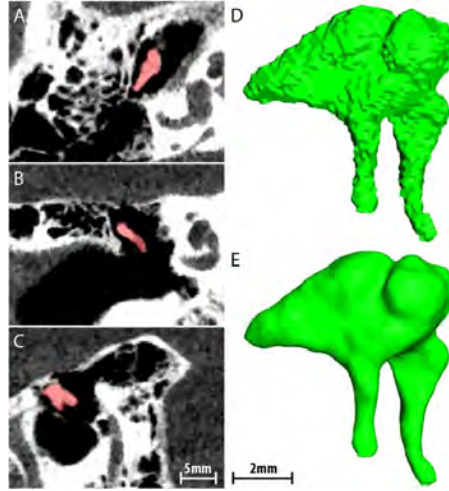


Figure 8.1: Geometric model generation (patient #71, right ear). IM joint in (A) transverse plane, (B) coronal plane and (C) sagittal plane, IM complex is labeled in red. (D) Unsmoothed and (E) smoothed 3D geometrical surface model of IM complex after segmentation.

The correspondences were obtained in three steps:

1. a reference surface was selected and registered to 70 middle ear samples. This reference was a smooth surface with distinct features, which had been uniformly resampled and made watertight,
2. a new reference surface with strongly reduced bias was generated by spatially averaging the 70 shapes. The corresponded shapes were aligned by Procrustes analysis. For each surface point of the middle ear, the average point per set of corresponding points was calculated.
3. the reference was successfully registered to 123 middle ears. First, an initial global rigid registration is obtained. Then, a global rigid registration and an elasticity modulated registration are iteratively repeated. During the iterations, the stiffness gradually decreases, such that the surface will become more elastic through the iterations.

24 middle ears were excluded, because of the difficulty to find correspondence between rod like protuberances, such as incus long process. This is because the algorithm searches for corresponding points by casting a normal ray from the template surface to the target surface. If ILP of the template surface is much longer than ILP of the target surface, no correct corresponding points will be found near the end of ILP. This issue will be further explored in future work.

An SSM was built from these corresponding scans by applying principal component analysis (PCA) on the points of the corresponded surfaces, describing the average shape and the main variations of the middle ear within the CBCT population. To build such an SSM, it is important that the surfaces are superimposed by optimally translating and rotating the surfaces. The optimal poses are determined by Procrustes analysis. An SSM can be presented by the following formula: $\mathbf{y} = \mathbf{C}(\bar{\mathbf{x}} + \Phi\mathbf{b})$, with \mathbf{y} the matrix that holds the surface points of an instance of the model, the matrix that holds the surface points of the average surface, \mathbf{C} a rigid transformation and \mathbf{b} the

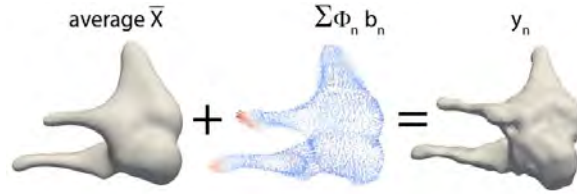


Figure 8.2: SSM approach: each target (e.g. $y_n = P100_L$) can be obtained by adding a linear combination of the principal components ($\sum \Phi_n b_n$) to the average model (\bar{x}) and applying a similarity transformation (C).

vector that holds the shape parameters. Matrix Φ holds the eigenvectors of the shape model. By adapting the shape parameters, the point coordinates will be displaced and a new, realistic surface can be formed, as shown in Figure ??.

Next, the SSM was used to locate landmarks on the individual ossicle surfaces, as shown in Figure ??. These allow us to present important measures and compare these to values from the literature. Landmark coordinates were acquired by manually annotating the points on the average of the SSM and transforming them to the individual middle-ears using the deformation function for each target. For a subset of landmarks (Um, ILP, MAP, ISP, MLP, and IMJcp), a further local optimization was performed using a geometric construction (based on the mapping of landmarks of the average shape). Three axes were defined by the original transformed landmarks: the ISP-MAP axis, IH-ILP axis, and the MH-Um axis. The Um, ILP, MAP and ISP landmarks were defined on their respective axis by projecting the surface points onto the axis and calculating the farthest surface point on the axis. MLP was defined as the farthest point from the MH-Um axis. IMJcp was defined as the center of gravity of the IMJip-IH-MH triangle. The optimized landmarks were sought within a radius of $0.5mm$ of the transformed annotated landmarks. The optimization was performed one time.

Landmarks were then used to calculate relevant ossicle features which can be compared to literature:

- The manubrium length (Um-MLP) and neck-head distance (MLP-MH) of the malleus and its enclosing angle (Um-MLP-MH);
- the short (ISP-IH) and long (ILP-IH) process lengths as well as the distance from ISP to ILP and the angle between short and long process of the incus (ILP-IH-ISP); It should be noted that the short and long process length are here defined as the distance measured till the incus head, and not till the IM joint as in the literature. The reason for this is that the IM joint was not visible in our segmentation.
- other length definitions given by ?: Um-IMJip, ILP-IMJip, and the enclosing angle (approximately the angle between manubrium and incus long process).
- Important measure is the classic lever arm ratio [?]. Here defined as the ratio between the perpendicular distance from Um to the anatomical axis (l1,Um-AnAx) and from ILP to the anatomical axis (l2,ILP-AnAx). The anatomical axis is defined by MAP-ISP. This ratio was determined using the same technique as in ?.

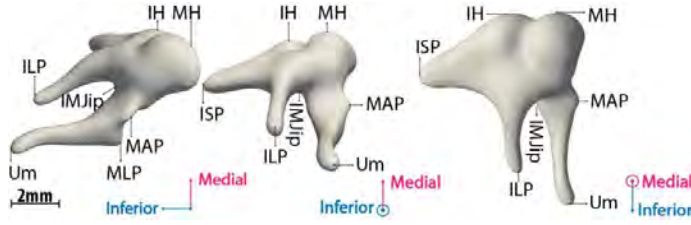


Figure 8.3: Landmarks used in this study to compare to literature data (shown on mean of SSM): (Um) umbo or inferior tip of the malleus; (ILP) lenticular process of the incus; (MAP) anterior process of the malleus; (ISP) short process of the incus; (MLP) lateral process of the malleus; (MH) malleus head (caput malleus); (IH) incus head; (IMJip) incudomalleolarincudomalleolar joint, inferior point..

- Face breadth is measured on CT scans as the distance between left and right intertragic notch, which is the notch between the tragus and antitragus, situated above the lobule of the auricle. This distance is chosen as a measure of face breadth because it, in contrast to the pinna or lobule, was distinguishable on all the scans (by using CBCT, not the whole cranium is visible).

Correspondence quality was assessed by calculating the inter- and intra-observer error. To this end, landmark points were manually annotated by three observers: all landmarks were identified on the average surface of the SSM and ten instances of the middle ear. For each surface and each landmark, the error was calculated as the distance between the manually annotated points and their mean. The calculations were repeated after locally optimizing the landmark locations.

The full 3D representation of the geometrical model also allows us to calculate the volume and the principal moment of inertia of the incudomalleolar complex (PMI). A homogeneous ossicle density (2250kg/m^3) [??] was assumed. Next, the principal moments of inertia (PMI) were calculated. Therefore, all surface models need to be filled with tetrahedral elements (tetgen, [?]). Center of mass was chosen as origin. For each tetrahedral element, the inertia matrix was calculated (with mass of tetrahedral element k and the perpendicular distance from axis (x, y, z) to the center of element k). Next, the overall inertia matrix $I_{x_i x_j, k} = m_k d_{x_i, k} d_{x_j, k}$ was calculated, with m_k the mass of tetrahedral element k and $d_{x_i, k}$ the perpendicular distance from axis x_i to the center of element k . Next, the overall inertia matrix was calculated by taking the sum of all k elements. Eigenvalues of this matrix were the PMI. A custom-made MATLAB script was used for these calculations. These anatomical features are summarized in Table ??.

A multiple linear regression was performed between the principal component weights and the features of each surface, capturing the relationship between them [?]. The regression matrix could be used to visualize the influence of a specific feature on the principal component weights, and thus on the 3D shape of the middle ear. The variation of a specific feature was represented by a deformation vector. By scaling this vector, the underlying correlation between feature and shape could be visualized, as shown in Figure ??.

In order to study the effect of the principal components these anatomical features are also shown for the first 6 principal components in Table ??. Finally, a Kolmogorov-Smirnov and Shapiro Wilk test for normality was applied, showing that the data is normally distributed. Such that the Pearson correlation had to be used. This

correlation and significance level between the measured values was calculated, corrected with a Bonferroni factor of 136, as shown in Table ???. We divided lengths by volume^{1/3} and moments of inertia by total mass and volume^{2/3}. As such, data is presented in a dimensionless way. This is done because the volume is significantly correlated with most lengths and strongly correlated with PMI, and as such, we can study correlation with the shape instead of absolute volume.

8.2.4 Quantitative data of anatomical features

Next, landmarks are used to obtain quantitative data of anatomical features. Therefore Intra- and inter-observer errors are calculated. One observer indicated all landmarks on 5 individual surfaces and did this three times. For each landmark on each surface, the distance between the three trials and the average of their location was calculated and averaged over the five surfaces. The inter observer error thus gives an indication of the error one can expect over multiple selection trials for a single observer.

Next, this error is compared with the variation that can be expected for landmarks obtained via the SSM method described in the previous section. One observer indicated all landmarks on the average and did this three times. These landmarks were then used in the geometric construction of the landmarks for five individual surfaces. Again, for each landmark on each surface, the distance between the three trials and the average of their location was calculated and averaged over the five surfaces.

A similar approach was followed for the evaluation of the inter-observer error (three observers, 10 individual surfaces) and comparison with the variance that can be expected for the landmarks via the SSM method.

8.3 Results

8.3.1 Statistical shape model

The 123 separate surface models acquired from CT data look noisy even after smoothing (e.g. Figure ??). This is caused by the limited resolution of $150\mu m$ (1/30 of manubrium length) and the poor SNR compared to μCT . Nevertheless, combining data of 123 healthy ears in an average model (Figure ??) removes this random noise and results in a smooth average model. The principal components (PC) or eigen-shapes added to this average model show the variation present in our dataset and by extension in the human middle ear (Figure ??). An advantage of the decomposition in PCs is that the first PCs explain most variation in data (Figure ??). The principal components are linearly uncorrelated shape variations and do not coincide with single anatomical variations per se. This is shown in Figure ?? and in Table ??. Some features, such as PMI_{2,3} are mainly described by a single PC, while other anatomical variations, such as Um-IMJip and ILP-IMJip are described by multiple principle components. Nevertheless, a more qualitative explanation of variations within these eigenshapes (shown in Figure ??) can be given:

PC1: 30% of the variation in our population. Mostly scaling of IM complex. Indicated by larger variation (stdev/mean) for lengths, volume and PMI in Table ?? and smaller variations in angles. Also, short process of incus seems to be affected.

PC2: 18%, mostly the angle between manubrium and long process of incus (around lateral medial axis). Indicated by larger variation of Um-IMJip-ILP in Table ??.

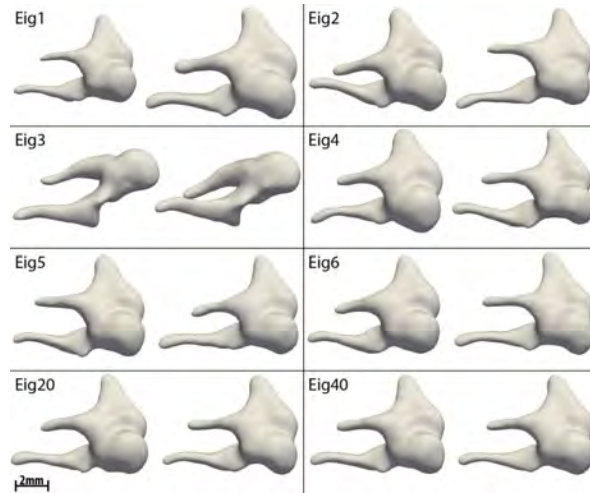


Figure 8.4: Selected principal components of the middle ear SSM. For each eigenshape $Eig_i = 1, 2, 3, 4, 5, 6, 20$ and 40 , the average $- 3 \cdot stdev_i PC_i$ (left) and average $+ 3 \cdot stdev_i PC_i$ (right) are shown.

Also small effect on lever arm ratio (2% of 1.34 in Table ??), PMI1 and curvature of manubrium (not shown).

PC3: 7.9%, mostly angle between manubrium and long process of incus (around anterior-posterior axis). Also angle between manubrium and malleus neck.

PC4: 5.6%, mostly change of manubrium shape. Also thickness of malleus head and incus short process.

PC5: 4.1%, manubrium shape and incus long process length result in large variation for Um-IMJip-ILP (Table ??).

PC6: 3.6%, incus short process shape

PC10: 1.6%, variation tends to be much smaller, incus long process (not shown)

PC20: 0.64%, small changes in thickness of incus long process and manubrium

PC22: 0.54%; **PC37:** 0.20%; **PC40:** 0.18%, tiny variation, mostly surface perturbations.

PC1-22 capture 90% of the total variation, and PC1-37 95%. The higher PCs (41-122) explain much smaller variation (combined contribution of them is less than 4%) in the population. These variations can for instance be originating from noise. The effect of leaving out higher order PCs is shown in Figure ??.

8.3.2 Anatomical features

The Intra- and inter-observer errors were calculated as described in section 2.4. The maximum intra-observer error (mean \pm stdev) was found for MH ($0.12 \pm 0.04mm$) and IH ($0.14 \pm 0.05mm$), with an average of $0.08 \pm 0.03mm$. Next, this error is compared with the variation that can be expected for landmarks obtained via the

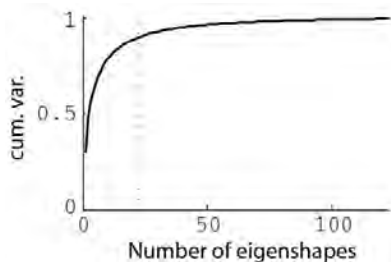


Figure 8.5: Compactness of the model: the amount of eigenshapes / PCs needed to explain the fraction of total variation in the entire middle ear population used in this study. (cum. var. = cumulative variation)

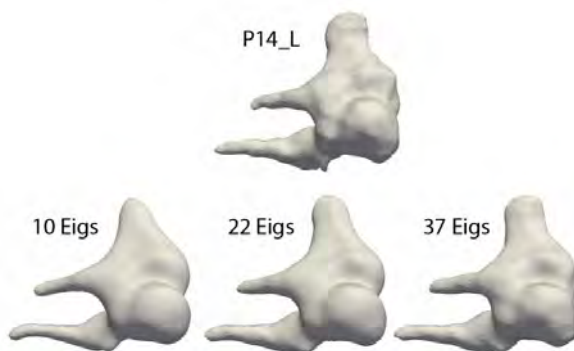


Figure 8.6: Compactness of the model shown for P14_L: effect of leaving out higher order eigenshapes (10 Eigs: PC1-10, 80% variation all models, 22 Eigs PC1-22 90%, 37 Eigs: PC1-37,95%).

Table 8.1: Measures for important IM features as indicated in Figure ??, 'average all data' is the average of 123 Patients and the relative stdev. Average model is created by SSM. PC1-6 is (average model + 3 stdev_i - (average model - 3stdev_i))/6/average model.

	average - all data (N=123)	average model	PC1	PC2	PC3	PC4	PC5	PC6
Um-MLP (mm)	4.53	4.49	4%	0%	1%	2%	0%	0%
MH-MLP (mm)	4.89	4.87	3%	1%	0%	2%	1%	0%
Um-MLP-MH (deg)	118	118	0%	1%	1%	2%	2%	1%
ISP-ILP (mm)	5.68	5.67	4%	2%	1%	0%	1%	1%
IH-ISP (mm)	4.37	4.32	8%	4%	0%	1%	1%	2%
ILP-IH-ISP (deg)	59.5	59.9	6%	0%	1%	0%	2%	2%
Um-IMJip (mm)	4.91	4.88	7%	4%	1%	1%	2%	2%
ILP-IMJip (mm)	3.27	3.21	9%	4%	1%	2%	3%	2%
UM-IMJip-ILP (deg)	37.8	37.0	19%	1%	2%	2%	10%	1%
l1=Um-AnAx (mm)	4.50	4.42	6%	3%	1%	2%	1%	1%
l2=ILP-AnAx (mm)	3.40	3.31	9%	3%	1%	3%	3%	1%
Ratio	1.33	1.33	9%	0%	2%	0%	4%	1%
Volume (mm3)	28.8	28.4	14%	12%	3%	3%	1%	2%
PMI1 (mg mm2)	123	119	23%	22%	8%	4%	4%	0%
PMI2 (mg mm2)	173	164	23%	22%	1%	0%	1%	1%
PMI3 (mg mm2)	256	245	22%	22%	4%	2%	1%	0%

SSM method described in Section ?? . As such a lower error was obtained for all points (average of $0.06 \pm 0.02mm$), except for MH ($0.17 \pm 0.04mm$) and IH ($0.20 \pm 0.02mm$). A similar approach was followed for the evaluation of the inter-observer error and comparison with the variance that can be expected for the landmarks via the SSM method. The maximum inter-observer errors were also for MH and IH ($0.25 \pm 0.07mm$ and $0.24 \pm 0.06mm$), with an average of $0.11 \pm 0.05mm$ (mean \pm stdev between). The SSM landmark method improved the average error for all landmarks (average = $0.07 \pm 0.02mm$, IH = $0.23 \pm 0.02mm$ and MH = $0.18 \pm 0.02mm$).

In Table ??, an overview of measures for important anatomical features is given and compared to values from the literature values. Relative standard deviation is about 7% for most lengths (also see Table ??). Exception to this is the larger variation for the angle between manubrium and long process of incus (19%), for volume 14% and for PMI around 23%. As a comparison, the total variation in face breadth is only 4%. Dimensionless values show smaller variation. For PMI1, PMI2 and PMI3 we found (mean value \pm stdev (stdev/mean)) of $0.201 \pm 0.013(6\%)$, $0.284 \pm 0.028(10\%)$ and $0.42 \pm 0.029(7\%)$. As a total mass we found $64.7 \pm 8.9mg$ by using uniform density of $2250kg/m^3$.

8.3.3 Correlations

Finally, the dimensionless features are used to find correlation in data, by using the Pearson correlation coefficient. In Figure ?? the correlations of these features are compared to the entire shape. By using the dimensionless data, very high correlation between PMI and volume (90% and up) and significant correlation between lengths of the malleus and PMI and volume (40%-60%) due to scaling correspondence are reduced. Indeed, moments of inertia are related with mass and thus volume and lengths. Results found for the dimensionless data are:

- PMI1 is strongly correlated with the length of incus short process.
- PMI2 and 3 are correlated with each other and with manubrium length, malleus neck-head and incus long and short process (for PMI3).
- The angle between manubrium and long process of incus (Um-IMJip-ILP) is correlated with long process (IH-ILP) and its lever arm (ILP- AnAx) but not with the manubrium (Um-MLP, Um-AnAx).
- As a result, the lever arm ratio is negatively correlated with this angle.
- The lever arm ratio is also more strongly correlated with the incus long process (IH-ILP, -0.64) than with the manubrium arm (Um-MLP, 0.20).
- Malleus angle is negatively correlated with the manubrium length.
- In general, no middle ear measures correlate significantly with the face breadth (highest correlation for ILP-IH-ISP, $r=0.2$).
- It is noteworthy that there are not so many strong correlations between anatomical features (e.g. only correlation for incus angle is IM complex opening angle (Um-IMJip-ILP)).

The correlations are also shown numerically in Table ??.

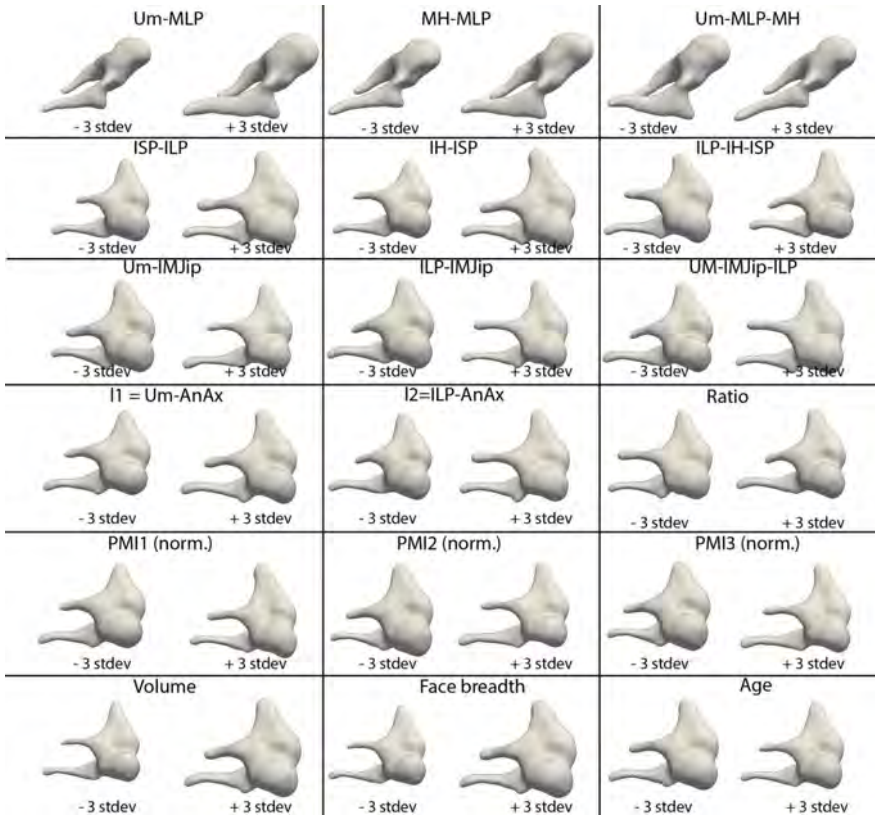


Figure 8.7: Feature plot shows the correlation between a specific feature (± 3 stdev) and the shape. PMI (norm.) is the principal component moment of inertia divided by mass and volume^{2/3}.

Table 8.2: Mean±stdev for important anatomical features, for this study and selected literature (N=number of samples). Note that angle UM-MLP-MH for Kirikae (1960), angle UM-IMJip-ILP for Ars (1977), the angles for Todd and Creighton (2013) and Quan (2014) were not given in original papers and were here calculated by assuming uncorrelated results for propagation of errors. As a result the actual stdev in their measurements would be lower. Also note that there is a difference in the definition for these measurements in our case and in literature, as mentioned earlier in 2.3.

	?	?	?	?	?	?	?	?	?
	(N=123)	(N=6)	(N=1315)	(N=200)	(N=1)	(N=20)	(N=3)	(N=41)	(N=43)
Um-MLP (mm)	4.53±0.33	4.98±0.39	4.51±0.08			4.70±0.45		4.8±0.4	4.94±0.31
MH-MLP (mm)	4.89±0.23	4.74±0.29	5.0±0.1			4.85±0.29		4.9±0.3	
Um-MLP-MH (deg)	117.5±5.8	-	120.8±3.9					111±14	
ISP-ILP (mm)	5.68±0.38	5.73±0.16	5.99±0.08			6.12±0.43		5.9±0.4	6.18±0.34
IH-ISP (mm)	4.37±0.37	5.35±0.21	4.81±0.07			4.88±0.47		5.0±0.3	5.07±0.37
ILP-IH-ISP (deg)	59.4±3.5	-	58.7±1.0					73±6	60±4.9
Um-IMJip (mm)	4.91±0.32	4.68±0.34	4.65±0.09	4.5±0.5					
ILP-IMJip (mm)	3.27±0.31	3.19±0.21		3.1±0.5					
UM-IMJip-ILP (deg)	37.8±7.0	35.3±5.4		29±14					
I1=Um-AnAx (mm)	4.50±0.28	4.47±0.30							
I2=ILP-AnAx (mm)	3.40±0.29	3.45±0.15							
Lever arm atio	1.33±0.12	1.30±0.11							
Volume (mm ³)	28.8±4.0	26.7±2.4							27.6±4.5
PMI1 (mg mm ²)	123±28	114±10			97.6				133±19
PMI2 (mg mm ²)	173±39	163±32			165.0				175±21
PMI3 (mg mm ²)	256±56	237±32			217.4				259±34
Face breadth (mm)	130.1±5.6								

Table 8.3: Correlation between dimensionless anatomical features. Underlined values have a significance smaller than 0.05/136, bold values have a significance of 0.001/136

Um-MLP	1.00	Um-MLP	1.00	Um-MLP-MH	1.00	IH-ILP	1.00	IH-ISP	1.00	ILP-IH-ISP	1.00	Um-IMJip	1.00	ILP-IMJip	1.00	Um-IMJip-ILP	1.00	Um-AnAx	1.00	ILP-AnAx	1.00	ratio	1.00	volume	1.00	PMI1	1.00	PMI2	1.00	PMI3	1.00	Head diameter	1.00
MH-MLP	0.13	MH-MLP	1.00	Um-MLP-MH	1.00	IH-ILP	1.00	IH-ISP	1.00	ILP-IH-ISP	1.00	Um-IMJip	1.00	ILP-IMJip	1.00	Um-IMJip-ILP	1.00	Um-AnAx	1.00	ILP-AnAx	1.00	ratio	1.00	volume	1.00	PMI1	1.00	PMI2	1.00	PMI3	1.00	Head diameter	1.00
Um-MLP-MH	-0.37	Um-MLP-MH	1.00	Um-MLP-MH	1.00	IH-ILP	1.00	IH-ISP	1.00	ILP-IH-ISP	1.00	Um-IMJip	1.00	ILP-IMJip	1.00	Um-IMJip-ILP	1.00	Um-AnAx	1.00	ILP-AnAx	1.00	ratio	1.00	volume	1.00	PMI1	1.00	PMI2	1.00	PMI3	1.00	Head diameter	1.00
IH-ILP	0.17	IH-ILP	0.43	Um-MLP-MH	-0.08	IH-ILP	1.00	IH-ISP	1.00	ILP-IH-ISP	1.00	Um-IMJip	1.00	ILP-IMJip	1.00	Um-IMJip-ILP	1.00	Um-AnAx	1.00	ILP-AnAx	1.00	ratio	1.00	volume	1.00	PMI1	1.00	PMI2	1.00	PMI3	1.00	Head diameter	1.00
IH-ISP	-0.02	IH-ISP	0.18	Um-MLP-MH	-0.02	IH-ILP	0.33	IH-ISP	1.00	ILP-IH-ISP	1.00	Um-IMJip	1.00	ILP-IMJip	1.00	Um-IMJip-ILP	1.00	Um-AnAx	1.00	ILP-AnAx	1.00	ratio	1.00	volume	1.00	PMI1	1.00	PMI2	1.00	PMI3	1.00	Head diameter	1.00
ILP-IH-ISP	-0.14	ILP-IH-ISP	0.00	Um-MLP-MH	0.19	IH-ILP	-0.10	IH-ISP	0.00	ILP-IH-ISP	1.00	Um-IMJip	1.00	ILP-IMJip	1.00	Um-IMJip-ILP	1.00	Um-AnAx	1.00	ILP-AnAx	1.00	ratio	1.00	volume	1.00	PMI1	1.00	PMI2	1.00	PMI3	1.00	Head diameter	1.00
Um-IMJip	0.53	Um-IMJip	0.34	Um-MLP-MH	0.36	IH-ILP	0.25	IH-ISP	-0.01	ILP-IH-ISP	-0.01	Um-IMJip	1.00	ILP-IMJip	1.00	Um-IMJip-ILP	1.00	Um-AnAx	1.00	ILP-AnAx	1.00	ratio	1.00	volume	1.00	PMI1	1.00	PMI2	1.00	PMI3	1.00	Head diameter	1.00
ILP-IMJip	0.21	ILP-IMJip	0.34	Um-MLP-MH	-0.07	IH-ILP	0.88	IH-ISP	0.26	ILP-IH-ISP	-0.19	Um-IMJip	1.00	ILP-IMJip	1.00	Um-IMJip-ILP	1.00	Um-AnAx	1.00	ILP-AnAx	1.00	ratio	1.00	volume	1.00	PMI1	1.00	PMI2	1.00	PMI3	1.00	Head diameter	1.00
Um-IMJip-ILP	-0.10	Um-IMJip-ILP	0.04	Um-MLP-MH	-0.29	IH-ILP	0.55	IH-ISP	0.08	ILP-IH-ISP	-0.37	Um-IMJip	1.00	ILP-IMJip	1.00	Um-IMJip-ILP	1.00	Um-AnAx	1.00	ILP-AnAx	1.00	ratio	1.00	volume	1.00	PMI1	1.00	PMI2	1.00	PMI3	1.00	Head diameter	1.00
Um-AnAx	0.56	Um-AnAx	0.42	Um-MLP-MH	0.20	IH-ILP	0.22	IH-ISP	0.10	ILP-IH-ISP	0.12	Um-IMJip	0.62	ILP-IMJip	0.19	Um-IMJip-ILP	0.30	Um-AnAx	1.00	ILP-AnAx	1.00	ratio	1.00	volume	1.00	PMI1	1.00	PMI2	1.00	PMI3	1.00	Head diameter	1.00
ILP-AnAx	0.18	ILP-AnAx	0.28	Um-MLP-MH	-0.08	IH-ILP	0.82	IH-ISP	0.03	ILP-IH-ISP	-0.02	Um-IMJip	0.17	ILP-IMJip	0.86	Um-IMJip-ILP	0.72	Um-AnAx	1.00	ILP-AnAx	1.00	ratio	1.00	volume	1.00	PMI1	1.00	PMI2	1.00	PMI3	1.00	Head diameter	1.00
Lever arm ratio	0.20	Lever arm ratio	0.03	Um-MLP-MH	0.22	IH-ILP	-0.64	IH-ISP	0.05	ILP-IH-ISP	0.11	Um-IMJip	0.25	ILP-IMJip	-0.69	Um-IMJip-ILP	-0.88	Um-AnAx	1.00	ILP-AnAx	1.00	ratio	1.00	volume	1.00	PMI1	1.00	PMI2	1.00	PMI3	1.00	Head diameter	1.00
Volume	-0.14	Volume	-0.51	Um-MLP-MH	-0.19	IH-ILP	-0.24	IH-ISP	0.03	ILP-IH-ISP	-0.10	Um-IMJip	0.41	ILP-IMJip	0.27	Um-IMJip-ILP	-0.08	Um-AnAx	1.00	ILP-AnAx	1.00	ratio	1.00	volume	1.00	PMI1	1.00	PMI2	1.00	PMI3	1.00	Head diameter	1.00
PMI1	0.03	PMI1	0.30	Um-MLP-MH	0.01	IH-ILP	0.32	IH-ISP	0.75	ILP-IH-ISP	-0.05	Um-IMJip	0.07	ILP-IMJip	0.32	Um-IMJip-ILP	0.12	Um-AnAx	1.00	ILP-AnAx	1.00	ratio	1.00	volume	1.00	PMI1	1.00	PMI2	1.00	PMI3	1.00	Head diameter	1.00
PMI2	0.59	PMI2	0.36	Um-MLP-MH	-0.02	IH-ILP	0.29	IH-ISP	-0.03	ILP-IH-ISP	-0.03	Um-IMJip	0.69	ILP-IMJip	0.31	Um-IMJip-ILP	-0.05	Um-AnAx	1.00	ILP-AnAx	1.00	ratio	1.00	volume	1.00	PMI1	1.00	PMI2	1.00	PMI3	1.00	Head diameter	1.00
PMI3	0.51	PMI3	0.36	Um-MLP-MH	-0.07	IH-ILP	0.40	IH-ISP	0.34	ILP-IH-ISP	-0.06	Um-IMJip	0.67	ILP-IMJip	0.39	Um-IMJip-ILP	-0.04	Um-AnAx	1.00	ILP-AnAx	1.00	ratio	1.00	volume	1.00	PMI1	1.00	PMI2	1.00	PMI3	1.00	Head diameter	1.00
Face Breadth	0.03	Face Breadth	0.10	Um-MLP-MH	-0.06	IH-ILP	0.16	IH-ISP	0.17	ILP-IH-ISP	0.20	Um-IMJip	0.03	ILP-IMJip	0.11	Um-IMJip-ILP	0.05	Um-AnAx	1.00	ILP-AnAx	1.00	ratio	1.00	volume	1.00	PMI1	1.00	PMI2	1.00	PMI3	1.00	Head diameter	1.00

8.4 Discussion

8.4.1 IM complex measures

A good agreement with literature values (mean, Stdev) for mean values as well for the standard deviation was obtained. Malleus neck-head lengths show good agreement with all literature values. The manubrium is a little bit up to 9% shorter than in most studies, except for ? and ?. Incus distance from long to short process is a little bit shorter up to 8% shorter but in good agreement. The Incus short process is also up to 18% shorter than literature values. This is due to a difference in definition mentioned earlier in 2.3 of incus head in the other studies, where distance is measured till IM joint. IM joint was not visible in our segmentation so it was measured till incus head. We do have a very good agreement with lengths for lever arm ratio (l1 and l2). In general, the relative standard deviation values found in this study are is similar to those from the literature values (7% in most cases), except for ? who reports systematically smaller standard deviations.

The volumes we found are slightly higher than those reported in previous literature. Although, differentiation between bone and air is clear on CBCT, so these slightly higher values show that the dimensions of the material selection during segmentation was were not too small underestimated. This consequently suggests that the shorter lengths in this study were not caused by too low grayscale values selected during automatic segmentation. Moreover, ? showed that the effect of segmentation is small. The variation of volume shows to be around 14%. We also found values for PMI in good agreement with previous data, but because we have a statistically relevant amount, we can also report on more reliable data for statistical variation. This variation shows to be quite large (23%). A better way to present this data could be a dimensionless representation ($PMI / \text{density} / \text{volume}^{5/3}$). $\text{Volume}^{5/3}$ may seem artificial. Nevertheless, numerical variation of the power in the previous equation shows lowest variation (stdev/mean) for PMI1 for a power of 1.6 5/3.

The correlations of dimensionless measures allow us to focus on the shape. Table ?? shows that PMI1 (dimensionless) is strongly correlated (75%) with incus short process and that PMI2 and 3 are correlated with manubrium length, malleus neck-head and long process. This is in correspondence with the rotation axes reported in literature [???]. PMI1 axis is approximately situated along the inferior-superior direction (more or less Um-MAP). Moment of inertia around this axis greatly depends on the mass and length of the incus short process. PMI2 axis is approximately along the anterior-posterior direction (more or less anatomical axis). An increase of the short process, almost located on this axis, will not affect this moment of inertia ($r=-0.03$). On the other hand, increasing the length of the manubrium and malleus head will have a large effect. PMI3 is approximately along the lateral-medial direction. Effects are similar as for PMI2. The effect of a longer incus process is smaller than malleus due to the smaller mass associated with this feature.

Nevertheless the length of the incus long process will affect lever arm ratio larger than length of manubrium or malleus neck. The angle between manubrium and long process of incus has a large variation (19%, Table ??) and is also strongly correlated with long process length and not with manubrium length, and will thus affect the lever arm ratio. One could argue that a large variation in anatomical features means that it has no large effect on or disadvantage for the transfer function. Nevertheless Although it has no direct mechanical meaning, the lever arm ratio is known to have a pressure enhancing effect [?]. This is something that could be investigated with a

finite element model with a parametric geometry based on SSM.

In general, only a few anatomical features show mutual correlation. Moreover, large variations are found in the IM complex (7% for lengths, up to 19% for IM angle). This means that most anatomical variations are not strictly constrained. This is similar to the conclusion of Todd and Creighton (2013). We also found no significant correspondence between IM complex measures and the face breadth. This is similar to the non-correlation between any ossicle dimension and mastoid size [?]. Finally, we also found no correlation between age and ossicle dimension for ages between 19 and 86 years.

To conclude this discussion, we explicitly want to point out that the middle ear transfer function is not only influenced by anatomical features and inertia properties, but that the mechanical properties of the ligaments also have a major effect on this transfer function.

8.4.2 Cone beam CT

Literature data presented by ????? were obtained using optical microscopes. Weistenhofer and Hudde (1999) improved this technique by acquiring different view angles to obtain 3D information on the ossicles. The introduction of (micro)CT opened the possibility for quantitative 3D imaging. The results of ?? are based on full 3D data obtained on cadaveric temporal bones with high resolution μ CT. Although CBCT (150 μ m) has a higher resolution compared to standard clinical CT, its resolution is still inferior to (stained) micro-CT (20 μ m). In the present study, we use available clinical data of a large patient population to calculate average morphology and their variation with a high precision. As such our study is limited to 'macroscopic' (150 μ m) shape variations. To catch these 'microscopic' variations, we would need a large amount of cadaveric temporal bone scans. This amount would even be larger than in this study to catch these 'microscopic' changes.

IM joint and stapes were visible on most CBCT scans but correct segmentation would be problematic because subtle variation in grayscale values (Hounsfield unit) occur and limit the automatic segmentation at places with lower grayscale values. We chose automated segmentation, limited to the IM-complex, because of the large data set (147 ears). The absence of Hounsfield units in CBCT also implies that density and material parameters cannot be coupled to grayscale values.

Another limitation is the visibility of soft tissue. General details on ligaments and joints could be obtained from ex-vivo μ CT and histological studies (e.g. Sim and Puria 2008, de Greef 2015a this issue). Details on tympanic membrane shape and thickness could be obtained from other in-vivo measures, such as OCT [?], Moire profilometry, and real-time microscopic phase-shifting profilometry [?].

8.4.3 Statistical shape modeling

To generate an SSM, surface models, created by segmentation, are needed. Segmentation can be dependent on the operator's subjective input. The influence of the operator's manual segmentation has been quantified by ?. In their study, the standard deviation between results generated by different operators was always smaller than 1.4%. This variation is smaller than the standard deviation of the features presented here and thus will only have a marginal effect. In addition, we use a more automatic segmentation which probably decreases this subjective error caused by manual intervention even more.

Another source of subjective errors is the selection of the landmarks. In most studies, these landmarks need to be selected on each surface model or digital image (for microscopy studies). Using the SSM approach, the anatomical landmarks only need to be selected on the average model. The sensitivity and correctness of this selection is shown to be small for most points ($<50 \mu\text{m}$ for inter- and intra-observer errors). For IH and MH the error was slightly higher, around $200 \mu\text{m}$, which is still comparable to the used resolution and the obtained variability. By using the optimization routine these smaller errors ($50 \mu\text{m}$ instead of $90 \mu\text{m}$ for most landmarks) are found. The effect is largest for the inter-observer error. Important to reduce these operator-induced errors is to provide a priori guidelines.

A major advantage of SSM is the reduction of parameters to describe shape variation. Here the higher PCs explain smaller shape variation from the average (e.g. PC 41-122 less than 4%). Smaller shape variation does however not directly mean smaller influence on mechanical behavior. This would only be the case if the mechanics act as a linear function. Higher PCs (>40) represent tiny variations, but could also have a non-negligible effect, especially when multiple PCs have an influence on the same small region. One could also do parameter studies of the shape without using SSM (e.g. ?) but the advantage of using SSM, however, is that one does not have to make a priori assumptions on the shape variations. Indeed, the shape variations are captured before placing the landmarks, necessary to obtain classic anatomical information. E.g. the angle between malleus and incus change without other geometry variations: in table 3 we see that this variation is correlated with other changes. With SSM one could study parameter variation in a more natural way. Another advantage of SSM is the dense correspondence between different shapes, so that the relation between the parameters and the global shape can be visualized. This delivers not only more qualitative insight into shape variations (which is harder in the case of a 1D parameter), but also allows us to evaluate (using FE-analysis) the influence of a parameter along greater variance than that observed in the specific samples. A major advantage of SSM is that all geometrical variations can be captured without any a priori assumptions by placing landmarks [?] this issue). Indeed, the shape variations are captured before placing the landmarks, necessary to obtain classic anatomical information. A disadvantage is that SSM have difficulties to capture outliers. All shapes of SSM need to have the same topology. This will not completely be true if for instance the manubrium is broken. At least SSM will be a good framework to detect these outliers so they can be dealt with manually. Another disadvantage is the difficulty to find correspondence between rod like protuberances, such as incus long process. This is because the algorithm searches for corresponding points by casting a normal ray from the template surface to the target surface. If ILP of the template surface is longer than ILP of the target surface, no correct corresponding points will be found near the end of ILP. This problem can result in ILP being mapped to manubrium or ILP with a similar shape as ILP of the template surface. This result in the exclusion of 24 ossicles in our analysis (going from 147 healthy ears to 123 analyzed ears).

In future this approach can be used to study the influence of morphology on transfer function. First, having the 'average middle ear' model will enable us to study the 'average mechanics', without being limited to data of a single specimen which could be a special case. Next, variation and uncertainty on the geometry can be studied by doing a parametric study including the eigenshapes. For the IM complex, only 6 parameters will be needed to explain 69% of all variation, 10 for 80% of variation,

22 for 90%. In addition, a sensitivity analysis can determine the most important eigenshapes for the functioning of the ear. The eigenshapes could also be used to smooth a low resolution CT scan, as shown in Fig. 6. This will allow patient-specific modeling approach. Another possibility is to change certain features, as shown in Fig.7, to test their influence. Finally, knowing the morphometric data of the healthy ear, may be helpful for the classification of middle ear diseases.

Acknowledgments

The authors thank D. de Greef for helpful discussions and sharing data of μ CT. This research was funded by Research Foundation Flanders (FWO) (to JS) and Agency for Innovation by Science and Technology in Flanders (IWT).

Data availability

Statistical shape model is available from <https://www.uantwerpen.be/en/research-groups/bimef/downloads/statistical-shape-mo/>.

Part IV

Conclusion

Conclusion

The goal of this manuscript was to provide a methodology for improved modeling of 3D shapes with complex (i.e. not basic geometry) topologies, such as the human body. In the chapters in this thesis, the developed algorithms are discussed into detail and thoroughly tested in the described applications.

The main techniques underlying the proposed methodology are elastic surface registration and surface posture normalization. In Chapter 2, two methods for surface registration were described. They proved to score well on geometric fit and correspondences, compared to the N-ICP-A algorithm of ?. Furthermore, the proposed algorithms run about 40 times faster than Amberg's. The more similar the surfaces, the fewer iterations are needed to obtain good correspondences and a good geometric fit.

In Chapter 3, we built an SSM that is adjustable in shape by intuitive parameters. We also studied the correlations between those intuitive parameters and found strong correlations between gender and stature, and waist circumference, waist circumference and chest circumference. No correlation was observed between breast circumference and height. The most relevant features to predict the body shape of a person were height, weight and hip circumference.

Chapter 4 is about building a posture normalized SSM. This allows to study the shape variations in a database of human body shapes in slightly varying postures. The posture model can be used to normalize any shape that is brought into correspondence with this model in a fast and precise way. Shape analysis of a posture normalized population results in more shape related variations than performing the same analysis on a non-normalized population. Furthermore, the normalized SSM is a more compact representation of the population, hence less shape modes are needed to describe a certain percentage of the population.

The contribution of Chapter ?? was an automatic technique to rig an SSM, allowing to simulate a movement on a whole range of body shapes. Results have shown that this framework has lead to detailed, realistic body shapes, moving in a natural way. In Chapter ??, Chapter ?? and Chapter ??, the developed modeling techniques were used for diverse shape-related applications. Each of those chapters contains an elaborated explanation of the methods and results

SSM Benefits

Over the chapters is shown that building an SSM of a population of shapes has many benefits for both product design as shape analysis.

Product Design The described algorithms can benefit the designs of product developers. Because of the detailed and realistic models, a designer can adapt his designs to fit very closely to the body. A perfectly fitting gear leads to optimal

comfort. Furthermore, optimal fit maximizes protection while minimizing encumbrance. For example, look at safety goggles, helmets, hearing protection,... Less-than-optimal fit can result in inadequate protection or obstruct the user's ability to perform operational tasks. On the other hand, if safety equipment is uncomfortable to wear, the user will be inclined to remove the product or even stop using it.

Personalized Design SSMs are valuable tools to improve personalized design. It is possible to link a CAD design with the SSM so that the shape of the design changes along with the shape of the model. Therefore, if a person is scanned and this scan is registered by the SSM, a personalized object can quickly be manufactured for that specific person, e.g. by 3D printing. On the other hand, as 3D scanners are still expensive equipment. With an SSM it is possible to simulate a body shape from some simple measurements, such as height, weight, gender, chest circumference,.. Following this idea, a design can again be adapted to this shape for personalized design.

Sizing System An SSM is a good tool to facilitate the design of made-by-measure products, but can also be deployed to derive a new sizing system, based on the shapes that occur in the population. Shapes can be clustered based on their principal component weights. The shapes in one cluster are more similar to each other than the shapes in other clusters.

Motion Tests By adding movement to the SSM, products can be validated for a whole range of movements. This means that the SSM can be used for reachability tests, to make sure that everything is within reach for a whole range of body shapes. Furthermore, the SSM is useful for testing the aerodynamics during motion.

Shape Analysis As shown in Chapter ??, with our developed correspondence techniques an extensive shape analysis of the shape could be carried out. An SSM makes it possible to compare 3D shapes of different groups with each other, to find statistically significant differences. In addition, by linking measurements with the SSM, the relationship between those measurements and overall 3D shape could be studied.

Possible Improvements and Future Prospects

For now, all techniques, such as PCA and linear regression, were linear. The population of N shapes, each consisting of n points, is represented by a point cloud with N points in an $3n$ -dimensional space, where each point represents a shape. Therefore, this is high-dimensional data which may be difficult to interpret. The PCA approach we applied, assumes the data lies on an embedded non-linear manifold within the N -dimensional space. Possibly, nonlinear modeling techniques are better suited to describe this high-dimensional data.

The posture normalization algorithm in Chapter 4 was built using the CAESAR database, where the subjects got strict posture instructions before scanning. Therefore, the posture variation present in this dataset is rather limited. Especially in the legs area, hardly any posture variation is present. Therefore, a dataset with more posture variation would probably lead to a posture model that is able to filter out more posture

variation, making it useful for other, less strict, datasets than the CAESAR database. More research is needed to see how a posture model built from a different dataset with more posture variation could cope with larger posture variations. Another limitation of the posture normalization framework is that it uses again a linear methodology. Therefore, it can not handle large rotational posture differences, such as torso flexion and rotation of the elbow. Further research is needed to be able to cope with this type of posture differences.

The motion in Chapter ?? was simulated by linear blend skinning. This technique works good for applications such as reachability tests or aerodynamic tests, but is not good enough for modeling soft tissue deformation and muscle bulging. Therefore, it can not be applied for e.g. animation movies, where the focus is on approaching the real world. More complex modeling algorithms should be used for that. Moreover, the skeleton is created relatively to the body shape, causing the skeleton to be too close to the skin, instead of at the center, for people with high BMI. A better method would be to generate a true skeleton for every surface in the training group and add these skeletons to the PCA model.

In Chapter ??, we talked about the combined SSM of the scalp and skull. For now, the two surfaces were registered separately and combined afterwards to create a combined SSM. Therefore, tangential shear between both surfaces can occur, which influences the SSM. A better way would be to register the scalp and skull together, to obtain a more accurate SSM. The problem with registering them together, is that the surfaces are relatively close to each other and one part can be mistaken for the other part. This means that the scalp can incorrectly be corresponded to the skull. Therefore, adding an extra spring force between the surfaces that keeps them together, could be a solution to this problem.

Bibliography

- 3D human model (2017). 3D HUMAN MODEL Antropometric Design & Validation Tool. <https://www.3dhumanmodel.com/>.
- 3D Scan Store (2016). 3D Scan Store - head scans - full body scans - Tutorials and HDRI's for 3D artists. <http://www.3dscanstore.com/>.
- Allen, B., Curless, B., and Popović, Z. (2003). The space of human body shapes. *ACM Transactions on Graphics*, 22(3):587.
- Alomari, R. S., Corso, J. J., Chaudhary, V., and Dhillon, G. (2014). Lumbar spine disc herniation diagnosis with a joint shape model. *Lecture Notes in Computational Vision and Biomechanics*, 17:87–98.
- Amberg, B., Romdhani, S., Vetter, T., Amberg, B., Romdhani, S., and Vetter, T. (2007). Optimal step nNonrigid ICP algorithms. In *IEEE Conference on Computer Vision and Pattern Recognition (CVPR)*, pages 1–8. IEEE.
- Anguelov, D., Srinivasan, P., Koller, D., Thrun, S., Rodgers, J., and Davis, J. (2005). Scape. *ACM Transactions on Graphics*, 24(3):408.
- Ars, B. (1977). Surgical anatomy of the tympano-ossicular system. *Acta oto-rhino-laryngologica Belgica*, 31(1):50–68.
- Asgharpour, Z., Baumgartner, D., Willinger, R., Graw, M., and Peldschus, S. (2014). The validation and application of a finite element human head model for frontal skull fracture analysis. *Journal of the Mechanical Behavior of Biomedical Materials*, 33(1):16–23.
- Audette, M., Brooks, R., Funnell, R., Strauss, G., and Arbel, T. (2008). Piecewise affine initialized spline-based patient-specific registration of a high-resolution ear model for surgical guidance. *MICCAI Workshop on Image Guidance and Computer Assistance for Soft-Tissue Interventions*.
- Baluwala, H. Y., Malcolm, D. T., Jor, J. W., Nielsen, P. M., and Nash, M. P. (2015). Automatic landmark detection using statistical shape modelling and template matching. In *Computational Biomechanics for Medicine: New Approaches and New Applications*, pages 75–82. Springer International Publishing, Cham.
- Baran, I. and Popović, J. (2007). Automatic rigging and animation of 3D characters. *ACM Transactions on Graphics*, 26(3):72.
- Barnea, E., Mairon, R., and Ben-Shahar, O. (2016). Colour-agnostic shape-based 3D fruit detection for crop harvesting robots. *Biosystems Engineering*, 146:57–70.
- Blanc, R., Seiler, C., Székely, G., Nolte, L. P., and Reyes, M. (2012). Statistical model based shape prediction from a combination of direct observations and various surrogates: Application to orthopaedic research. *Medical Image Analysis*, 16(6):1156–1166.
- Blanchonette, P. (2010). Jack Human Modelling Tool: A Review. Technical report, Air Operations Division Defence Science and Technology Organisation.
- Blanz, V. and Vetter, T. (1999). A morphable model for the synthesis of 3D faces. In *Proceedings of the 26th annual conference on Computer graphics and interactive techniques - SIGGRAPH '99*, pages 187–194, New York, New York, USA. ACM Press.

-
- Blanz, V. and Vetter, T. (2003). 3DMM-Face recognition based on fitting a 3D morphable model. *TPAMI*, 25(9):1063–1074.
- Blender Online Community (2013). Blender - a 3D modelling and rendering package. URL: <http://www.blender.org/>.
- Borsa, J., Chu, R., Sun, J., Linton, N., and Hunter, C. (2002). Use of CT scans and treatment planning software for validation of the dose component of food irradiation protocols. *Radiation Physics and Chemistry*, 63(3-6):271–275.
- Bragança, S., Arezes, P., Carvalho, M., and Ashdown, S. (2016). Effects of Different Body Postures on Anthropometric Measures. *Advances in Ergonomics in Design: Proceedings of the AHFE 2016 International Conference on Ergonomics in Design, July 27-31, 2016, Walt Disney World®, Florida, USA*, 485:313–322.
- Bredbenner, T. L., Eliason, T. D., Francis, W. L., McFarland, J. M., Merkle, A. C., and Nicolella, D. P. (2014). Development and validation of a statistical shape modeling-based finite element model of the cervical spine under low-level multiple direction loading conditions. *Frontiers in Bioengineering and Biotechnology*, 2(November):58.
- Brunton, A., Salazar, A., Bolkart, T., and Wuhrer, S. (2014). Review of statistical shape spaces for 3D data with comparative analysis for human faces. *Computer Vision and Image Understanding*, 128:1–17.
- Bruse, J. L., McLeod, K., Biglino, G., Ntsinjana, H. N., Capelli, C., Hsia, T. Y., Sermesant, M., Pennek, X., Taylor, A. M., Schievano, S., Taylor, A., Giardini, A., Khambadkone, S., de Leval, M., Bove, E., Dorfman, A., Baker, G. H., Hlavacek, A., Migliavacca, F., Pennati, G., Dubini, G., Marsden, A., Vignon-Clementel, I., Figliola, R., and McGregor, J. (2016). A statistical shape modelling framework to extract 3D shape biomarkers from medical imaging data: Assessing arch morphology of repaired coarctation of the aorta. *BMC Medical Imaging*, 16(1):40.
- Buytaert, J., Goyens, J., De Greef, D., Aerts, P., and Dirckx, J. (2014). Volume shrinkage of bone, brain and muscle tissue in sample preparation for micro-CT and light sheet fluorescence microscopy (LSFM). *Microscopy and Microanalysis*, 20(4):1208–1217.
- Canavan, S., Liu, P., Zhang, X., and Yin, L. (2015). Landmark localization on 3D/4D range data using a shape index-based statistical shape model with global and local constraints. *Computer Vision and Image Understanding*, 139:136–148.
- Casselman, J. W., Gieraerts, K., Volders, D., Delanote, J., Mermuys, K., De Foer, B., and Swennen, G. (2013). Cone beam CT: Non-dental applications. *Jbr-Btr*, 96(6):333–353.
- Chen, Y., Liu, Z., and Zhang, Z. (2013). Tensor-based human body modeling. In *Proceedings of the IEEE Computer Society Conference on Computer Vision and Pattern Recognition*, pages 105–112. IEEE.
- Cignoni, P., Cignoni, P., Callieri, M., Callieri, M., Corsini, M., Corsini, M., Dellepiane, M., Dellepiane, M., Ganovelli, F., Ganovelli, F., Ranzuglia, G., and Ranzuglia, G. (2008). MeshLab: an Open-Source Mesh Processing Tool. In *Sixth Eurographics Italian Chapter Conference*, pages 129–136. The Eurographics Association.

Bibliography

- Claes, P., Vandermeulen, D., De Greef, S., Willems, G., and Suetens, P. (2006). Craniofacial reconstruction using a combined statistical model of face shape and soft tissue depths: Methodology and validation. *Forensic Science International*, 159(1):S147–S158.
- Cootes, T. F., Taylor, C. J., Cooper, D. H., and Graham, J. (1995). Active shape models - their training and application. *Computer Vision and Image Understanding*, 61(1):38–59.
- Corsini, M., Cignoni, P., and Scopigno, R. (2012). Efficient and flexible sampling with blue noise properties of triangular meshes. *IEEE Transactions on Visualization and Computer Graphics*, 18(6):914–924.
- Costa, C., Antonucci, F., Pallottino, F., Aguzzi, J., Sun, D. W., and Menesatti, P. (2011). Shape Analysis of Agricultural Products: A Review of Recent Research Advances and Potential Application to Computer Vision. *Food and Bioprocess Technology*, 4(5):673–692.
- Crum, W. R., **Danckaers**, F., Huysmans, T., Cotel, M. C., Natesan, S., Modo, M. M., Sijbers, J., Williams, S. C., Kapur, S., and Vernon, A. C. (2016). Chronic exposure to haloperidol and olanzapine leads to common and divergent shape changes in the rat hippocampus in the absence of grey-matter volume loss. *Psychological Medicine*, 46(15):3081–3093.
- Dahmani-Causse, M., Marx, M., Deguine, O., Fraysse, B., Lepage, B., and Escudé, B. (2011). Morphologic examination of the temporal bone by cone beam computed tomography: Comparison with multislice helical computed tomography. *European Annals of Otorhinolaryngology, Head and Neck Diseases*, 128(5):230–235.
- Dai, H., Cai, B., Song, J., and Zhang, D. (2010). Skeletal animation based on BVH motion data. In *2nd International Conference on Information Engineering and Computer Science - Proceedings, ICIECS 2010*, pages 1–4. IEEE.
- Davies, R. H., Twining, C. J., Cootes, T. F., Waterton, J. C., and Taylor, C. J. (2002). A minimum description length approach to statistical shape modeling. *IEEE Transactions on Medical Imaging*, 21(5):525–537.
- De Greef, D., Buytaert, J. A., Aerts, J. R., Van Hoorebeke, L., Dierick, M., and Dirckx, J. (2015a). Details of human middle ear morphology based on micro-CT imaging of phosphotungstic acid stained samples. *Journal of Morphology*, 276(9):1025–1046.
- De Greef, D., Goyens, J., Pintelon, I., Bogers, J.-P., Van Rompaey, V., Hamans, E., and Van de Heyning, P. (2015b). On the connection between the eardrum and the malleus: a detailed study through micro-CT and histology. In *MEMRO 2015 - 7th International Symposium on Middle Ear Mechanics in Research and Otolology*, pages 29–30.
- Decraemer, W. F., Dirckx, J. J. J., and Funnell, W. R. J. (2003). Three-Dimensional Modelling of the Middle-Ear Ossicular Chain Using a Commercial High-Resolution X-Ray CT Scanner. *JARO - Journal of the Association for Research in Otolaryngology*, 4(2):250–263.
- Decraemer, W. F., Maes, S., and Funnell, W. (2015). Finite-element modelling of the synovial fluid and contact in the incudostapedial joint. In *Memro*.

-
- Dehghannya, J., Ngadi, M., and Vigneault, C. (2010). Mathematical Modeling Procedures for Airflow, Heat and Mass Transfer During Forced Convection Cooling of Produce: A Review. *Food Engineering Reviews*, 2(4):227–243.
- Delele, M. A., Tijssens, E., Atalay, Y. T., Ho, Q. T., Ramon, H., Nicolai, B. M., and Verboven, P. (2008). Combined discrete element and CFD modelling of airflow through random stacking of horticultural products in vented boxes. *Journal of Food Engineering*, 89(1):33–41.
- Domingo, J., Ibáñez, M. V., Simó, A., Dura, E., Ayala, G., and Alemany, S. (2014). Modeling of female human body shapes for apparel design based on cross mean sets. *Expert Systems with Applications*, 41(14):6224–6234.
- Dryden, I. L. and Mardia, K. V. (2016). *Statistical Shape Analysis, with Applications in R*. John Wiley and Sons Ltd.
- Ferrari, V., Jurie, F., and Schmid, C. (2010). From images to shape models for object detection. *International Journal of Computer Vision*, 87(3):284–303.
- Fritscher, K. D., Peroni, M., Zaffino, P., Spadea, M. F., Schubert, R., and Sharp, G. (2014). Automatic segmentation of head and neck CT images for radiotherapy treatment planning using multiple atlases, statistical appearance models, and geodesic active contours. *Medical Physics*, 41(5):051910.
- Funnell, W. R. (1984). On the calculation of surface areas of objects reconstructed from serial sections. *Journal of Neuroscience Methods*, 11(3):205–210.
- Gan, R. Z., Sun, Q., Dyer, R. K., Chang, K. H., and Dormer, K. J. (2002). Three-dimensional modeling of middle ear biomechanics and its applications. *Otology and Neurotology*, 23(3):271–280.
- Gerig, R., Ihrle, S., Rösli, C., Dalbert, A., Dobrev, I., Pfiffner, F., Eiber, A., Huber, A. M., and Sim, J. H. (2015). Contribution of the incudo-malleolar joint to middle-ear sound transmission. *Hearing Research*, 327:218–226.
- Godin, C. (2011). Jack A premier human simulation tool for populating your designs with virtual people and performing human factors and ergonomic analysis. Technical report.
- Goñi, S. M., Purlis, E., and Salvadori, V. O. (2007). Three-dimensional reconstruction of irregular foodstuffs. *Journal of Food Engineering*, 82(4):536–547.
- Goñi, S. M., Purlis, E., and Salvadori, V. O. (2008). Geometry modelling of food materials from magnetic resonance imaging. *Journal of Food Engineering*, 88(4):561–567.
- Gower, J. C. (1975). Generalized procrustes analysis. *Psychometrika*, 40(1):33–51.
- Guo, Z., Zhang, Y. N., Xia, Y., Lin, Z. G., Fan, Y. Y., and Feng, D. D. (2013). Multi-pose 3D face recognition based on 2D sparse representation. *Journal of Visual Communication and Image Representation*, 24(2):117–126.
- Hamanishi, S., Murakoshi, M., Steele, C., Puria, S., and Wada, H. (2016). Effects of Maturation on Dynamic Behavior of Ear Canal Wall and Middle Ear in Neonates. In *Bioengineering Conference Annual Meeting of BED/JSME*.

- Haney, J. M., Wang, T., D'Souza, C., Jones, M. L., and Reed, M. P. (2017). Spatial and temporal patterns in sequential precision reach movements. *Proceedings of the Human Factors and Ergonomics Society*, 2017-Octob(1):929–930.
- Hasler, N., Stoll, C., Sunkel, M., Rosenhahn, B., and Seidel, H. P. (2009). A statistical model of human pose and body shape. In *Computer Graphics Forum*, volume 28, pages 337–346.
- Heimann, T. and Meinzer, H. P. (2009). Statistical shape models for 3D medical image segmentation: A review. *Medical Image Analysis*, 13(4):543–563.
- Hemilä, S., Nummela, S., and Reuter, T. (1995). What middle ear parameters tell about impedance matching and high frequency hearing. *Hearing Research*, 85(1-2):31–44.
- Ho, B.-C., Andreasen, N. C., Ziebell, S., Pierson, R., and Magnotta, V. (2011). Long-term Antipsychotic Treatment and Brain Volumes. *Archives of General Psychiatry*, 68(2):128.
- Hoffstetter, M., Schardt, F., Lenarz, T., Wacker, S., and Wintermantel, E. (2010). Parameter study on a finite element model of the middle ear. *Biomedizinische Technik*, 55(1):19–26.
- Huysmans, T., Sijbers, J., and Brigitte, V. (2010). Automatic construction of correspondences for tubular surfaces. *IEEE Transactions on Pattern Analysis and Machine Intelligence*, 32(4):636–651.
- Huysmans, T., Sijbers, J., and Verdonk, B. (2005). Parameterization of Tubular Surfaces on the Cylinder. *the Journal of Wscg*, 13:97—104.
- Huysmans, T., **Danckaers**, F., Vleugels, J., Lacko, D., De Bruyne, G., Verwulgen, S., and Sijbers, J. (2019). Multi-patch B-spline statistical shape models for CAD-compatible digital human modeling. In *Advances in Human Factors in Simulation and Modeling*, pages 179–189. Springer, Cham.
- Iqbal, S. M., Gopal, A., and Sarma, A. S. V. (2011). Volume estimation of apple fruits using image processing. In *ICIIP 2011 - Proceedings: 2011 International Conference on Image Information Processing*, pages 1–6. IEEE.
- Jacob, A., Faria, C., Cardoso, G., Reis, K., Motta, M., Meneghetti, T., Cammino, R., and Shibli, A. (2015). Evaluation of Helmet Protection during Impact of Head to Ground and Impact of an Object to Head Using Finite Element Analysis. *Journal of Safety Engineering*, 5(1):8–16.
- Jancsó, P. T., Clijmans, L., Nicolăi, B. M., and De Baerdemaeker, J. (2001). Investigation of the effect of shape on the acoustic response of 'conference' pears by finite element modelling. *Postharvest Biology and Technology*, 23(1):1–12.
- Jones, P. R. and Rioux, M. (1997). Three-dimensional Surface Anthropometry: Applications to the Human Body. *Optics and Lasers in Engineering*, 28(2):89–117.
- Kazemi, K. and Noorzadeh, N. (2014). Quantitative comparison of SPM, FSL, and brainsuite for brain MR image segmentation. *Journal of biomedical physics & engineering*, 4:13–26.

-
- Kendall, D. G. (1989). [A Survey of the Statistical Theory of Shape]: Rejoinder. *Statistical Science*, 4(2):116–120.
- Keustermans, W., Huysmans, T., **Danckaers**, F., Zarowski, A., Schmelzer, B., Sijbers, J., and Dirckx, J. (2018). High quality statistical shape modelling of the human nasal cavity and applications. *Royal Society Open Science*.
- Kim, J., Moreira, R. G., Huang, Y., and Castell-Perez, M. E. (2007). 3-D dose distributions for optimum radiation treatment planning of complex foods. *Journal of Food Engineering*, 79(1):312–321.
- Kirikae, I. (1960). *The Structure and Function of the Middle Ear*. Tokyo ; Univ. of Tokyo Press.
- Klein, K. F., Hu, J., Reed, M. P., Hoff, C. N., and Rupp, J. D. (2015). Development and validation of statistical models of femur geometry for use with parametric finite element models. *Annals of Biomedical Engineering*, 43(10):2503–2514.
- Knapik, J., Reynolds, K., and Harman, E. (2004). Soldier load carriage: historical, physiological, biomechanical, and medical aspects. *Military medicine*, 169(1):45–56.
- Koike, T., Wada, H., and Kobayashi, T. (2002). Modeling of the human middle ear using the finite-element method. *The Journal of the Acoustical Society of America*, 111(3):1306–1317.
- Lacko, D., Huysmans, T., Parizel, P. M., De Bruyne, G., Verwulgen, S., Van Hulle, M. M., and Sijbers, J. (2015). Evaluation of an anthropometric shape model of the human scalp. *Applied Ergonomics*, 48:70–85.
- Lane, J. I., Witte, R. J., Driscoll, C. L., Camp, J. J., and Robb, R. A. (2004). Imaging microscopy of the middle and inner ear. Part I: CT microscopy. *Clinical Anatomy*, 17(8):607–612.
- Lane, J. I., Witte, R. J., Henson, O. W., Driscoll, C. L., Camp, J., and Robb, R. A. (2005). Imaging microscopy of the middle and inner ear - Part II: MR microscopy. *Clinical Anatomy*, 18(6):409–415.
- Lee, C.-F., Chen, P.-R., Lee, W.-J., Chen, J.-H., and Liu, T.-C. (2006). Three-Dimensional Reconstruction and Modeling of Middle Ear Biomechanics by High-Resolution Computed Tomography and Finite Element Analysis. *The Laryngoscope*, 116(5):711–716.
- Lei, Z., Yang, J., and Zhuang, Z. (2012). Headform and N95 filtering facepiece respirator interaction: Contact pressure simulation and validation. *Journal of Occupational and Environmental Hygiene*, 9(1):46–58.
- Lindner, C., Waring, D., Thiruvengkatachari, B., O’Brien, K., and Cootes, T. F. (2017). Adaptable landmark localisation: Applying model transfer learning to a shape model matching system. In *Lecture Notes in Computer Science (including subseries Lecture Notes in Artificial Intelligence and Lecture Notes in Bioinformatics)*, volume 10433 LNCS, pages 144–151. Springer, Cham.
- Ling, L., Hongzhen, X., Wenlin, S., and Gelin, L. (2007). Research on Visualisation of Fruits Based on Deformation. *New Zealand Journal of Agricultural Research*, 50(5):593–600.

Bibliography

- Liu, Z., Li, J., Chen, G., and Lu, G. (2014). Predicting detailed body sizes by feature parameters. *International Journal of Clothing Science and Technology*, 26(2):118–130.
- Lopes, O., Reyes, M., Escalera, S., and González, J. (2014). Spherical blurred shape model for 3-D object and pose recognition: Quantitative analysis and HCI applications in smart environments. *IEEE Transactions on Cybernetics*, 44(12):2379–2390.
- Lowe, D. G. (2004). Distinctive image features from scale-invariant keypoints. *International Journal of Computer Vision*, 60(2):91–110.
- Ma, X. and Luximon, A. (2014). 3D foot prediction method for low cost scanning. *International Journal of Industrial Ergonomics*, 44(6):866–873.
- Maes, C., Fabry, T., Keustermans, J., Smeets, D., Suetens, P., and Vandermeulen, D. (2010). Feature detection on 3D face surfaces for pose normalisation and recognition. In *C. Maes, T. Fabry, J. Keustermans, D. Smeets, P. Suetens, and D. Vandermeulen*, pages 1—6. IEEE.
- Mebatsion, H. K., Boudon, F., Godin, C., Pradal, C., Génard, M., Goz-Bac, C., and Bertin, N. (2011). A Novel Profile Based Model for Virtual Representation of Quasi-Symmetric Plant Organs. *Computers and Electronics in Agriculture*, 75(1):113–124.
- Meunier, P., Shu, C., and Xi, P. (2009). Revealing the internal structure of human variability for design purposes. In *17th World Congress on Ergonomics*.
- Moes, N. C. C. M. (2010). Digital Human Models: An Overview of Development and Applications in Product and Workplace Design. In *Proceedings of the Eight International Symposium on Tools and Methods of Competitive Engineering - TMCE 2010*, pages 73–84, Ancona, Italy.
- Mohr, A. and Gleicher, M. (2003). Building efficient, accurate character skins from examples. *ACM Transactions on Graphics*, 22(3):562.
- Moreda, G. P., Muñoz, M. A., Ruiz-Altisent, M., and Perdigones, A. (2012). Shape determination of horticultural produce using two-dimensional computer vision - A review. *Journal of Food Engineering*, 108(2):245–261.
- Motallebzadeh, H., Robert J Funnell, W., and Daniel, S. (2015). Sensitivity analyses of finite-element models of newborn ear canal and middle ear. In *International meeting of Middle-Ear Mechanics in Research and Otosurgery (MEMRO)*.
- Muhammad, G. (2015). Date fruits classification using texture descriptors and shape-size features. *Engineering Applications of Artificial Intelligence*, 37:361–367.
- Mustafa, H., Pang, T. Y., Perret-Ellena, T., and Subic, A. (2015). Finite element bicycle helmet models development. *Procedia Technology*, 20(July):91–97.
- Muyshondt, P. G., Soons, J. A., De Greef, D., Pires, F., Aerts, P., and Dirckx, J. J. (2016). A single-ossicle ear: Acoustic response and mechanical properties measured in duck. *Hearing Research*, 340:35–42.

-
- O'Connor, K. N., Cai, H., and Puria, S. (2017). The effects of varying tympanic-membrane material properties on human middle-ear sound transmission in a three-dimensional finite-element model. *The Journal of the Acoustical Society of America*, 142(5):2836–2853.
- Oliphant, T. E. (2007). Python for scientific computing. *Computing in Science and Engineering*, 9(3):10–20.
- Oßmann, S., Carus, G., Bornitz, M., M., F., and T, Z. (2015). On the influence of anatomical variations on METF - theoretical investigations using a finite element model. In *Memro*.
- Otake, Y., Carneal, C. M., Lucas, B. C., Thawait, G., Carrino, J. A., Corner, B. D., Carboni, M. G., Decristofano, B. S., Maffeo, M. A., Merkle, A. C., and Armand, M. (2015). Supervised learning of anatomical structures using demographic and anthropometric information. In *Advances in Intelligent Systems and Computing*, volume 318, pages 225–240. Springer, Cham.
- Park, B.-K., Lumeng, J. C., Lumeng, C. N., Ebert, S. M., and Reed, M. P. (2015). Child body shape measurement using depth cameras and a statistical body shape model. *Ergonomics*, 58(2):301–309.
- Park, B. K. and Reed, M. P. (2015). Parametric body shape model of standing children aged 3–11 years. *Ergonomics*, 58(10):1714–1725.
- Peng, Y. and Lu, R. (2006). Improving apple fruit firmness predictions by effective correction of multispectral scattering images. *Postharvest Biology and Technology*, 41(3):266–274.
- Pintar, F. A., Philippens, M. M. G. M., Zhang, J., and Yoganandan, N. (2013). Methodology to determine skull bone and brain responses from ballistic helmet-to-head contact loading using experiments and finite element analysis. *Medical Engineering and Physics*, 35(11):1682–1687.
- Pishchulin, L., Wuhrer, S., Helten, T., Theobalt, C., and Schiele, B. (2017). Building statistical shape spaces for 3D human modeling. *Pattern Recognition*, 67:276–286.
- Ponce, E., Ponce, D., and Andresen, M. (2014). Modeling heading in adult soccer players. *IEEE Computer Graphics and Applications*, 34(5):8–13.
- Qi, L., Funnell, W. R. J., and Daniel, S. J. (2008). A nonlinear finite-element model of the newborn middle ear. *The Journal of the Acoustical Society of America*, 124(1):337–347.
- Quam, R. M., Coleman, M. N., and Martínez, I. (2014). Evolution of the auditory ossicles in extant hominids: Metric variation in African apes and humans. *Journal of Anatomy*, 225(2):167–196.
- Rakun, J., Stajniko, D., Berk, P., Lakota, M., Zazula, D., and Others (2012). Detecting natural objects by means of 2D and 3D shape analysis. *Actual Tasks on Agricultural Engineering: Proceedings of the 40. International Symposium on Agricultural Engineering, Opatija, Croatia, 21-24 February 2012*, pages 345–354.

Bibliography

- Reed, M., Park, B.-K. D., and Corner, B. (2016). Predicting seated body shape from standing body shape. In *4th International Digital Human Modeling Conference*, pages 1–5, Montreal, Canada.
- Robinette, K., Daanen, H., and Paquet, E. (1999). The CAESAR project: a 3-D surface anthropometry survey. In *Second International Conference on 3-D Digital Imaging and Modeling (Cat. No.PR00062)*, pages 380–386. IEEE Comput. Soc.
- Rogge, S., Defraeye, T., Herremans, E., Verboven, P., and Nicolaï, B. M. (2015). A 3D contour based geometrical model generator for complex-shaped horticultural products. *Journal of Food Engineering*, 157:24–32.
- Rosowski, J. J., Chien, W., Ravicz, M. E., and Merchant, S. N. (2007). Testing a method for quantifying the output of implantable middle ear hearing devices. *Audiology and Neurotology*, 12(4):265–276.
- Saito, A., Nawano, S., and Shimizu, A. (2016). Joint optimization of segmentation and shape prior from level-set-based statistical shape model, and its application to the automated segmentation of abdominal organs. *Medical Image Analysis*, 28:46–65.
- Sayinci, B., Kara, M., Ercicsli, S., Duyar, Ö., and Ertürk, Y. (2015). Elliptic Fourier analysis for shape distinction of Turkish hazelnut cultivars. *Erwerbs-Obstbau*, 57(1):1.
- Scheerlinck, N., Marquenie, D., Jancsó, P. T., Verboven, P., Moles, C. G., Banga, J. R., and Nicolaï, B. M. (2004). A model-based approach to develop periodic thermal treatments for surface decontamination of strawberries. *Postharvest Biology and Technology*, 34(1):39–52.
- Schroeder, W., Martin, K., and Lorensen, B. (1997). *An Object-Oriented Approach To 3D Graphics*, volume 429. Kitware.
- Si, H. (2010). A quality tetrahedral mesh generator and a 3d delaunay triangulator.
- Sim, J. H. and Puria, S. (2008). Soft tissue morphometry of the malleus-incus complex from micro-CT imaging. *JARO - Journal of the Association for Research in Otolaryngology*, 9(1):5–21.
- Sim, J. H., Puria, S., and Steele, C. (2007). Calculation of inertial properties of the malleus-incus complex from micro-CT imaging. *Journal of Mechanics of Materials and Structures*, 2(8):1515–1524.
- Smoger, L. M., Shelburne, K. B., Cyr, A. J., Rullkoetter, P. J., and Laz, P. J. (2017). Statistical shape modeling predicts patellar bone geometry to enable stereo-radiographic kinematic tracking. *Journal of Biomechanics*, 58:187–194.
- Soons, J., **Danckaers**, F., Huysmans, T., Sijbers, J., Casselamn, J. W., and Dirckx, J. J. J. (2015). Statistical Shape Modeling of the Incudomalleolar Complex using Micro-CT and Clinical Cone-beam CT. In *MEMRO: 7th International Symposium on Middle Ear Mechanics in Research and Otology*, Aalborg, Denmark.
- Soons, J. A., **Danckaers**, F., Keustermans, W., Huysmans, T., Sijbers, J., Casselman, J. W., and Dirckx, J. J. (2016). 3D morphometric analysis of the human incudomalleolar complex using clinical cone-beam CT. *Hearing Research*, 340:79–88.

-
- Stajanko, D., Rozman, Č., Pavlovič, M., Beber, M., and Zadavec, P. (2013). Modeling of 'Gala' apple fruits diameter for improving the accuracy of early yield prediction. *Scientia Horticulturae*, 160:306–312.
- Stanković, K., **Danckaers**, F., Booth, B. G., Burg, F., Duerinck, S., Sijbers, J., and Huysmans, T. (2016). Foot Abnormality Mapping using Statistical Shape Modelling. In *Proceedings of the 7th International Conference on 3D Body Scanning Technologies, Lugano, Switzerland, 30 Nov.-1 Dec. 2016*, pages 70–79, Ascona, Switzerland.
- Su, Z. (2011). *Statistical Shape Modelling : Automatic Shape Model Building*. PhD thesis, University College London.
- T., H. and J., S. (2009). Method for Mapping Tubular Surfaces to a Cylinder.
- Danckaers**, F., Huysmans, T., Halleman, A., De Bruyne, G., Truijen, S., and Sijbers, J. (2018a). Full Body Statistical Shape Modeling with Posture Normalization. In *Advances in Intelligent Systems and Computing*, volume 591, pages 437–448. Springer, Cham.
- Danckaers**, F., Huysmans, T., Halleman, A., De Bruyne, G., Truijen, S., and Sijbers, J. (2018b). Posture normalization of 3D body scans. *Ergonomics*.
- Danckaers**, F., Huysmans, T., Lacko, D., Ledda, A., Verwulgent, S., Van Dongen, S., and Sijbers, J. (2014). Correspondence preserving elastic surface registration with shape model prior. In *Proceedings - International Conference on Pattern Recognition*, pages 2143–2148, Stockholm, Sweden. IEEE.
- Danckaers**, F., Huysmans, T., Lacko, D., and Sijbers, J. (2015a). Evaluation of 3D Body Shape Predictions Based on Features. In *Proceedings of the 6th International Conference on 3D Body Scanning Technologies, Lugano, Switzerland, 27-28 October 2015*, pages 258–265, Ascona, Switzerland.
- Danckaers**, F., Huysmans, T., Rogge, S., Van Dael, M., Verboven, P., Nicolai, B., and Sijbers, J. (2016a). Building a Statistical Shape Model of the Interior and Exterior of the Bell Pepper. In *30th Targeted Technologies for Sustainable Food Systems (EFFoST) International Conference*, volume 28-30 Nove, Vienna, Austria.
- Danckaers**, F., Huysmans, T., Van Dael, M., Verboven, P., Nicolai, B., and Sijbers, J. (2015b). Building a Statistical Shape Model of the Apple from Corresponded Surfaces. *Chemical Engineering Transactions*, 44:49–54.
- Danckaers**, F., Huysmans, T., Van Dael, M., Verboven, P., Nicolai, B., and Sijbers, J. (2016b). Building Statistical Shape Models of Vegetables and Fruit. In *National Symposium for Applied Biological Sciences (NSABS)*.
- Danckaers**, F., Huysmans, T., Van Dael, M., Verboven, P., Nicolai, B., and Sijbers, J. (2017). Building 3D Statistical Shape Models of Horticultural Products. *Food and Bioprocess Technology*, 10(11):2100–2112.
- Danckaers**, F., Lacko, D., Verwulgen, S., De Bruyne, G., Huysmans, T., and Sijbers, J. (2018c). A Combined Statistical Shape Model of the Scalp and Skull of the Human Head. In *Advances in Intelligent Systems and Computing*, volume 591, pages 538–548. Springer, Cham.

Bibliography

- Danckaers**, F., Scataglini, S., Haelterman, R., Van Tiggelen, D., Huysmans, T., and Sijbers, J. (2019). Automatic generation of statistical shape models in motion. In *Advances in Human Factors in Simulation and Modeling*, pages 170–178. Springer, Cham.
- Tinard, V., Deck, C., and Willinger, R. (2012). New methodology for improvement of helmet performances during impacts with regards to biomechanical criteria. *Materials and Design*, 37:79–88.
- Tornincasa, S., Bonisoli, E., and Brino, M. (2016). Parametric, Asymmetric and Stochastic-Based 3D CAD Model of Tonda Gentile Trilobata Hazelnut Variety. *Biosystems Engineering*, 144:72–84.
- Torppa, J., Valkonen, J. P. T., and Muinonen, K. (2006). Three-Dimensional Stochastic Shape Modelling for Potato Tubers. *Potato Research*, 49(2):109–118.
- University of Southern California (2017). LONI: Laboratory of Neuro Imaging.
- Unur, E., Ulger, H., and Ekinçi, N. (2002). Morphometrical and morphological variations of middle ear ossicles in the newborn. *Erciyes Tıp Dergisi (Erciyes Medical Journal)*, 24(2):57–63.
- Valdés-Hernández, P. A., von Ellenrieder, N., Ojeda-Gonzalez, A., Kochen, S., Alemán-Gómez, Y., Muravchik, C., and Valdés-Sosa, P. A. (2009). Approximate average head models for EEG source imaging. *Journal of Neuroscience Methods*, 185(1):125–132.
- Valette, S., Chassery, J. M., and Prost, R. (2008). Generic remeshing of 3D triangular meshes with metric-dependent discrete voronoi diagrams. *IEEE Transactions on Visualization and Computer Graphics*, 14(2):369–381.
- Van Dael, M., **Danckaers**, F., De Schryver, T., Huysmans, T., Verboven, P., Van Hoorebeke, L., Sijbers, J., and Nicolai, B. (2016). Combining 3D Vision and X-ray Radiography for Internal Quality Inspection of Foods. In *30th Targeted Technologies for Sustainable Food Systems (EFFoST) International Conference*, Austrian Economic Chamber, Vienna, Austria.
- Van der Jeught, S., Dirckx, J. J. J., Aerts, J. R. M., Bradu, A., Podoleanu, A. G., and Buytaert, J. A. N. (2013). Full-Field Thickness Distribution of Human Tympanic Membrane Obtained with Optical Coherence Tomography. *Journal of the Association for Research in Otolaryngology*, 14(4):483–494.
- Van der Jeught, S., Soons, J. A. M., and Dirckx, J. J. J. (2015). Real-time microscopic phase-shifting profilometry. *Applied optics*, 54(15):4953–9.
- Van Der Meulen, P. and Seidl, A. (2007). RAMSIS - The Leading Cad Tool for Ergonomic Analysis of Vehicles. *Lncs*, 4561:1008–1017.
- Van Dijck, C., Wirix-Speetjens, R., Huysmans, T., **Danckaers**, F., Sijbers, J., and Vander Sloten, J. (2014). Influence of Correspondence Method on Statistical Model Based Shape Prediction. In *Symposium on Statistical Shape Models & Applications*, page 2014.

-
- Van Houtte, J., Stanković, K., Booth, B. G., **Danckaers**, F., Bertrand, V., Verstreken, F., Sijbers, J., and Huysmans, T. (2019). An Articulating Statistical Shape Model of the Human Hand. In *Advances in Human Factors in Simulation and Modeling*, pages 433–445. Springer, Cham.
- Verboven, P., Flick, D., Nicolai, B. M., and Alvarez, G. (2006). Modelling transport phenomena in refrigerated food bulks, packages and stacks: basics and advances. *International Journal of Refrigeration*, 29(6):985–997.
- Verwulgen, S., Lacko, D., De Bruyne, G., **Danckaers**, F., Christis, N., Sijbers, J., and Huysmans, T. (2014). Anthropometrics 2.0: Enrichment of classical anthropometry through multidisciplinary collaboration. In *Proceedings of the 16th International Conference on Engineering and Product Design Education: Design Education and Human Technology Relations, EPDE 2014*.
- Vitronic (1995). Inhalte Lightbox - VITRONIC - the machine vision people.
- Wang, L. and He, X. (2013). Model reconstruction of human buttocks and the shape clustering. In *Lecture Notes in Computer Science (including subseries Lecture Notes in Artificial Intelligence and Lecture Notes in Bioinformatics)*, volume 8026 LNCS, pages 245–251. Springer, Berlin, Heidelberg.
- Wang, Y., Chua, C. S., and Ho, Y. K. (2002). Facial feature detection and face recognition from 2D and 3D images. *Pattern Recognition Letters*, 23(10):1191–1202.
- Weistenhöfer, C. and Hudde, H. (1999). Determination of the shape and inertia properties of the human auditory ossicles. *Audiology and Neuro-Otology*, 4(3-4):192–196.
- Wendell Todd, N. and Creighton, F. X. (2013). Malleus and incus: Correlates of size. *Annals of Otology, Rhinology and Laryngology*, 122(1):60–65.
- Wold, H. (1973). Nonlinear Iterative Partial Least Squares (NIPALS) Modelling: Some Current Developments. In *Multivariate Analysis-III*, pages 383–407. Elsevier.
- Woods, C., Fernee, C., Browne, M., Zakrzewski, S., and Dickinson, A. (2017). The potential of statistical shape modelling for geometric morphometric analysis of human teeth in archaeological research. *PLoS ONE*, 12(12):e0186754.
- Wuhrer, S. and Shu, C. (2013). Estimating 3D human shapes from measurements. *Machine Vision and Applications*, 24(6):1133–1147.
- Wuhrer, S., Shu, C., and Xi, P. (2012). Posture-invariant statistical shape analysis using Laplace operator. *Computers and Graphics (Pergamon)*, 36(5):410–416.
- Xi, P. and Shu, C. (2009). Consistent parameterization and statistical analysis of human head scans. *Visual Computer*, 25(9):863–871.
- Zadavec, P., Veberic, R., Stampar, F., Eler, K., and Schmitzer, V. (2013). Fruit size prediction of four apple cultivars: Accuracy and timing. *Scientia Horticulturae*, 160:177–181.
- Zhang, L., Makwana, R., and Sharma, S. (2013). Brain response to primary blast wave using validated finite element models of human head and advanced combat helmet. *Frontiers in Neurology*, 4 AUG(August):1–12.

Bibliography

Zheng, G., Gollmer, S., Schumann, S., Dong, X., Feilkas, T., and González Ballester, M. A. (2009). A 2D/3D correspondence building method for reconstruction of a patient-specific 3D bone surface model using point distribution models and calibrated X-ray images. *Medical Image Analysis*, 13(6):883–899.

Developed Software



During this research, following software has been developed:

- A command line tool for obtaining correspondence between two surfaces, using elastic surface registration. As input, a source and target surface are given. The output is the deformed source surface, that resembles the shape of the target surface.
- A GUI to simulate a body shape from measurements. The user can fill in some measurements, such as gender, stature, weight,... and the program simulates the most plausible body shape based on those measurements.
- A tool to generate a skeleton relative to the body shape. This tool is also incorporated in the GUI to generate a body shape from measurements.
- A program to predict a body shape in another pose from a 3D scan in a basic pose when two shape models are available, both from the basic pose as in the other pose.
- Multiple analysis (ANOVA, 2-way MANOVA, t-test) of variance algorithms are implemented to calculate the difference in shape between groups of subjects.
- K-means clustering to group shapes. This algorithm is useful for generating a new sizing system based on the shapes that occur in the population.
- A tool to automatically segment 2D scans (e.g. CT or MRI scans) and stack those scans to generate a 3D surface.

Curriculum Vitae

Femke Danckaers was born in Brasschaat, Belgium on July 30, 1990. She attended high school at the Royal Atheneum Brasschaat. Femke graduated as a Master of Science in applied engineering: Electronics-ICT in June 2013 (cum laude). In her final year, she worked in a multidisciplinary team on a project called "Anthropometrics 2.0", for which she received the "Belgian Industrial Research & Development (BiR&D) Interdisciplinary Master of Science Thesis Programme 2012"-award. In August 2013, she started her PhD at the Vision Lab in the field of statistical shape modeling, where her research was funded by an IWT scholarship. Her work focusing on 3D surface registration, statistical shape modeling, and related applications has lead to this manuscript.

Publications

Journal articles

- **Danckaers**, F., Huysmans, T., Hallemans, A., De Bruyne, G., Truijen, S., and Sijbers, J. (2018b). Posture normalization of 3D body scans. *Ergonomics*
- Keustermans, W., Huysmans, T., **Danckaers**, F., Zarowski, A., Schmelzer, B., Sijbers, J., and Dirckx, J. (2018). High quality statistical shape modelling of the human nasal cavity and applications. *Royal Society Open Science*
- **Danckaers**, F., Huysmans, T., Van Dael, M., Verboven, P., Nicolai, B., and Sijbers, J. (2017). Building 3D Statistical Shape Models of Horticultural Products. *Food and Bioprocess Technology*, 10(11):2100–2112
- Crum, W. R., **Danckaers**, F., Huysmans, T., Cotel, M. C., Natesan, S., Modo, M. M., Sijbers, J., Williams, S. C., Kapur, S., and Vernon, A. C. (2016). Chronic exposure to haloperidol and olanzapine leads to common and divergent shape changes in the rat hippocampus in the absence of grey-matter volume loss. *Psychological Medicine*, 46(15):3081–3093
- Soons, J. A., **Danckaers**, F., Keustermans, W., Huysmans, T., Sijbers, J., Casselman, J. W., and Dirckx, J. J. (2016). 3D morphometric analysis of the human incudomalleal complex using clinical cone-beam CT. *Hearing Research*, 340:79–88

Conference proceedings

- **Danckaers**, F., Scataglini, S., Haelterman, R., Van Tiggelen, D., Huysmans, T., and Sijbers, J. (2019). Automatic generation of statistical shape models in motion. In *Advances in Human Factors in Simulation and Modeling*, pages 170–178. Springer, Cham
- Van Houtte, J., Stanković, K., Booth, B. G., **Danckaers**, F., Bertrand, V., Verstreken, F., Sijbers, J., and Huysmans, T. (2019). An Articulating Statistical Shape Model of the Human Hand. In *Advances in Human Factors in Simulation and Modeling*, pages 433–445. Springer, Cham
- Huysmans, T., **Danckaers**, F., Vleugels, J., Lacko, D., De Bruyne, G., Verwulgen, S., and Sijbers, J. (2019). Multi-patch B-spline statistical shape models for CAD-compatible digital human modeling. In *Advances in Human Factors in Simulation and Modeling*, pages 179–189. Springer, Cham

- **Danckaers**, F., Lacko, D., Verwulgen, S., De Bruyne, G., Huysmans, T., and Sijbers, J. (2018c). A Combined Statistical Shape Model of the Scalp and Skull of the Human Head. In *Advances in Intelligent Systems and Computing*, volume 591, pages 538–548. Springer, Cham
- **Danckaers**, F., Huysmans, T., Halleman, A., De Bruyne, G., Truijten, S., and Sijbers, J. (2018a). Full Body Statistical Shape Modeling with Posture Normalization. In *Advances in Intelligent Systems and Computing*, volume 591, pages 437–448. Springer, Cham
- **Danckaers**, F., Huysmans, T., Van Dael, M., Verboven, P., Nicolai, B., and Sijbers, J. (2016b). Building Statistical Shape Models of Vegetables and Fruit. In *National Symposium for Applied Biological Sciences (NSABS)*
- **Danckaers**, F., Huysmans, T., Rogge, S., Van Dael, M., Verboven, P., Nicolai, B., and Sijbers, J. (2016a). Building a Statistical Shape Model of the Interior and Exterior of the Bell Pepper. In *30th Targeted Technologies for Sustainable Food Systems (EFFoST) International Conference*, volume 28-30 Nove, Vienna, Austria
- Van Dael, M., **Danckaers**, F., De Schryver, T., Huysmans, T., Verboven, P., Van Hoorebeke, L., Sijbers, J., and Nicolai, B. (2016). Combining 3D Vision and X-ray Radiography for Internal Quality Inspection of Foods. In *30th Targeted Technologies for Sustainable Food Systems (EFFoST) International Conference*, Austrian Economic Chamber, Vienna, Austria
- Stanković, K., **Danckaers**, F., Booth, B. G., Burg, F., Duerinck, S., Sijbers, J., and Huysmans, T. (2016). Foot Abnormality Mapping using Statistical Shape Modelling. In *Proceedings of the 7th International Conference on 3D Body Scanning Technologies, Lugano, Switzerland, 30 Nov.-1 Dec. 2016*, pages 70–79, Ascona, Switzerland
- **Danckaers**, F., Huysmans, T., Van Dael, M., Verboven, P., Nicolai, B., and Sijbers, J. (2015b). Building a Statistical Shape Model of the Apple from Corresponded Surfaces. *Chemical Engineering Transactions*, 44:49–54
- **Danckaers**, F., Huysmans, T., Lacko, D., and Sijbers, J. (2015a). Evaluation of 3D Body Shape Predictions Based on Features. In *Proceedings of the 6th International Conference on 3D Body Scanning Technologies, Lugano, Switzerland, 27-28 October 2015*, pages 258–265, Ascona, Switzerland
- Soons, J., **Danckaers**, F., Huysmans, T., Sijbers, J., Casselamn, J. W., and Dirckx, J. J. J. (2015). Statistical Shape Modeling of the Incudomalleolar Complex using Micro-CT and Clinical Cone-beam CT. In *MEMRO: 7th International Symposium on Middle Ear Mechanics in Research and Otology*, Aalborg, Denmark
- **Danckaers**, F., Huysmans, T., Lacko, D., Ledda, A., Verwulgent, S., Van Dongen, S., and Sijbers, J. (2014). Correspondence preserving elastic surface registration with shape model prior. In *Proceedings - International Conference on Pattern Recognition*, pages 2143–2148, Stockholm, Sweden. IEEE

-
- Van Dijck, C., Wirix-Speetjens, R., Huysmans, T., **Danckaers**, F., Sijbers, J., and Vander Sloten, J. (2014). Influence of Correspondence Method on Statistical Model Based Shape Prediction. In *Symposium on Statistical Shape Models & Applications*, page 2014
 - Verwulgen, S., Lacko, D., De Bruyne, G., **Danckaers**, F., Christis, N., Sijbers, J., and Huysmans, T. (2014). Anthropometrics 2.0: Enrichment of classical anthropometry through multidisciplinary collaboration. In *Proceedings of the 16th International Conference on Engineering and Product Design Education: Design Education and Human Technology Relations, EPDE 2014*

